INFORMATION TO USERS

University of Alberta

Characteristics of the Vortex Structure in the Outlet of a

Stairmand Cyclone: Regular Frequencies and Reverse Flow

by

Mei Chen ©

A thesis submitted to the Faculty of Graduate Studies and Research in partial fulfillment

of the requirements for the degree of Master of Science in Chemical Engineering

Department of Chemical and Materials Engineering

Edmonton, Alberta

Fall 1999

Canada

University of Alberta

Library Release Form

Name of Author: Mei Chen

Title of Thesis: Characteristics of the Vortex Structure in the Outlet of a
Stairmand Cyclone: Regular Frequencies and Reverse Flow

Degree: Master of Science

Year this degree granted: 1999

Permission is hereby granted to the University of Alberta Library to
reproduce single copies of this thesis and to lend or sell such copies for private, scholarly
or scientific research purposes only.

The author reserves all other publication and other rights in association with the
copyright in the thesis, and except as herein before provided, neither the thesis nor any
substantial portion thereof may be printed or otherwise reproduced in any material form
whatever without the author's prior written permission.
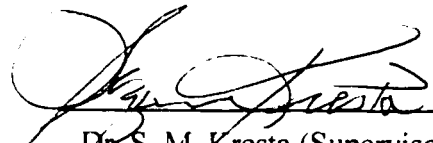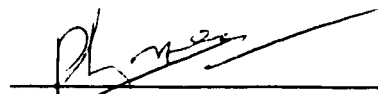
Mei Chen
Apt. 521
609 Devenport Rd.
Waterloo, Ontario
Canada
N2L 6H9

Date: *Aug. 13, 1999*
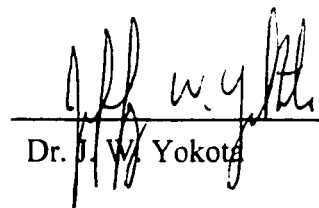
University of Alberta
Faculty of Graduate Studies and Research

The undersigned certify that they read and recommend to the Faculty of Graduate Studies and Research, an thesis entitled **Characteristics of the vortex structure in the outlet of a Stairmand cyclone: regular frequencies and reverse flow** submitted by Mei Chen in partial fulfillment of the requirements for the degree of Master of Science in Chemical Engineering.

Dr. S. M. Kresta (Supervisor)

Dr. P. A. J. Mees (Supervisor)

Dr. K. Nandakumar

Dr. J. W. Yokota

Date: Aug, 9, 1999

To my diligent and sacrificial parents

To whom I owe all that I am

.

Abstract

In this project, a combination of experiments and simulations is used to investigate the penetration of the processing vortex core into the cyclone, the extent of the reverse flow, and the impact of the geometry on the flow field.

Periodic motions were detected in the gas outlet tube or just outside of the gas outlet tube with the three gas outlet tube diameters tested. The observed oscillations are caused by a coherent structure. These oscillations grow less vigorous down the gas outlet tube and eventually die out. Time averaged axial velocity profiles at different elevations indicate that the back flow region shrinks down the gas outlet tube.

Numerical simulation (3D) was also conducted. With the Reynolds Stress Model (RSM) to account for the non-isotropic effect of turbulence in the highly swirling flow, the CFD simulation prove to be effective in capturing the essential features of the flow in cyclone.

Acknowledgments

Table of Contents

List of Tables

.

List of Figures

Nomenclature

A	inlet width	m
A_{in}	inlet area	m^2
B	inlet hight	m
D_{barrel}	barrel diameter	m
D_{outlet}	gas outlet tube diameter	m
d_p	critical size particle diameter	μm
E_l	one dimensional power spectrum	m^2/s
F	oscillation frequency	1/s
F_c	centrifugal force	N
f_D	Doppler frequency	MHz
F_d	drag force	N
G_θ	axial flux of swirl momentum	
G_z	axial flux of axial momentum	$kg\ m^2/s^2$
$H(f)$	continuous fourier transform	m/s
$h(t)$	continuous time series of data	m/s
H^*	complex conjugate	m/s
H_k	discrete fourier transform	m/s
h_k	discrete time series data	m/s
h_{top}	height with respect to the top of cyclone	m
K_{fi}	friction loss coefficient at the inlet	
K_{fo}	friction loss coefficient in the outlet tube	
M	axial momentum	kg m/s
$f_{Nyquist}$	Nyquist frequency	1/s
P	pressure	pa
Q	volumetric flow rate	m^3/s

R	radial position	m
Re	Reynolds number	-
R_E	autocorrelation coefficient function	-
S_t	the Strouhal number	-
S_w	the Swirl number	-
t	time lag	s
U	axial velocity	m/s
W	tangential velocity	m/s
u_f	fluctuating velocity	m/s
u_p	fluctuating velocity contributed by periodic motion	m/s
u_{tur}	turbulence fluctuating velocity	m/s
V	radial velocity	m/s
W	tangential velocity	m/s
Z	axial direction	m

Greek

τ	time	s
θ	beam intersection angle	rad
μ	viscosity of gas	kg/m s
ω	angular velocity	rad/s
λ_0	wavelength of light	m
δ_f	fringe spacing	μm
ω_r	vorticity at r direction	1/s

Chapter 1: Introduction

1.1 The function of a cyclone

Gas cyclone separators are widely used to collect particles from industrial gas streams. The duty of a cyclone is to take in a supply of contaminated gas and separate it into its components of dust and clean gas as perfectly as possible with the least consumption of pressure head. Cyclones have no moving parts, relying on centrifugal forces due to fluid flow to separate the particles from the gas. A cyclone can operate at high superficial velocities and at a high dust load. The performance of a cyclone can be quantified by the collection efficiency, which is defined as the fraction of any given size particles that is separated by the cyclone. Efficiency is a function of particle size. It is low for smaller particles and high for large ones. This project investigated several issues that might affect the collection efficiency. The results can provide useful information for improved cyclone design.

1.2 Geometric variables of a cyclone

Most cyclones are of the cone-cylinder type. All cyclones have a gas inlet, gas outlet or vortex finder, and dust discharge. Various arrangements of these three elements leading to different cyclone configurations are possible. The usual arrangement has a tangential inlet with two axial outlets for clean gas and collected dust and is called a reverse-flow cyclone, as shown in Figure 1.1. The dimensions of a reverse-flow cyclone, as shown in Figure 1.2, are often expressed as their ratio to cyclone barrel diameter. Each set of dimensionless ratios constitutes a cyclone "design".

1.3 General flow pattern in a cyclone

Although the geometry of the cyclone is simple, the pattern of the gas flow is extremely complex. There are three main flow patterns that prevail in all cyclones. These are:

- Descending spiral flow - This pattern carries the separated dust down the walls of the cyclone.

- Ascending spiral flow - This rotates in the same direction as the descending spiral, but the cleaned gas is carried from the dust discharge to the gas outlet.

- Radially inward flow - This feeds the gas from the descending to the ascending spiral.

Cyclone performance is evaluated in terms of pressure drop and collection efficiency. To assess factors that contribute to performance, the tangential, radial, and axial velocity components of the velocity field must be understood. The axial velocity is directed upwards in the core and downwards along the wall. The absolute value of the radial velocity is at least one order of magnitude lower than the axial velocity components. Its magnitude is probably as large as the fluctuation of the tangential and axial velocity components. The tangential velocity can be described as a Rankine vortex. i.e. a combination of a free vortex and a forced vortex. The tangential velocity increases with the radius and reaches a maximum at about 60~70% of the diameter then decreases towards the wall.

1.4 The mechanism of particle separation

Separation of particles in the cyclone occurs due to the centrifugal force caused by the spinning gas stream. For a particle rotating with the same speed as the tangential gas velocity w at radial position r. the centrifugal force is:

$$F_c = ma = \frac{1}{6}\pi d_p{}^3 \rho_p \cdot \frac{w^2}{r} = \frac{\pi \rho_p d_p{}^3 w^2}{6r} \qquad (1.1)$$

Opposing the outward particle motion resulting from the centrifugal force is an inward drag force:

$$F_d = 3\pi\mu \, d_p(v - V) \qquad (1.2)$$

2

v is the outward radial velocity of the particle while V is the gas radial velocity directed toward the cyclone axis. Equation (1.2) is Stoke's law, although this may be a poor assumption for large particles with high radial velocity since Stoke's law is only applicable at very low Reynolds number.

By balancing the centrifugal force and the drag force, the critical particle size can be determined. The equilibrium of the centrifugal and drag forces can be used to determine the separation efficiency, the pressure loss and operation parameters. This is the traditional approach to cyclone design (Cheremisinoff & Gupta 1983). All particles with a diameter larger than the critical particle size are transported outward and separated. All particles with a diameter smaller than the critical particle size will be carried out through the outlet pipe with the fluid. This is only true theoretically. The actual separation efficiency curve is 'S' shaped as shown on Figure 1.3 and depends essentially on the geometric dimensions and operating conditions of the cyclone.

1.5 Previous investigations

1.5.1 Experimental work

During the last half century, many researchers have investigated the gas flow field in a cyclone with adjustable inlet, outlet, length and flow rate through different approaches. A large amount of experimental data has been acquired on cyclone performance (Ter linden, 1949: Stairmand 1951, Linoya 1953) which forms the basis of semi-empirical correlations on which current design practice is almost entirely based, and most studies focused on the improvement of collection efficiency (Kessler & Leith 1991, Hoffman *et al.* 1996, Kim & Lee 1997, Ogawa 1997). Previous work has constructed a picture of the basic flow pattern in a cyclone, but there are still several issues which are unclear. This research will focus on two of them: back flow and oscillations.

1.5.1.1 Back flow in the center of the core

Most researchers (ter Linden 1949, Baluev & Troyankin 1969, Abrahamson *et al.* 1978, Hargreaves & Silvester 1990, Hsieh & Rajamani 1991) agree that, as the air flow enters the cyclone tangentially, it moves towards the wall, forming an outer downward vortex

3

flow due to the strong action of the centrifugal force. After the flow reaches the bottom, it turns around and forms an upward vortex flow, as shown in Figure 1. Some researchers (Boysan *et al.* 1983, Zhou & Soo 1990) reported that in the case of a strong swirl the axial velocity could also be downward in the center of the core. This phenomenon is called back flow or reverse flow. Reydon & Gauvin (1981) reported that with a smaller diameter outlet, the possibility of having reverse axial flow decreases.

Back flow has long been detected in swirling flows. A swirling flow is defined as one undergoing simultaneous axial and vortex motions, such as the motions in combustion chambers or cyclone separators.

Harvey (1962) was the pioneer who detected back flow in swirling flows. He carried out an experiment in which a cylindrical vortex formed in a long tube. By varying the amount of swirl that was imparted to the fluid before it entered the tube, it was found that the rotating flow could exhibit axial velocity reversal. Chanaud (1965) observed reverse flow in a vortex whistle (two concentric cylinders) when the Reynolds number exceeded 300. The reverse flow was centered on the tube axis and was more elongated than what was observed by Harvey (1962). Cassidy & Falvey (1970) studied the rotating flow through a straight tube. As the angular momentum flux was increased, a flow reversal was observed to occur in the jet downstream from the tube exit. Further increase in the angular momentum flux forced the reversed-flow beginning upstream just into the tube as observed by Harvey (1962), and this can produce a precessing helical vortex throughout the tube.

Syred & Beer (1974) conducted research in combustion in swirling flow and concluded that the reverse flow zones are dependent on the mixture ratio and on the mode of fuel entry, but made no attempt to show how the reverse flow zone can be affected by the geometry of the combustion chamber.

Vu & Gouldin (1982) have proposed the mechanism for adverse pressure gradient in two confined coaxial swirling jets. The radial momentum equation can be integrated to obtain:

4

$$\frac{\partial \overline{P}}{\partial r_{r=0}} = \frac{\partial \overline{P}}{\partial r_{r=R}} + \frac{\partial}{\partial r} \int_0^R \frac{\rho \overline{V}^2}{r} dr \qquad (1.3)$$

where turbulence and viscous stresses are neglected, the overbar denotes mean quantities, and R is the section radius. For flow reversal, the last term of the above equation must be sufficiently positive to overcome the negative $\partial \overline{P} / \partial r$ contribution at the wall and the dynamic head of the axial flow.

In a review on combustion in swirling flows, Gupta *et al.* (1984) have cited evidence to show that the flow downstream exhibits a large temporal instability which they have called a precessing vortex core (PVC). They suggested that, for high Reynolds number flow, the precessing vortex core is important to the mechanism for flow reversal. Gouldin *et al.* (1985) argued that this mechanism is only applicable in flows with large amplitude oscillation. They proposed a new mechanism by applying Bernoulli's equation in a sudden expansion combustor and a burner. So far, there is not a satisfactory solution to the mechanism of reverse flow in swirling flow.

1.5.1.2 Flow oscillation in cyclone

Flow oscillations in cyclones have seldom been investigated. They are not well documented in the literature and are often referred to as a kind of fluid dynamic instability. The instability has long been detected in swirling flows. The behavior of highly swirling flow is complicated by several different instabilities and changes in flow pattern with variation in Reynolds and swirl number, and the instability occurrence is called vortex breakdown which is characterized by flow reversal (Syred & Beer 1974).

Squire (1960) studied this occurrence analytically and deduced that breakdown would occur when the local swirl angle ($\tan^{-1} = w / u$) exceeds $52.5\,^0$. In the swirl ratio u and w are the local axial and tangential velocity components. Harvey (1962) obtained experimental results agreeing with Squire's analysis.

The instability in the swirling flow can ultimately develop into regular oscillations. Theory and experiment associated with this phenomenon led to two somewhat different

explanations (Chanaud 1965). The first is that oscillation is due to the amplification of small disturbances and the second is that it is an abrupt change between two basic types of rotating flows. Hall (1966) discussed the possible types of change in the concentrated vortex core structure that includes the instability, and analyzed different stability criteria. One of the theories is the stability criterion of Rayleigh applied to spiraling flows. It showed that any inviscid flow in which the circulation decreases with increasing distance from the axis is unstable. Based on this, if a flow is in a state approaching a rigid rotation then it will be highly stable. In a cyclone. the circulation is $2\pi rw$, where w is the swirl velocity. w can be expressed as:

$$w = cr \qquad \text{for forced vortex(solid body rotation)}$$

$$w = c' / r \qquad \text{for free vortex}$$

by substituting the above two expressions into $2\pi rw$. the circulation for forced vortex and free vortex will be $2\pi cr^2$ and $2\pi c'$. leading to the increasing or constant circulation with increasing radius which satisfied stability based on Rayleigh's criteria. According to this. the oscillations in the cyclone should be stable.

Cassidy & Falvey (1970) investigated the flow in a plexiglass tubes. They observed that a helical vortex was generated if the angular momentum flux was sufficiently large relative to the flux of linear momentum. The study described the occurrence. frequency and peak to peak amplitude of the wall pressure generated by the vortex. The frequency and amplitude are independent of viscous effects for high Reynolds numbers.

Faler & Leibovich (1978) used a laser-Doppler anemometer to provide a detailed velocity map of the interior and flow upstream of a bubble form of vortex breakdown in a laminar water flow. They detected well-defined energetic low frequency oscillations in the interior of the bubble and in the near wake. Garg & Leibovich (1979) have investigated the spectral characteristics of vortex breakdown flowfields in a tube with a small divergence angle. They used an inviscid linear stability analysis for parallel flows developed by Lessen et al. (1974) and showed that these oscillations are associated with the normal mode of non-axisymmetric instabilities in the flow. They are unable to

determine whether the nonaxisymmetric instabilities in some way promote breakdown. In an isothermal dump configuration, Janjua & Mclaughlin (1986) observed oscillations with only a limited number of experiments and did not show how these oscillations changed in the streamwise direction. However, they showed that the Strouhal number, based on the inlet tube diameter and the maximum inlet velocity, was independent of the Reynolds number. Their phase measurements indicated that the origin of the oscillations was non-axisymmetric disturbances. Vu & Gouldin (1982) conducted research in isothermal confined coaxial swirling flows with Reynolds comparable to those by Garg & Leibovich (1979). They observed frequencies over an order of magnitude higher than those of Garg & Leibovich (1979). Unfortunately, they did not give any details and did not offer any explanations for their results.

Leibovich (1983) argued against Syred & Beer (1974)'s findings that the axial flow reversals could be created in swirling flows without any sign of hydrodynamic instability to infinitesimal disturbances. A breakdown event causes significant modifications of the vortex structure. However, experiments at high Reynolds numbers reveal that the flow downstream of it is always more unstable than that upstream. Breakdown acts as a switch that marks the onset of transition to a turbulent flow downstream if the flow upstream is laminar, or transition to a flow with a higher level of turbulent fluctuations downstream if the vortex upstream of breakdown is already turbulent.

Gupta et al.(1984) demonstrated by flow visualization that vortex core precession occurs in especially long cyclone dust separators with $L/D > 4$. With short cyclone chambers $(L/D << 1)$ at high degree of swirl, the very strong radial inflows in the wall boundary layers can affect the precessing vortex core. In such a device $(L/D = 0.1)$ up to two concentric bands of PVCs may occur around the varying areas of recirculation. In the exit, four distinct PVCs were found, while in the outer part of the chamber at the boundary of the outer reverse flow zone, a secondary ring containing many PVCs occurs.

Kumar & Conover (1993) observed a helical flow pattern that surrounded a secondary flow by using reflective particles in a cylinder. They observed that the center of the vortex appears in the first quadrant at the inlet and meanders around anticlockwise as it

traverses the length of the cylinder. The vortex center in the cross sections is observed to be stable but not steady. This center would frequently move from its average location. Bernard (1992) observed oscillations in his flow visualization in a cyclone and concluded that not only the turbulence of the flow pattern but also the construction of the cyclone and the way the flow is introduced into the cyclone might cause the instability.

Experiments by Yazdabadi *et al.* (1994) show that as the Reynolds number is increased, a large three dimensional time dependent instability develops just outside the vortex finder of the cyclone, and the flow field in that region oscillates with a regular frequency and amplitude. For it to be a stable oscillation, there must be a feedback mechanism, and it has been suggested that this is provided by the reverse flow zone in the vortex finder. The oscillation is greatly affected by the swirl number defined as the ratio of the axial flux of swirl momentum to the axial flux of axial momentum.

1.5.2 Numerical work

Early in the nineteen seventies, Kopecky & Torrance (1973) and Grabowski & Berger (1976) carried out numerical computations of steady, laminar, axisymmetric Navier-Stokes equations in attempts to simulate the back flow. The results obtained by them differ from experiments in the following ways:

a): The numerical solutions do not reveal the two-celled structure in the interior of the recirculation zone revealed by the time-averaged streamlines constructed from the experimental data of Faler (1976).

b): Back flow has never been seen at low Reynolds numbers such as those used in the computations.

In the last 15 years, a theoretical approach based on the calculation of the actual flow field from the Navier-Stokes equations has become more popular thanks to the development of faster computers with more memory. After the gas flow field is calculated, the motion of single particles introduced into the flow can be tracked. By calculating particle paths for different size particles, a separation efficiency curve can be

determined. Such an approach is valid for dilute slurries only, since only in this kind of flow particle-particle interactions can be neglected. The fluid motion is not affected by the contributing source terms in the Navier-Stokes equations due to particle-fluid interaction, but the influence from the surrounding gas on the particle is retained. (Frank *et al.* 1998)

For the turbulent flow field in a cyclone, the key to a successful computation lies in the accurate description of turbulent behavior of the flow. According to Hanjalic (1994), three types of turbulence models could be identified as fast engineering methods (despite the need to solve partial differential equations)

❏ two-equation eddy-viscosity models ($k-\varepsilon$)

❏ the differential Reynolds stress equation model (RSM) (differential second-moment closure); and

❏ intermediate (truncated) and hybrid models that hierarchically fall in between these two and take some advantages from each of them (ASM)

The $k-\varepsilon$ model in its rudimentary form has a major advantage in its simplicity and practical usability. Zhou & Soo (1990) assume non-theta gradients and applied the $k-\varepsilon$ turbulence model to solve the tangential and axial velocity in a cyclone. In the near-axis region, the numerical predictions give much higher values than those obtained from measurements. The discrepancy is a result of the defect of the $k-\varepsilon$ model, which cannot account for the non-isotropic turbulence structure due to the different magnitudes of velocity components and hence gives high values of the turbulent viscosity, leading to a high axial velocity near the axis.

Many researchers made modifications to the $k-\varepsilon$ model, Yap's (1987) proposal stands out as one interesting theory because he thinks the $k-\varepsilon$ produces near-wall length scales that are too large; he therefore added a source term in the ε equation. Minier *et al.*(1991) consider Yap's (1987) model as an attractive and inexpensive alternative to the complete RSM model if $k-\varepsilon$ shortcomings are to be overcome.

The Reynolds-stress model (RSM) is regarded as the natural and most logical level of modeling within the framework of the Reynolds averaging approach. Since it provides the extra turbulent momentum fluxes from the solution of full transport equations, it requires a length-scale-supplying equation. Although the Reynolds stress model performs much better than the k-ε model in swirling flow because it accounts automatically for the effects of stress anisotroy, it has the disadvantage of being computationally expensive. An intermediate solution might be to use the algebraic stress model (ASM) which transforms the differential equations into algebraic ones and leads to direct expressions for the Reynolds stress components. The development of the ASM raised two coefficients, incorporating a total of nine new parameters. Boysan et al. (1982) developed this model and found better than expected agreement with certain regimes of swirling flow. Hoffman et al. (1996) predicted back flow using a 2-dimensional ASM model. The length of the vortex finder has a very important effect on the appearance of back flow. However, some authors argue that the algebraic stress model should not be used for axisymmetric swirling flow. Fu et al. (1986) emphasized that despite the significant time savings, the ASM scheme ought not to be used where stress-transport processes give rise to significant terms in the overall Reynolds stress.

So far, the differential Reynolds stress model (RSM) is the most promising turbulence model for describing the swirling cyclone flow. Boysan (1984) predicted reverse flow in the cyclone using RSM. Mees'(1997) 3D simulations using CFX software (from AEA technology) with the RSM model also show oscillations in the body of the cyclone. Researchers are still not sure about the proper boundary conditions at the two cyclone outlets because of insufficient experimental data. Usually, fully developed flow boundary conditions are imposed at the exits.

1.6 Approach used in this work

The objective of this work is to investigate the existence of the three dimensional time dependent instability in the body of the cyclone, and examine back flow in the cyclone under the influence of various gas outlet geometries. Experiments were conducted in a glass cyclone using Laser Doppler anemometry. The flow was modeled using second

order Reynolds stress closure. The results will give information valuable for the designer about the effects of oscillation and back flow on the separation efficiency.

Laser Doppler anemometry (LDA) was used to measure the axial and tangential components in or just outside the gas outlet to provide boundary conditions for the simulations. Some measurements have also been carried out in the barrel and cone of the cyclone.

Frequency analysis was used to analyze the low frequency instability of the coherent structure. The LDA time series were analyzed using the autocorrelation function and spectral analyses. Since traditional FFT analysis cannot be employed for the unevenly spaced data collected by our instrument, a slotting technique was applied.

Finally, 3D transient CFD simulations were carried out to validate the model with the ultimate aim of predicting flow in other geometries. The Reynolds stress model of turbulence was used. The effects of inlet velocity and boundary conditions were examined.
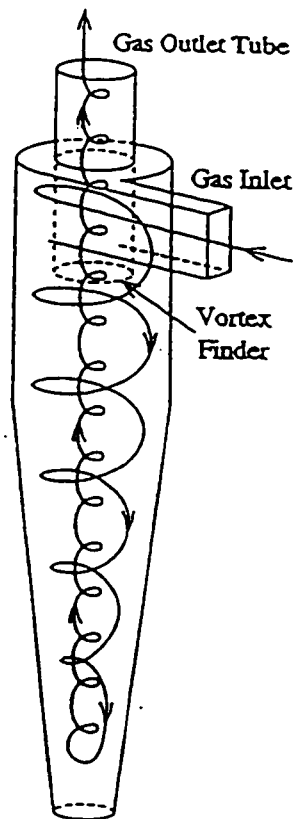
Figure 1.1 Cyclone geometry and general flow pattern
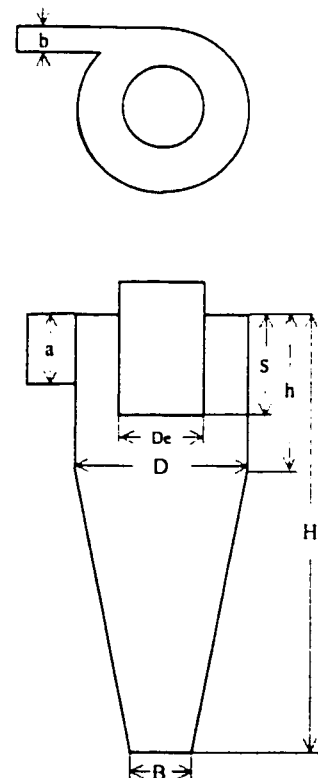
Figure 1.2 Cross-sectional dimensions of a reverse flow cyclone
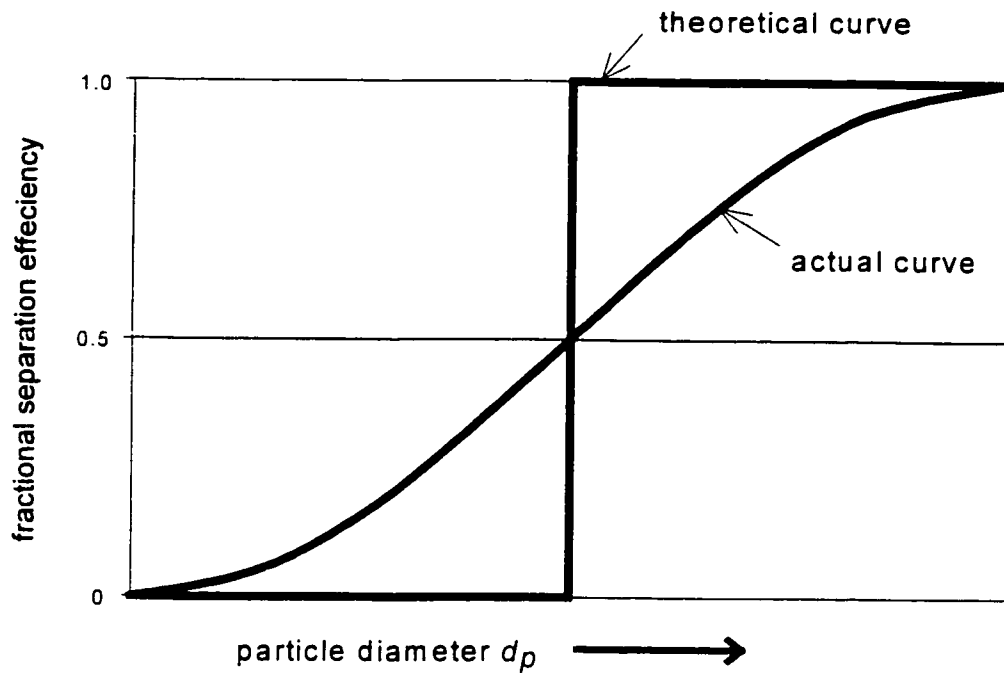
Figure 1.3 Fractional separation efficiency

References

Abrahamson, J., C.G. Martin, & K.K. Wang. 1978. *The physical mechanisms of dust collection in a cyclone*. Trans. I. Chem. E., **56**, 168-177.

Baluev, E.D., & Yu.V.Troyankin, 1969. *The Aerodynamics Resistance and Efficiency of a Cyclone Chamber*. Teploenergetika, **16**, 6-29

Bernard, J.G. 1992. *Experimental Investigation and Numerical Modeling of Cyclones for Application at High Temperatures*, Doctoral Thesis, Technische Univ. Delft

Boysan, F., B.C.R. Ewan, J. Swithenbank, & W.H. Ayers, 1983. *Experimental and theoretical studies of cyclone separator aerodynamics*. I.Chem. E. Symp. Ser., **69**, 305-319.

Boysan, F., 1984, *Mathematical modeling of cyclone separation*, Proceedings of 9th lecture series on two-phase flow, Trondheim, Norway.

Chanaud, Robert C., 1965, *Observations of oscillatory motion in certain swirling flows*. J. Fluid Mech. **21**, 111-127

Cheremisinoff, N.P., & R. Gupta, 1983. *Handbook of Fluids in Motion*. 847-860

Cassidy, John J., & Henry T. Falvey, 1970, *Observations of unsteady flow arising after vortex breakdown*. J.Fluid Mech, **41**, 727-736

Faler, J.H., & S. Leibovich, 1978, *An experimental of vortex breakdown flowfields.*. Journal of fluid mechanics, **86**, 1978

Frank, E., and Yu. Q. Wassen, 1998, *Lagrangian prediction of disperse gas-particle flow in cyclone separators*. Third international conference on multiphase flow, Lyon, France June 8-12, 1998. CD-ROM, Paper No. 217

Fu, S., P.G. Huang, B. E. Launder, & M.A.Leschziner, 1988. *A Comparison of Algebraic and Differential Second-Moment Closures For turbulent Shear Flows with and without Swirl*. Transactions of the ASME **110**, June. 216-221

Garg, A. K., & S. Leibovich, 1979, *Spectral characteristics of vortex breakdown flowfields*, Physics of fluids, **22**, 1979, 2053-2064

Gouldin, F.C., J.S. Depsky, & S-L. Lee, 1985, *Velocity field characteristics of a swirling flow combustor*. AIAA Journal **23**, 95-102

Gupta, A. K., D.G. Lilley, & N.Syred, 1984, *Swirl flow*, Energy and Engineering Science Series

Hall, M.G., 1966. *The structure of concentrated vortex cores*. Progress in Aeronautical Sciences. **7**, 53-110

Hanjalic,K., 1994, *Advanced turbulence closure model: A view of current status and future prospect*. Int. J Heat and fluid Flow. **15** June 178-203

Hargreaves, J.H., & R.S. Silvester, 1990. *Computational fluid dynamics applied to the analysis of hydrocyclone performance*. Trans IChemE,.**68**, Part A, 365-383

Harvey, J.K. 1962. *Some observations of the vortex breakdown phenomenon*. J. Fluid Mech. **14**, 585

Hoffmann, A.C., de Groot, & M. Hospers, A.1996, *The Effect of the Dust Collection System on the Flow pattern and Separation Efficiency of a Gas Cyclone*. The Canadian Journal of Chemical Eng., **74**, 464-470

Hsieh, K.T., & R.K. Rajamani, 1991. *Mathematical Model of the Hydrocyclone Based on Physics of Fluid Flow*. AIChE Journal, **37**(5), 735-746

Janjua, S. I., and D. K. MaLaughlin, 1986, *An experimental study on swirling confined jets with helium injection*. Rept. DT-8562-01, Dynamics Technology, Inc, Torrance, CA

Kessler, Marc & D. Leith, 1991, *Flow measurement and efficiency modeling of cyclones for particle collection*. Aerosol Science and Technology, **15**, 8-18

Kim, W.S., & J.W.Lee, 1997, *Collection efficiency model based on boundary-layer characteristics for cyclones*. AIChE Journal, **43**, 2446-2455

Kopicky, R.M. & K.E. Torrance, 1971, *Initiation and structure of axisymmetric eddies in a rotating stream, Computers and Fluids*, Computers and Fluids, **1**, 289

Kumar, R., T. Conover, 1993. *Flow visulization studies of a swirling flow in a cylinder*. Experimental Thermal and Fluid Science, **7**, 254-262

Leibovich, S., 1984, *Vortex stability and breakdown: survey and extension*, AIAA Journal, **22**, 1192-1206.

Lessen, M., P. J. Singh, & F. Paillet, 1974, *The stability of a trailing line vortex Part I. Inviscid Theory*, Journal of Fluid Mechanics. **63**, 753-763.

Linoya, K., 1953, *Study of the cyclone*, Memoirs of the Engineering, Nagoya University, **5**, 131-178

Loffler, F., M. Schmidt, & R. Kirch. 1991. *Esperimental investigation into gas cyclone flow fields using a laser-doppler-velocimeter*. Indusrie Minerale-Mines *et* carrieres, les Techniques. July. 149-156

Mees, P.A.J., 1997. *Three dimensional transient gas cyclone simulations*, 47th Canadian Chemical Engineering Conference. Oct. 5-8, Edmonton, Alberta. Paper 482.

Minier, J.P., Simomon, O., & Babillard, M. 1991. *Numerical modelling of cyclone separators. Fluidized bed combustion*. ASME 1251-1259.

Ogawa, A., 1997. *Mechanical separation process and flow patterns of cyclone dust collectors*. Appl Mech Rev **50**. 97-130

Reydon, R.F., & W.H.Gauvin. 1981. *Theoretical and Experimental Studies of Confined Vortex Flow*. The Canadian Journal of Chemical Eng.. **59**. 14-23

Squire, H. B. 1960. *Analysis of the vortex breakdown phenomena*. Part1 , Aero. Dept., Imp. Coll. Rep. No.102

Stairmand, C.J.. 1951. *The design and performance of cyclone separators*. Trans. Inst. Chem. E.. **29** 356-383.

Syred, N., & J.M. Beer. 1974. *Combustion in swirling flows: a review*. Combustion and flame. **23**. 143-201

ter Linden, A.J., 1949. *Investigation into cyclone dust collectors*. Proc. I. Mech. E.. **160**, 233-251.

Vu, B.T., & F.C. Gouldin, 1982, *Flow measurements in a model swirl combustor*, AIAA Journal, **20**, 642-651

Yap, C.L. 1987. *Turbulent Heat and Momentum Transfer in Recirculating and Impinging Flows*. Ph.D. Thesis. UMIST, Manchester

Yazdabadi, P.A., A.J. Griffiths, & N. Syred, 1994, *Investigations into the precessing vortex core phenomenon in cyclone dust separators*. Proc. I. Mech. E., **208**, 147-154.

Zhou, L.X., & S.L. Soo, 1990, *Gas-Solid flow and collection of solid in a Cyclone separator*. Powder Tech., **63,** 45-53.

Chapter 2: Experimental

In this chapter, the theory of laser Doppler anemometry, the LDA system used in this work, the experimental design, and the seeding methods for this high velocity field are discussed. A schematic diagram of the experimental equipment is shown in Figure 2.1. The main components are the LDA, the tank where the seeding particles are generated, the glass cyclone, and the blower that provides the airflow. Each of these components is discussed in turn.

2.1 The principle of laser Doppler anemometry (LDA) – an overview

With the invention of the laser in 1960 it was natural that people should start considering measuring the velocity of a material by means of the 'Doppler effect'. This technique allows the measurement of the local, instantaneous velocity of tracer particles suspended in the flow without disturbing the flow with a probe. It provides great advantages in recirculating flows, such as cyclones and in flows in ducts of small dimensions where mechanical probes can cause interference or blockage.

The basic principles of laser Doppler anemometry can be interpreted as follows: when a beam of light with a certain frequency reaches a moving object, the frequency of the light will be changed. To construct the LDA measuring volume, two laser beams are directed to the location at which the measurement of the velocity is required. The relation between the Doppler shift frequency f_D and the velocity of a moving object scattering the light is (Drain, 1980)

$$f_D = \frac{2V}{\lambda_0} \sin(\frac{\theta}{2}) \qquad (2.1)$$

where V is the velocity of the object, θ is the angle between two illuminating beams, and λ_0 is the wavelength of the light. By measuring the Doppler shift frequency for a given wavelength and beam angle, the velocity of the moving object can be determined.

In our lab, the LDA uses a 300mW argon-ion laser manufactured by Ion Laser Technology, operating at a 514.7 nm wavelength green beam. The system is one

component and uses forward scattering: scattered light is collected opposite the source of the light.

In our system, the dual beam or differential Doppler technique is used in which the measurement volume is illuminated by two focused, coherent laser beams of similar intensity and at beam angle θ intersection, as shown in Figure 2.2. The beams overlap to form an ellipsoidal measuring volume. The pattern of alternatively dark and bright planes with a known spacing is known as fringes. As each particle crosses the fringes, the intensity of light scattered onto the detector rises and falls at a frequency (f_D) directly proportional to the velocity.

The fringe spacing, δ_f, is dependent on the wavelength of the light λ_0, and the beam intersection angle, θ, and is given by

$$\delta_f = \frac{\lambda_0}{2\sin(\frac{\theta}{2})} \qquad (2.2)$$

In our case, the argon-ion laser provides the monochromatic and coherent light source. There are three different tracks, which provide three beam spacing and intersection angles. The two beams of equal intensity emerge from the transmitting optics through an $f = 500$ mm focal length lens and intersect at angles $\theta = 1.94$, 3.88, and 7.19 degrees, depending on which track is chosen, resulting in spacings of the interference fringes in the measuring volume of $\delta_f = 15.2$, 7.6, and 4.1 μm respectively. The number of fringes in the probe is $N = 18$. Most experiments were conducted on track 1, since it has a higher data rate.

In measuring recirculating or turbulent flows, the direction of velocity is unknown before hand. To avoid velocity direction ambiguity, a Bragg cell frequency shift is employed. The function of the Bragg cell is to introduce a fixed optical frequency shift f_o on one beam. The shifted beam has the same optical properties as the incoming beam and causes no deterioration of the performance of the laser Doppler system. Frequency shifting may

be described as a modulation of shifting frequency, $v_s = f_s \cdot \delta_f$, where f_s is the modulation frequency shift introduced, and δ_f is the fringe spacing. Thus a flow moving against the fringe pattern will result in an increase in the frequency of the light scattered from a particle in the measuring volume by an amount f_D, where f_D is the Doppler shift due to the particle motion. In other words, the detected frequency is $f_d = f_s + f_D$, taking into account the sign of f_D. For Aerometrics' Bragg cell transmitter system, a $40MHz$ frequency shift is set. Since the optical frequency shift is not infinitely adjustable, an electronic frequency shift, i.e. mixer frequency is employed after the photodetector. The electronic shifting increases the center frequencies of both Doppler spectrum and the pedestal. In our experiment, $35MHz$ was set for the mixer frequency, and a $10MHz$ low pass filter was applied to attain the velocity range from −30.4~ +30.4 on track 1.

2.2 Optical system

2.2.1 Optical configurations

The laser Doppler velocity measurement system consists of a laser, beam splitter, Bragg cell, focusing lenses, photodetectors, amplifiers and a signal processor, as shown in Figure 2.3. The two beams are derived from a continuous – wave laser beam using a beam splitting prism. They are then passed through a collimating lens. The Bragg cell applies a frequency shift to one beam. They are focussed by the transmitting lens onto the measuring volume. The measuring volume is intersected by the focal plane of the imaging system formed by the receiver and the photodetector aperture. Light scattered by a traversing particle is imaged on the photodetector. The resulting electrical signal is fed to a signal processor to extract the Doppler frequency. In our system, a Doppler signal analyzer (DSA) uses frequency domain burst detection to convert signals. The advantage of this method is that it can be successfully applied to a low signal to noise ratio signal.

2.2.2 Optical requirements and component measured in the study

In LDA, there are some optical limitations to successful measurement. A velocity measurement cannot be acquired in all places where the measuring volume can be located.

In LDA, two beams pass through the fluid and intersect to form the measuring volume. In the case of measurements in confined or internal flows, the incident beams pass from the air through a transparent wall or window before entering the fluid under consideration. The laser beams are refracted at the solid interfaces between these media. Sometimes, the refraction will produce a difference in optical path length between the two beams, and/or a change in the orientation of the beam angle bisector (thus measuring a different component of velocity than intended), as well as a change in the position of the measuring volume. (Kresta 1991)

For an experimental system with fixed refractive indices and tube radii, the refraction effects for measurement can always be calculated by applying Snell's law of refraction and ray tracing (Gardavsky *et al.* 1989). This is required to determine if the velocity component can be measured by LDA. In our system, before carrying out experiments, calculations were done to determine the accessible measuring locations and the velocity components actually measured.

Refraction effects in the cyclone are complex due to the curved and tilted geometry, since the cyclone geometry is composed of a cylinder and a cone. In the calculation, the cylinder is a planar geometry in the measurement of axial velocity, and a circular geometry for the radial and tangential components of velocity. There can be no difference in optical path length or deviation angle in measurement of the axial and tangential velocities in the cylinder because the two beams are always symmetric to the centerline (Figure 2.4A). Unlike the measurement of tangential velocity, the measurement of the radial component requires the two beams to be moved sideways with respect to the centerline, as shown in Figure 2.4B. In this case, the real bisector between the beams at the point of intersection is not always tangent to the circle but can be at a small angle ϕ, the deviation angle, as shown in Figure 2.5. The two beams may now have a difference in path length. A deviation angle results in the measurement of a small component of tangential velocity, along with the radial velocity. Although this angle is insignificant in the cylinder, the radial velocity measurement is unreliable since the tangential velocity is 100 times larger than the radial velocity.

In the cone, both beams will be bent upward for all orientations of the beams because the plane containing the two beams is no longer perpendicular to the conical surface, and therefore the real crossover point is not in the plane of the incident beams. Based on beam tracing calculations, there is still no optical path length difference or deviation angle for measurement of tangential velocity, and the optical path length difference is negligible for axial velocity measurement. For the radial velocity measurement, however, the optical requirement is not met. The largest deviation angle can reach 17 degrees, as shown in Figure 2.6. The further away the beams are from the center, the greater the deviation angle. Because of this large deviation angle, we cannot measure the radial velocity in the cone.

According to the calculations, axial and tangential components of velocity can be measured both in the cylinder and the cone. In our experiments, most measurements examine the axial flow in the gas outlet tube. Some tangential velocity measurements were conducted in the gas outlet tube, and a very few radial velocity measurements were carried out in the barrel. As mentioned in chapter 1, some tangential and axial velocity measurements have also been done in the cone. Several areas were not accessible. This may be due to the streaks in the cone of the glass cyclone that prevent intersection of the two beams after refraction at the cyclone wall.

2.3 Seeding design (seeding tank)

Laser Doppler anemometry (LDA) involves the measurement of a flow field, in either a liquid or a gas using light scattered by seeding particles. The signal generated by the scattered light is used to determine the particle velocity. When the velocity of a particle transported by the flow is taken to represent the fluid velocity, the ability of the particles to follow the flow becomes of great importance. If the particles are small, they are assumed to have the same velocity as the fluid. In liquids normally no problem occurs, as some small particles are always present. A more difficult situation occurs in the case of a gas that does not contain particles of any significant size. Artificial seeding must be added which should be done with reasonable cost. In some cases, for instance when the acceleration is high, as is the case in swirling flow, the size of the seeding is rather critical.

Particles whose motion is used to represent that of a fluid continuum should be

- able to follow the flow;

- good light scatterers;

- conveniently generated;

- cheap;

- non-toxic, non-corrosive, non-abrasive;

- non-volatile, or slow to evaporate;

- chemically inactive;

- clean.

Among all these factors, the most important one is the size of the particle. To determine the particle size, the analysis of particle motion relative to a viscous fluid by Hinze (1959) and Crane & Moore (1972) is followed. For particle motion in a centrifugal field, usually it is considered for the simple situation of the centrifugal force being balanced by the drag force, as mentioned in chapter 1

$$d_p = \sqrt{\frac{18\mu r}{\rho_p w}} \qquad (2.3)$$

For a water droplet rotating at 25m/s, the size of the particle required is about 3^μm, i.e. the trace or seeding particles which are smaller than 3^μm should be able to follow the gas flow. In practice, the particle size can not be determined strictly by the above calculation, since the rotating speed of the gas is unknown in the cyclone. The seeding problem can only be solved by trial and error.

In our system, we initially used nebulizers to provide water mist for seeding particles. Two sets of nebulizers were built. The first was placed just in front of the motor exit in order to saturate the ambient gas. The second one was placed 1 meter away from the cyclone inlet to provide the seeding particles. For measuring only inlet velocities, this kind of seeding method is good enough for LDA. Unfortunately, the particle size is too large when we try to measure the velocities in the body of the cyclone. Some of the large

water droplets impinge on the wall of the transporting hose due to the inertia of the denser water droplets. Some of the particles are larger than the critical separation size, so they stay in the outer downward flow in the cyclone and get separated. Smaller particles have to be added into the system to measure the velocity near the center of the cyclone. Injecting the smoke of burning Chinese incense provides a good signal. This was achieved by lighting a bundle of incense at the inlet of the motor. After two minutes, however, the smoke covers the cyclone wall with soot so that measurements can no longer be taken.

Tests showed that solid carbon dioxide or liquid nitrogen combined with hot water generates very fine droplets. The mechanism that drives the drop generation is proposed as follows: as the solid carbon dioxide vaporizes, it has to absorb large amount of heat from the environment. As this happens, the moisture in the air condenses. The white fog generated is composed of water mist rather than carbon dioxide. The particle size of mist is in the size range of $1\sim10\mu m$ by PDPA measurement. In the experiment. the gas flow rate is very high. The corresponding seeding generation rate has to be very high as well. The higher the rate of heating the solid carbon dioxide, the higher the seeding generation rate. Calculations showed that the required heating duty for seeding is about 40 kW. This amount of heat can only be supplied using steam.

The seeding used was mist in the size range of $1\sim10\ \mu m$ generated by solid carbon dioxide mixed with steam. A 60cm tall, 30cm diameter stainless steel tank was built to contain the solid carbon dioxide. Steam entered at the bottom. A perforated pipe distributor was used in the tank to provide uniform distribution of steam, as shown in Figure 2.7. To some extent, adjusting the steam valve can control the seeding flow rate. During the experiment, dry ice can only fill one-third of the tank, since too much dry ice will freeze the water in the distributor and block the steam. The extra room in the dry ice tank is designed to serve as a plenum chamber to eliminate the velocity or pressure fluctuation from the upstream flow, so the inlet velocity in the cyclone is only dependent on the pressure in the tank. Two narrow passages were mounted at the top of the tank to feed the seeding particles into the main hose. Each day, 50lb dry ice were delivered from Praxair company to run the seeding equipment.

23

To make optimal use of the mist, i.e. without any waste of mist in the hose before it reaches the cyclone, the mist was fed to the air 1m in front of the cyclone inlet. This consideration can be explained as follows: the relaxation time for a 1$^\mu$m mist droplet is about $300 \times 10^{-6} s$. Since 99% of the free velocity is obtained in five times the relaxation time, only 0.05m is required for the particle to reach the gas speed. For the flow in the pipe to become fully developed, the length needed is about 10 times the pipe diameter (Kundu 1990). Since the diameter of the transporting hose is 3 inches, only 0.75m is required to reach fully developed flow. Therefore. one-meter of pipe is enough for the seeding particles to reach the flow velocity and is also enough for the mean velocity to reach fully developed flow before the inlet to the cyclone.

The final flow process can be described as follows: Ambient air is supplied from the blower to the 3-inch hose. Having a volume of 0.043 m^3, the tank provides a uniform cascade exit pressure that maintains a constant flow rate of seeding particles. After the gas travels along the hose for 5 meters. it meets the seeding particles and is well mixed with mist which is supplied from the seeding tank. After 1m distance during which the flow becomes fully developed. the seeded gas enters the cyclone tangentially and imparts the swirling motion in the cyclone.

2.4 Cyclone model and blower

2.4.1 Cyclone model

The cyclone geometry used in this work is a 75% scaled-down cyclone based on Stairmand's geometry (Stairmand 1951). The dimensions of the glass cyclone are shown in Figure 2.8. The cyclone gas outlet diameter is half of the body diameter. This is based on balancing considerations on both efficiency and pressure drop. To prevent choking by collected dust and still maintain the required separation efficiency, the dust discharge is only a little narrower than the gas outlet. The cyclone inlet is in a rectangular shape, with the height of it approximately twice the width. To provide a smooth gas entry and reduce pressure drop, the inlet is no wider than the annular space between the gas outlet and the cyclone wall. The bottom of the gas outlet tube is flush with the bottom of the inlet. This may cause short-circuiting of the incoming gases directly to the outlet. The top of the gas

outlet tube is 265 mm above the roof of the cyclone. These cyclone parameters are specified with the design of a Stairmand type cyclone. In our experiment, three gas outlet tube diameters were used: 50 mm, 75 mm, and 95 mm, giving outlet diameter to barrel diameter ratios of 0.33, 0.50 and 0.63.

Since the cyclone inlet is rectangular in shape, a metal piece was used to connect the cyclone inlet to the circular cross section hose, as shown in Figure 2.9.

2.4.2 Blower

The selection of motor (blower) is based on the estimations of pressure loss in the cyclone, which occurs primarily in two regions: one is the inlet loss and friction within the cyclone, the second is the loss in the outlet pipe. The equations for these losses are given by Bhonet (1983):

$$\Delta P = (K_{fi} + K_{fo}) \frac{\rho V_\theta^2}{2}$$

(2.4)

in which K_{fi} and K_{fo} are functions of both cyclone geometry and inlet velocity. In our experimental cyclone, the pressure calculated from the above equation is about 1.5psi. Adding some margin to the pressure, a motor was chosen which can provide an inlet superficial velocity from 3~27 m/s and a pressure drop of up to 2psi. The speed of the motor can be varied by adjusting the percentage of the motor load on the motor drive.

An experiment was carried out to test the reproducibility of experimental data and also to calibrate the motor and fan. The calibration point was chosen near the center of the inlet tube where the seeding particles were present in abundance. By changing the percentage of the motor load, three determinations of inlet velocity were completed in the inlet, as shown in Figure 2.10. The sample size was 8000. These three lines were measured on three different days and they agree very well. The largest error calculated is less than 3%. The streamwise velocity increases parabolically with the motor frequency. The secondary flow, i.e. the velocity components that are perpendicular to the main flow, is less than 5%. The velocity distribution in the inlet at 90% motor load is shown in Figure 2.11. The

distribution is quite flat in the middle which shows that the flow is subject to considerable turbulence: velocity gradients only exist near the boundary.

2.5 Cyclone alignment

The cyclone is attached to a long arm that is mounted on the bench that is equipped with an x, y, z traversing mechanism (Figure 2.12). The bench can be moved horizontally by computer and controlled vertically by hand. Since only one of the velocities lying in the plane of the beam but perpendicular to the bisectors of the beam could be measured with a single-channel LDA, the measurement of either the tangential or the axial velocity component was made by rotating the plane of the beams. This was achieved by rotating the transmitter.

To obtain correct measurements, the optical system and the cyclone have to be properly aligned. This becomes more important in the cyclone, since the three velocity components have very different magnitudes (e.g. in some positions, $V_\theta \approx 30V_z$). For instance, when measuring the axial velocity at the centerline in the barrel part, the optical system should be oriented such that both beams are in a plane which passes through the axis of the cylinder, with the bisector between the beams at a right angle with axis. If the plane is slightly tilted from the axis, a combination of both axial and tangential velocities will be measured. Because of the large difference in magnitude of the velocity components, a one-degree deviation can cause a 50% error in axial velocity.

In our system, the transmitter of the laser was carefully aligned and rigidly mounted to the optical table. During focusing, the receiver is free to move on its optical table. The main challenge is to design and build a cyclone support. In order to take full advantage of the existing traverse system and have LDA measurements covering the whole length of cyclone, the cyclone was mounted on a long arm which is attached to the existing support, as shown in Figure 2.12. This can introduce disturbances. The inlet velocity is quite high (27m/s). The large momentum applied to the system due to the high flow rate can cause a slight movement and/or disturbance on the cyclone support. This disturbance can introduce a false frequency in LDA velocity records. Therefore everything has to be built rigid, and each experimental run requires careful leveling.

2.6 Experiment error prediction and equipment calibration

Accurate determination of LDA data is particularly difficult. Two aspects are to be considered. The first is the repeatability of data and the second is the absolute value of the velocity. The first is influenced mainly by the fluctuating nature of the signal and reproducibility of experimental conditions. The mean velocity measurement in the cyclone were repeatable to within 3%. The fluctuation data (rms velocity) could be greatly affected by different LDA settings. For instance, the low pass filter, whose function is to limit the high frequency noise band and remove the upper side band of the mixed signal, can alter the rms velocity if it is set too low. The value of the rms velocity from track one measurement was lower than that from track two and track three due to the large fringe spacing for track one. In order to have a consistent influence from the settings, the LDA parameter settings were kept the same. In spite of this, repeatability of the rms velocity was within 10% which is remarkably high. The vibration of the cyclone due to the high velocity may contribute to the high error of rms velocity. Absolute value determination is to be affected predominantly by the ratio of the measurement time scale relative to the real flow time scale. This is complicated by the presence of multiple time scales. Fortunately, by setting the measuring time long enough and getting enough samples, the velocity can cover more than 100 cycles of the lowest frequency component we are interested in to avoid velocity bias.

In the experiment, the mean data rate is of the order of 150Hz to 4000Hz, depending on the location of the probe in the cyclone. As the probe approaches the outside walls, there are more particles, and the data rate rises. In each measurement, 8000 instantaneous velocities were recorded with a validation rate of approximately 65~85%. The signal sampling rate is set at $40MHz$. The signal sampling rate does not affect the measurement as long as it is at least twice as much as the Doppler frequency ($f_D = 1.8MHz$). Zhou (1996) carried out the initial experiment validation. He reported that a sample size of at least 4000 is required to obtain accurate and stable measurement of velocities in a stirred tank. Since the LDA settings for a cyclone are totally different from those for a stirred tank, repeatability tests in terms of sample size were conducted. Figure 2.13 shows that a

sample size of approximately 5000 is required to obtain repeatable results in the cyclone. The final LDA settings are shown in Table 2.1:

2.7 Conclusion

A glass cyclone was built in the lab with the gas flow provided by a blower. Since LDA is used for the velocity field measurements. much effort has been spent on solving the seeding problem during the setup. Mist generated by solid carbon dioxide combined with steam was the solution for most experiments. Instrument calibration was carried out and experimental repeatability was also tested with great care.

Table 2.1 Velocity setup:

High voltage (V)	450
Frequency shift (MHz)	40
Sampling rate (MHz)	40
Sample size	8000
Validation	65%-85%
Velocity range (m/s)	-30.4-30.4
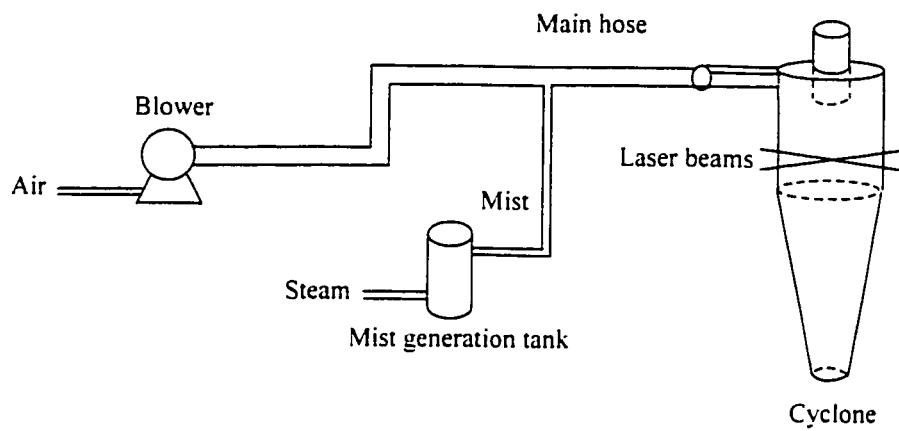
Figure 2.1. Schematic diagram of experimental

setup
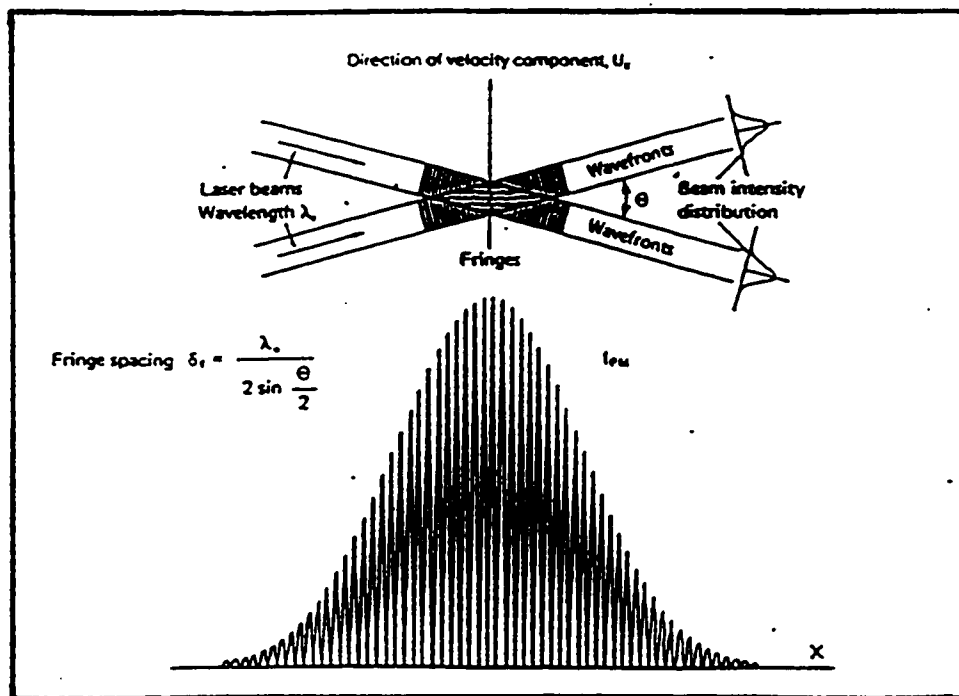
Figure 2.2 LDA measuring volume as envision by the
fringe interpretation (from George,1988)
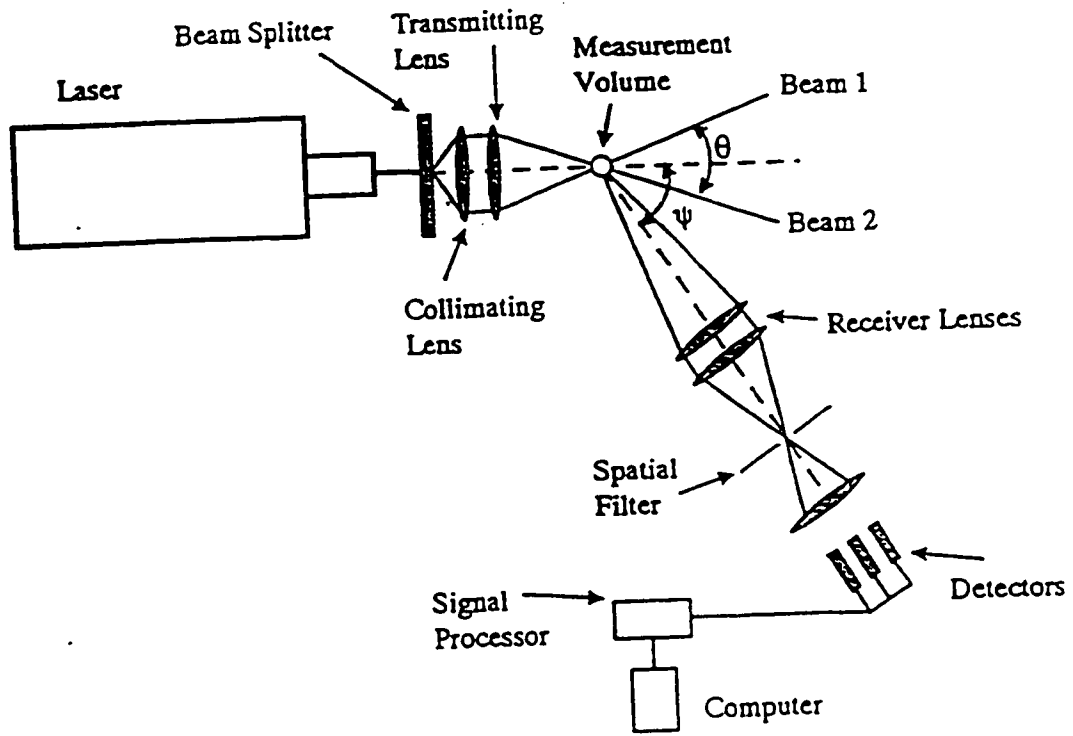
Figure 2.3 Schematic of the Aerometrics LDA optical configuration
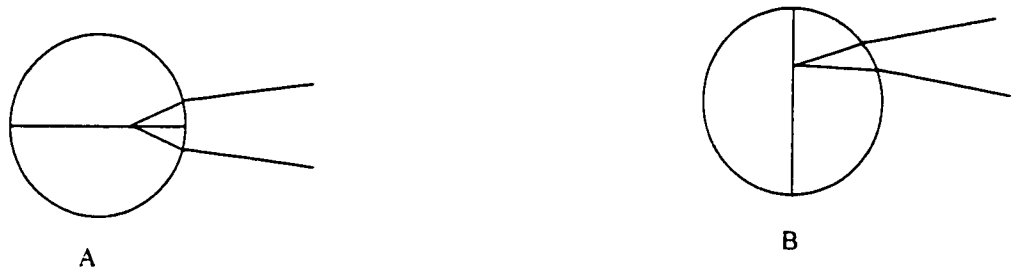
Figure 2.4 Beam orientation

    A: Measurement of tangential velocity

    B: Measurement of radial velocity
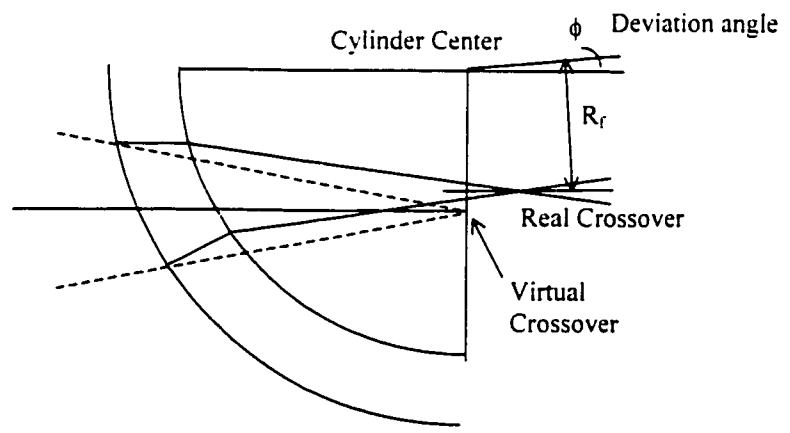
Figure 2.5 Refraction of laser Doppler anemometer beams during

    measurement of radial velocity. (Broadway & Karahan 1981)
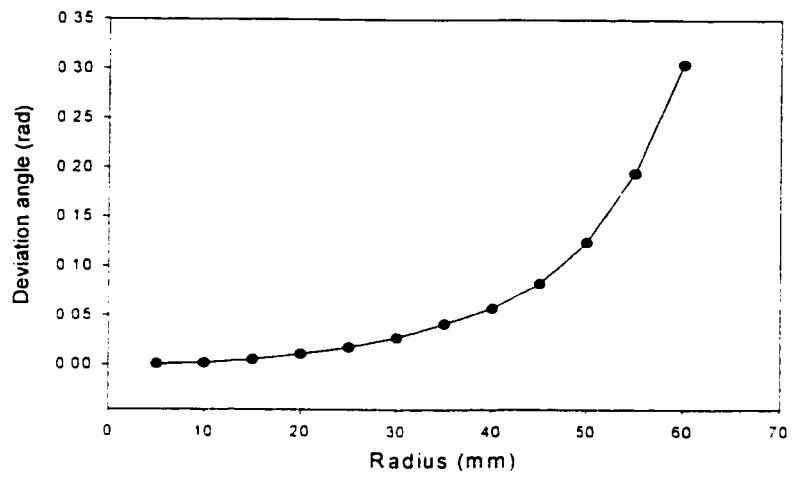
Figure 2.6 Deviation angle in the cone of cyclone when measuring
radial velocity at z=300 mm from the bottom
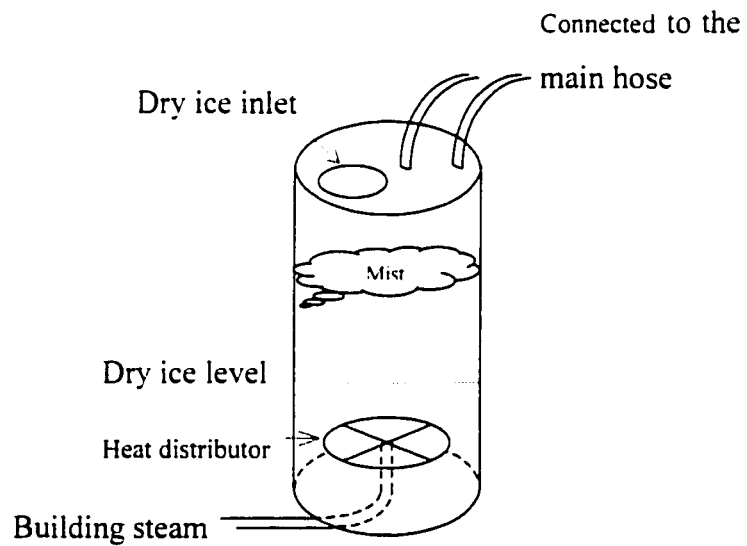
Figure 2.7 Diagram of dry ice

0.075

0.265

0.075

0.225

0.075

0.035

0.225

0.15

0.375

7.29°

Units: meter

0.054
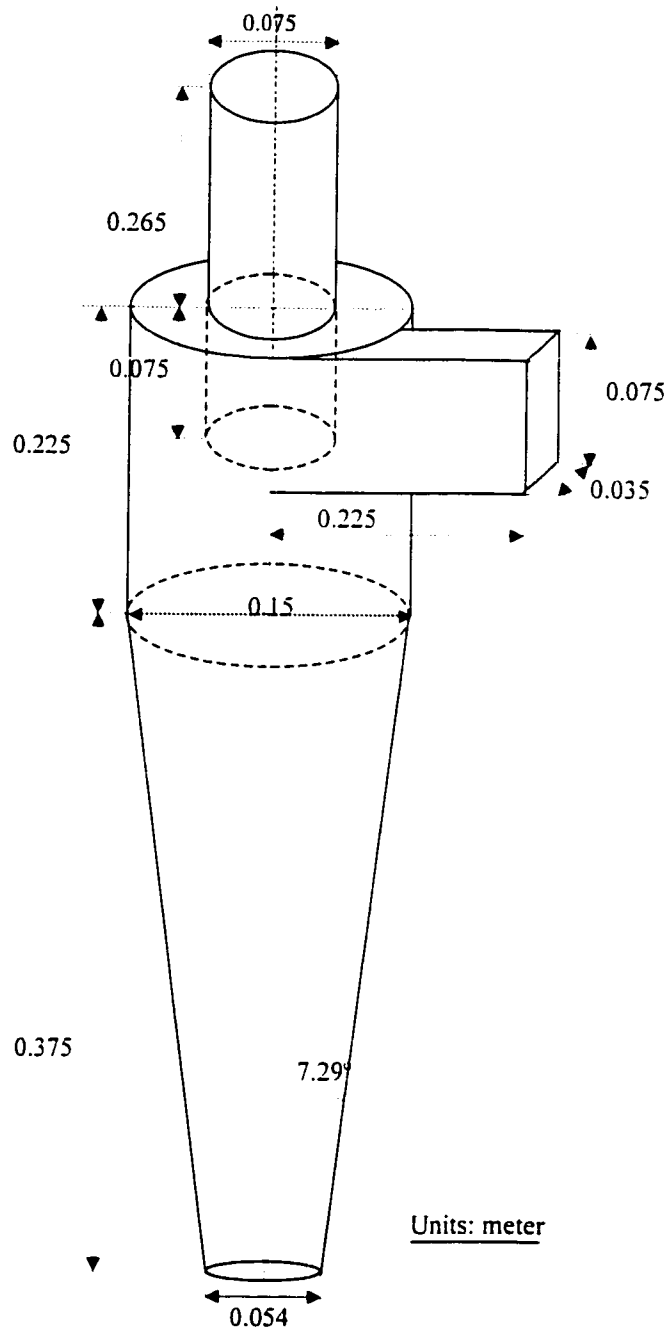
Figure 2.8 Cyclone model in lab (dimensions are in meters)

Seeding in

Cyclone inlet

3 inch

1 meter
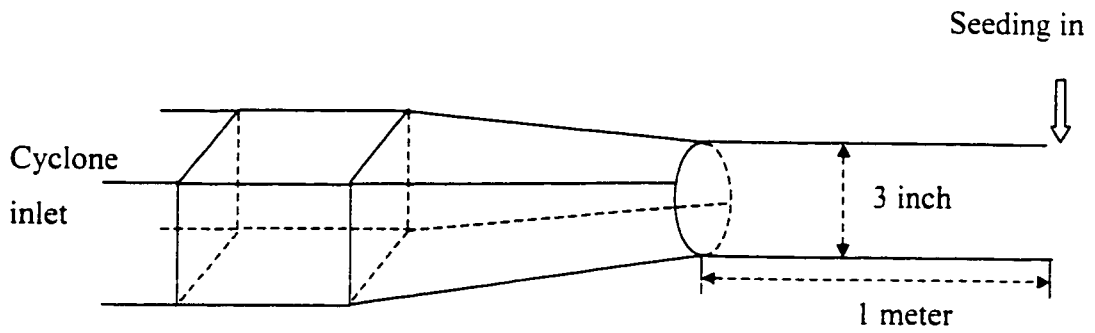
Figure 2.9 The connection of cyclone inlet to hose

% of the motor full load
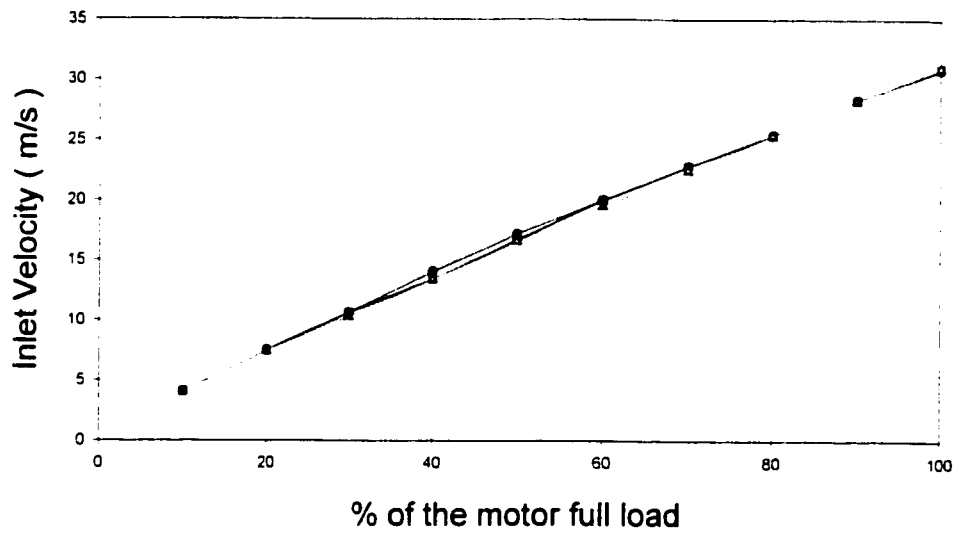
Figure 2.10 Repeatability and calibration of the inlet velocity
The velocity measurements were taken at x/a =0.5 and y/b=0.5 ,
where a and b are the width and height of the inlet
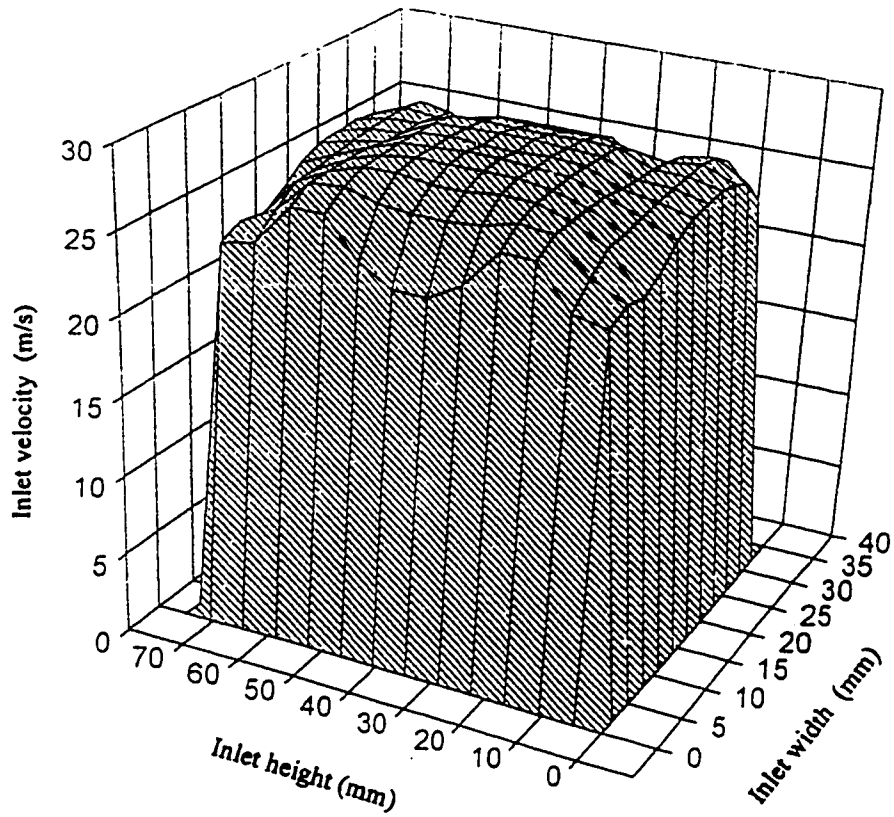
Figure 2.11 Inlet velocity distribution at motor load =90%
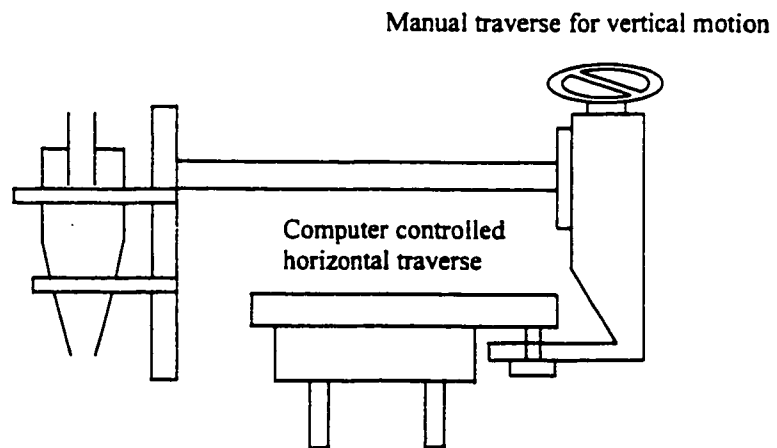
Figure 2.12 Cyclone supports and traverses
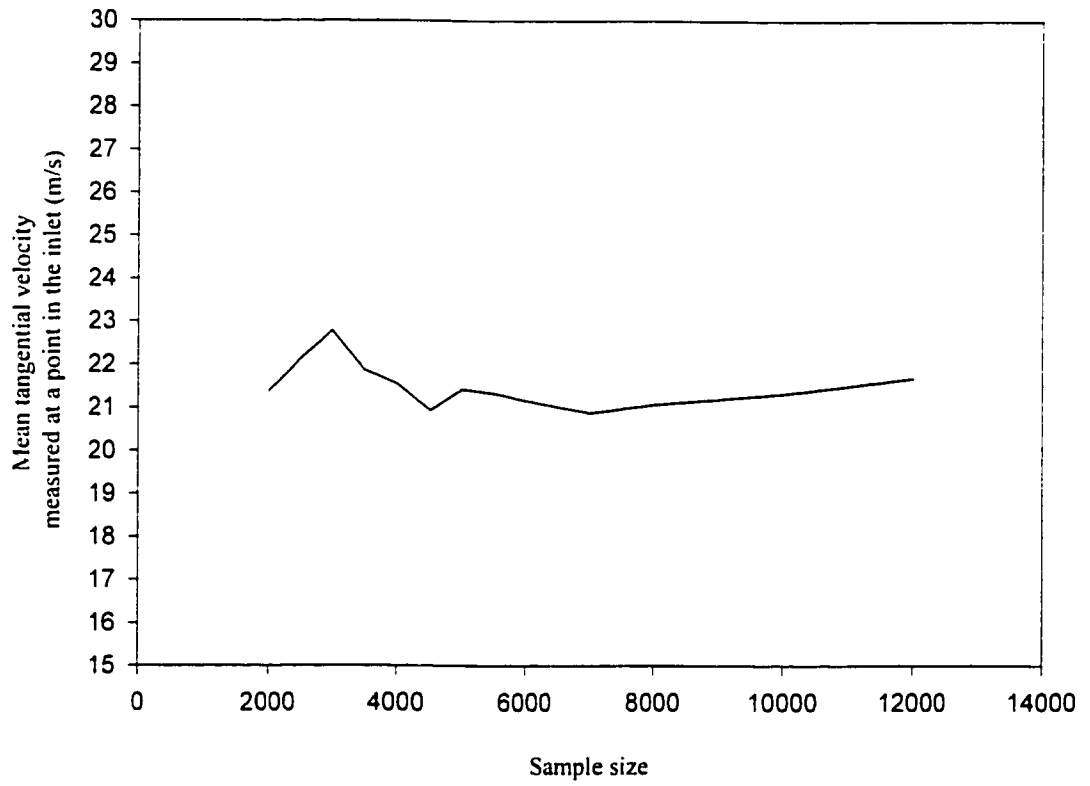
Figure 2.13 Tangential velocity measurements with varying sample size.
Each point in the figure is obtained by averaging values of 3 runs

Reference

Bhonet M.,1983, *Design methods for aerocyclones and hydrocyclone*, Chapter 32 in handbook of Fluids in motion. Ann Arbor Science

Broadway John D. & Emin Karahan, *Correction of laser Doppler anemometer readings for refraction at cylindrical interfaces*. Disa Information #26, February 1981

Crane R.I. & M.J. Moore, 1972, *Interpretation of pitot pressure in compressible two-phase flow*. J.Mech.Eng.Sci. **14**.128

Drain L.E., 1980, *The laser Doppler technique*. John Wiley and Sons, Toronto

Dring, R. P., 1982, *Sizing criteria for laser anemometry particles*. J. Fluids engineering. 104, p15-17

Gardavsky J., J.Hrbek, Z.Chara, and M.Serera, 1989, *Refraction corrections for LDA measurements in circular tubes within rectangular optical boxes*. Dantec Information. measurement and analysis, no.8.

George W.K., 1988, *Quantitative measurement with burst-mode laser Doppler anemometer*. Exptl. Thermal and Fluid Sci.1,

Hinze J.O. 1959, *Turbulence: an introduction to its mechanism and theory*. McGraw-Hill, New York

Kresta S. M., 1991, *Characterization, measurement and prediction of the turbulent flow in stirred tanks*, pp281. Ph.D thesis

Kundu, K. Pijush, 1990, *Fluid mechanics*, Academic press, San Diego, California.

Zhou G., 1996, Characteristics of turbulence energy dissipation and liquid-liquid dispersion in an agitated tanks. Ph.D thesis, University of Alberta, Edmonton, Alberta

Chapter 3: Experimental results

In this chapter, velocity field measurements will be discussed. Before presenting the experimental results, the techniques used to analyze the frequency and oscillations in local velocity are introduced.

3.1 Data analysis technique

In this study, spectral analysis is used to analyze the low frequencies in the velocity field. The instantaneous velocity signal of a turbulent flow can be interpreted as the sum of a wide spectrum of frequencies. The relative contributions of the individual frequencies to the sum are represented by the frequency spectrum or spectral density. The power spectral density (PSD) and the autocorrelation function provide powerful information for a physical interpretation of the dominant frequencies and time scales in the flow field. The PSD gives the energy or power content of the signal in a specified frequency band. The autocorrelation gives a measure of the extent to which a signal correlates with a displaced version of itself in time.

The estimation of frequency spectra from the LDA signal is very important in determining the frequencies present in turbulent flows and their associated time and length scales. When the data are evenly spaced, the fast Fourier transform can be used directly to process the raw signal to obtain the PSD or autocorrelation function coefficient. In our DSA (Doppler signal analyzer), the particles cross the measuring volume at irregular time intervals; hence, the conventional spectral estimates based on constant sampling rates must be modified. This was achieved using a slotting averaging technique.

3.1.1 Alias free sampling

It is well known that the spectrum of a signal can be obtained unambiguously from equi-spaced sampled data only if the signal has been sampled fast enough. To avoid the aliasing of high-frequency energy down to lower frequencies, it is necessary to sample at a rate equivalent to twice the frequency above which the signal energy content is negligible. This is generally called the Nyquist criterion (Wills, 1991). In our system, the

average data rate is 2 kHz, and the highest frequency of interest in the flow is about 500 Hz, therefore, the sampling frequency allows us to sample fast enough to avoid aliasing of the coherent low frequency. Aliasing of turbulent high frequency contributions could not be avoided

3.1.2 Turbulence power spectrum

The power spectrum is a decomposition of the measured velocity into different waves of different frequencies or wavenumbers. The value of the spectrum at a given frequency (or wavelength) is the mean energy in that wavelength. The power spectral density (PSD) gives the energy content of the signal in a specified frequency band.

The one-dimensional spectral density $E_1(f)$ for the crossflow fluctuating velocity u_1 is given by (Hinze, 1975):

$$\overline{u_1^2} = \int_0^\infty E_1(f)df \tag{3.1}$$

in which f denotes frequency. The energy spectrum, $E_1(f)$, is a continuous function in the frequency domain. However, the spectrum is made up of eddies of discrete sizes. When turbulence is analyzed by plotting $E_1(f)$ versus f, a peak is defined if there is a coherent periodicity in the flow (Reynolds, 1975).

3.1.3 Transformation to frequency domain using FFT

A physical process can be described either in the time domain, by the value of some quantity h as a function of time t, $h(t)$, or in the frequency domain, where the process is specified by giving its amplitude H (generally a complex number indicating phase also) as a function of frequency f, that is $H(f)$. For many purposes it is useful to think of $h(t)$ and $H(f)$ as being two different representations of the same function. The transformation from the time domain to the Fourier domain is defined as (Press et al., 1989, pg. 381):

$$H(f) = \int_{-\infty}^{+\infty} h(t)e^{2\pi ift} dt \tag{3.2}$$

$$h(t) = \int_{-\infty}^{+\infty} H(f) e^{-2\pi ft} \, df \qquad (3.3)$$

where time t is in seconds and frequency f in Hertz.

Computational work using a Fourier transform involves a discrete list of measurements- $h_k(t)$, rather than a continuous function $h(t)$. Thus, the integral (3.2) in its discrete form is (Press $et.$ $al.$, 1989):

$$H(f_n) = \int_{-\infty}^{+\infty} h(t) e^{i2\pi f_n t} \, dt \cong \sum_{k=0}^{N-1} h_k(t) e^{i2\pi \, f_n t_k} \Delta t_k = \sum_{n}\sum_{k} h_k(t) e^{i2\pi n t_k} \, ^r\Delta t_k \qquad (3.4)$$

Equation (3.4) is the discrete Fourier transform of N points h_k where k denotes the point in the time domain and $k = 0, 1, 2, \ldots\ldots N\text{-}1$: n denotes the point in the frequency domain $f_n \equiv n / T$ and $n = 1, 2, \ldots\ldots N$; and $\Delta t_k = t_{k+1} - t_k$ is the sampling interval.

From equation (3.4), it is obvious that the discrete Fourier transform (DFT) involves N^2 complex multiplications. This number can be reduced with an algorithm called the fast Fourier transform (FFT), which involves data reordering by bit reversal order and the Danielson-Lanczos lemma. Data are subdivided into $N/2$ even-numbered and $N/2$ odd-numbered points and their discrete Fourier transform is calculated. This subdivision goes further down to 1. Thus bit-reordering data takes N operations, and the discrete Fourier transform of length 2,4,8... N takes $\log_2 N$, so that the whole algorithm takes $N\log_2 N$ operations. For large N, the difference between N^2 and $N\log_2 N$ becomes very significant.

The one-sided power spectrum may be calculated as:

$$PSD = |H(f)|^2 + |H(-f)|^2 \qquad (3.5)$$

when the function $h(t)$ is real, then $H(f) = H(-f)$, so that a factor of 2 is expected in the above equation. Since the quantity involved is not power, but the RMS velocity squared, the factor of 2 drops out.

3.1.4 Autocorrelation Function

The autocorrelation function of physical data establishes the correlation between values of the data at anytime and values at a future time. The autocorrelation function coefficient R_E (or autocorrelation) is calculated from the following equation with t the time delay between the two signals:

$$R_E(t) = \frac{\overline{u(\tau)u(\tau+t)}}{\overline{u(\tau)^2}} \qquad (3.6)$$

The autocorrelation function coefficient has the following relationship:

$$R_E(t) \to 1 \text{ as } t \to 0$$

The general character of the dependence of an autocorrelation coefficient on the time delay shows zero slope at $t = 0$. This can be justified as follows: the autocorrelation of a stationary random function of time must be an even function of t, symmetrical about $t = 0$. Turbulent motions are continuous, with the smallest scales still of finite size; hence there is a finite delay before the signal changes at all, and the curve is level at $t = 0$. However, in practice, the smallest scales are comparable to or smaller than the transducer resolution, and it is not possible to see this leveling out.

After computing the Fourier transform of the initial time series, the autocorrelation can be obtained by multiplying the FFT transform by its complex conjugate:

$$R_E(\tau) \equiv H_k H_k^* = |H_k|^2 \qquad (3.7)$$

where H_k is discrete Fourier transform and H_k^* is the complex conjugate of H_k. The inverse is also true.

3.1.5 Analyzing unevenly spaced data

For data taken at equi-spaced intervals in time, both the standard fast Fourier transform (FFT) and the discrete Fourier transform (DFT) can be used to yield spectral estimates. In this study, the FFT algorithm was used in order to save calculation time. Since the

particle arrival times in the LDA data are irregular, the data sets are sampled at random instants of time. The raw data must be reprocessed before the FFT can be applied.

Methods for computing power spectra from unevenly sampled data can be classified into two categories (Mees 1990): correlation based methods which calculate the power spectrum from the Fourier transform of the autocorrelation function, and direct methods which are based on a direct Fourier transform (DFT) of the data. There are several methods available to speed up the calculation of spectra from random data for both the correlation-based methods and the direct transform methods. The best-developed methods are the 'slotting' methods that quantize time intervals. This quantization procedure can be applied either to the arrival times of the original samples, or, alternatively, to the lag times associated with each pair of data samples. In either case the quantization results in the crossproducts associated with each pair of data samples being accumulated in 'slots' or 'bins' in the correlation plane. With the autocorrelation function determined, the FFT is obtained by transform.

In this study, the fast Fourier transform is applied directly to binned data to calculate the spectrum. This estimate is formed by dividing the measurement time into equi-distant intervals or slots. The LDA data consist of discrete points $U(t_i)$ at times t_i. The bin size was chosen to be at least $\dfrac{2}{f_{mean-sampling}}$, or on the average 2 points per bin. The equally spaced time series is obtained by taking the average of the velocity measurements in each bin. For empty bins, the value from the previous bin is used. Then, the mean velocity of all the bins is computed and subtracted from the velocity in each bin, giving the time signal a zero mean. Bin sizes of $\dfrac{2}{f_{Nyquist}}$ and $\dfrac{4}{f_{Nyquist}}$, were also tested. They gave the same peak location as before.

Since the new time sequence is expressed in terms of the equi-spaced lag time, an FFT can be applied directly. In our study, the power spectrum density was calculated using Eq. 3.5, while the autocorrelation function was calculated by applying the inverse Fourier transform to the product of the Fourier transform and its complex conjugate. The slotted

43

direct method is much faster than the DFT or the binned A/C method for high sampling rates.

3.2 Flow field measurements

To determine the possible existence and extent of reverse flow, and the transient flow characteristics, the time varying axial, tangential and radial velocities were measured at various locations in the cyclone. The axial velocity was measured inside or just outside the gas outlet tube along the centerline that is perpendicular to the inlet as shown in Figure 3.1. The radius of the centerline which is near to the inlet is defined as positive and the other half as negative. Some axial velocity measurements were also carried out in the cone. Tangential velocity measurements were conducted just outside the gas outlet tube and in the barrel for comparison with previous investigations. A few radial velocity measurements were taken just below the vortex finder to determine if there is short-circuiting in that area. The frequency of any oscillations was determined from a frequency analysis of the velocity time series. Three outlet tube diameters were used: 50 mm, 75 mm, and 95 mm, giving outlet diameter to barrel diameter ratios of 0.33, 0.50 and 0.63. The majority of the data reported here is for the case of $D_{outlet}/D_{barrel} = 0.50$ and for a motor load of 100%.

3.2.1 Inlet velocity

In Chapter 2, the inlet velocity profile and the calibration of the streamwise velocity in the centre of the inlet with motor load were discussed. Figure 3.2 shows the streamwise velocity in the center of the inlet at three different gas outlet tube diameters. The streamwise inlet velocities increase linearly or slightly parabolically with the percentage of full motor load. The parabolic curve could be due to a pressure drop increase at high motor loads. It is not surprising that the larger the diameter of the gas outlet tube, the higher the velocities at the same motor load. Since with a small gas outlet tube the pressure drop due to friction will be higher, the velocity will be reduced based on the mechanical energy balance. At a low motor load, the pressure drop is relatively low and is the same for all three gas outlet tubes, since pressure drop is proportional to the square of inlet velocity. Therefore, the discrepancy in streamwise velocities between different

44

gas outlet tube diameters only exists at high motor loads (Figure 3.2). If we extend the three lines to the axis, they pass right through the origin, indicating that there is no flow when the motor is off.

The velocity distributions in the inlet at different motor load and different gas outlet tube diameters were also measured. Figure 3.3 is representative of the inlet velocity distribution in the inlet showing fully turbulent flow. The superficial velocity at the inlet was calculated by the following procedure: time varying velocity is averaged at the four nodes of each rectangular area and is then integrated over this area to get a volumetric flow rate. A superficial velocity of the inlet is obtained by adding all the volumetric flow rates from each area and dividing over the inlet area, i.e. $\dfrac{\sum_{n} V_i \Delta A_i}{A_{in}}$. The streamwise superficial velocities with percentage of full motor load at different gas outlet diameters are shown on Figure 3.4.

Frequency analysis is applied to the inlet velocity records for comparison with the frequency spectrum of the velocity signals in the gas outlet tube. Figure 3.5 is a time series plot of the velocity signal at a typical point in the inlet. Figure 3.6 is a power spectrum plot. The abscissa is the frequency plotted on a logarithmic scale running from 0.1 to 400Hz. The ordinate is the power spectral estimate plotted on a logarithmic scale. The area under the spectrum estimate curve is the variance of the signal and thus represents the power of the fluctuations. Since there is no discernible peak in the spectrum, the flow is random. The autocorrelation function coefficient on Figure 3.7 does not show the presence of oscillations around the time axis, revealing that the flow is purely turbulent. All these indications provide confidence that there is no periodic motion in the inlet.

3.2.2 Axial velocity

3.2.2.1 Periodic motion detected

The periodic motions in the cyclone were studied using the time varying velocity record acquired with the LDA. A typical time series of the axial velocity, shown in Figure 3.8,

indicates a very regular periodic motion at 265 Hz. As mentioned before, a power spectrum is the frequency decomposition of the variance of the signal. A peak in the power spectrum estimate represents a coherent fluctuation at that frequency. The distinct peak in Figure 3.9 confirms that there is periodic motion in the flow field at this measuring point, leading to a clean oscillation at the same frequency in the corresponding autocorrelation function plot as shown in Figure 3.10. The data shown in Figure 3.8 - 3.10 were collected 50 mm below the top of the gas outlet tube and 32.5 mm from the center. Footnote h_{top} denotes the vertical distance from the measuring position to the top of the gas outlet tube. A positive value of h_{top} indicates that the measuring position is below the gas outlet tube, while a negative value of h_{top} indicates that the measuring position is above the gas outlet tube.

The regular oscillation observed in the gas outlet tube is the result of a large-scale coherent structure, rather than of random turbulent fluctuations. Hussain (1986) defined a coherent structure as follows: A coherent structure is a connected turbulent fluid mass with instantaneously phase-correlated vorticity over its spatial extent. That is, underlying the random, three-dimensional vorticity that characterizes turbulence, there is a component of large-scale vorticity which is instantaneously coherent over the spatial extent of a coherent structure. As a consequence of this definition, a turbulent flow can be decomposed into coherent structures and incoherent turbulence. Coherent structures play important roles in transports of heat, mass and momentum. Simulations have shown that the coherent structure or precessing vortex core in a cyclone takes on a helical shape (Mees 1997).

3.2.2.2 Oscillations at h_{top} = -2 mm, varying r

This vertical position is just above the top of the gas outlet tube. Figure 3.11, 3.12 and 3.13 show the power spectra for the axial velocity components at three different radial locations but the same vertical position. At r = 30 mm (Figure 3.11), there is one distinct peak at 260 Hz. At r = 20 mm (Figure 3.12), two peaks at 260 Hz and 510 Hz are noticeable with the peak of fundamental frequency higher than that for r=30mm. At r = 10 mm (Figure 3.13), the two amplitudes are once again a little higher than those at r =

20 mm in Figure 3.12, but the frequency is preserved. The area under the dominant frequency increases progressively as the measuring point moves toward the center. The larger area under the peak of spectrum near the center of the tube indicates that the oscillations are intense there. As mentioned before, the area under a frequency spectrum is equal to the variance or mean square of the fluctuating velocity components in a frequency range, so the power contained below the peak in the frequency spectrum is the contribution due to the flow fluctuations. The larger the area, the stronger the flow fluctuations. Since the spectral intensity scale is logarithmic in this study, it is possible that a large fraction of the energy contained in the flow fluctuations arises from coherent motions. The second peak in Figure 3.12 and Figure 3.13 is a harmonic of the fundamental frequency.

3.2.2.3 Oscillations at $r = 30$ mm, varying h_{top}

Figures 3.14 and 3.15 are the time series plots and corresponding spectral analysis of the velocity fluctuations at $r = 30$ mm and $h_{top} = -13$ mm (outside the cyclone). They show a periodic motion oscillating at a fundamental frequency of 260 Hz with a broad peak in the frequency estimate (Figure3.15). Figure 3.16 and 3.17 show the periodic motion at $h_{top} = -2$ mm but the same radial location. It is clear that the amplitude of the velocity fluctuation at $h_{top} = -2$ mm (Figure 3.16) is a little smaller than that of $h_{top} = -13$ mm (Figure 3.14). This lower amplitude is consistent with the smaller area of the dominant peaks in the power spectrum (Figure 3.17 compared with Figure 3.15). Figure (3.18, 3.19), (3.20, 3.21), (3.22, 3.23), and (3.24, 3.25) are time series and the corresponding spectra at $h_{top}=+40mm$, $+90mm$, $+110mm$, and $+135mm$. From the time series plots (3.18, 3.20, 3.22, and 3.24), the amplitudes of the velocity fluctuations are clearly decreasing and the energy contained in the frequency reduces at a rate of at least an order of magnitude consecutively (3.19, 3.21, 3.23, and 3.25). The progressively diminishing amplitude of velocity fluctuations and the decreasing area under the dominant frequency as the measurements move down the gas outlet tube at the same radial position establishes with a high level of certainty that the strength of the oscillations decays down the gas outlet tube. It seems that the oscillations vanish at the vertical location of $h_{top} =$

135 mm (Figure 3.24 and 3.25). This could be due to interaction with the wall which cause the coherent structure to lose its identity.

3.2.2.4 Averaged axial velocity

Since the flow is time varying, both the mean and fluctuating components of the velocity components are obtained by averaging over a period long (larger than 0.5 s) in comparison with one cycle time (less than 0.0056 s) of the lowest frequency component of significant magnitude that is present in the flow (the precessing vortex core). The time averaged axial velocity and the rms axial velocity profiles at h_{top}= -13 mm (top of the cyclone) are shown in Figure 3.26 and 3.27. In Figure 3.26, the mean velocity becomes negative in the center, indicating that, *on the average*, back flow exists in that region. Measurements show that the back flow can penetrate at least half way down the gas outlet tube as shown later on Figure 3.32. The magnitude of the rms velocity at this position (Figure 3.27) is quite high when compared with those at other vertical positions, indicating that the velocity fluctuations could be mainly due to the coherent structure. It also shows two regions with high velocity fluctuations. These regions coincide with the regions of high axial velocity gradients in Figure 3.26. This is expected, since velocity fluctuations induced by the precessing vortex core will, as a first approximation be proportional to the velocity gradients in the vortex core. The time-averaged flow appears to be asymmetric, which may be due to the asymmetry of the single inlet in our experiment. Note that the measuring range at this elevation is wider than the diameter of the gas outlet tube (75mm), since at this position (13 mm above the gas outlet tube), the flow undergoes a sudden expansion and there is still fluid flow beyond the confines of the tube diameter.

Figure 3.28 and Figure 3.29 are time averaged axial velocity and the rms axial velocity profiles at h_{top}=-2mm (at the top of the gas outlet tube). They have a similar shape to Figure 3.26 and 3.27. The difference is that the area under the two peaks of the averaged axial velocity profile (Figure 3.28) is a little smaller than that of h_{top}=-13 mm (Figure 3.26). This can cause a significant volumetric flow rate decrease since the two peaks are near the wall. Although the rms velocity peaks (Figure 3.29) still coincide with the high

axial velocity gradient in Figure 3.28, their values are a little smaller than those at h_{top} = - 13 mm (Figure 3.27). This is an indication of the decay of the oscillation in spite of the fact that the coherent structures are still energetic and dominant at this position (Figure 3.11 – 3.13)

In the gas outlet tube at a vertical position of h_{top} = 90 mm, the back flow region in Figure 3.30 has almost disappeared (one point indicating back flow), showing the downward mass flow rate is less than higher up in the gas outlet tube. The rms velocity profile, instead of showing two local peaks, is almost flat and randomly scattered in the center (Figure3.31), and the magnitude of the rms velocity is much less than that at the top of gas outlet tube. The rms velocity trend at this location is the same as reported by Boysan et al.(1983). One hypothesis to explain this variation is that both random and organized fluctuations contribute comparably to the measured rms velocity fluctuations.

At a vertical position of 135 mm from the gas outlet top, the time averaged axial velocity is shown in Figure 3.32. The rms velocity shows one peak at the center (Figure 3.33). This may indicate that the rms velocity at this elevation is mainly due to turbulent fluctuations. The decrease of the average rms velocity down the gas outlet tube is another confirmation of the decay of the oscillation. The values of averaged rms velocities at different elevations are shown in Table 3.1.

3.2.3 Tangential velocity

The tangential velocity was measured in the barrel at 0.415 m from the top of gas outlet tube (0.15 m from the cyclone roof). It shows the expected Rankine vortex shape (combination of a free vortex and a forced vortex) in Figure 3.34. The velocities measured in this work show the region of solid body rotation persisting much further out towards the cyclone wall than that reported by Boysan and co-workers (Boysan et al. 1983) at the same superficial gas velocity. The discrepancy could be due to the 75% scaling of our cyclone geometry dimensions. It can also contribute to the conservation of angular momentum. With a smaller diameter cyclone at the same inlet velocity, the tangential velocity has to increase to maintain the same angular momentum. This could cause a shifting of the maximum tangential velocity towards the wall.

3.2.3.1 Oscillations in tangential velocity

Frequency analysis was applied to tangential velocity time series to verify the frequency of the oscillations. Figure 3.35, 3.36 and 3.37 are plotted at a selected point just outside the gas outlet tube. The time series record shows vigorous periodic motion on Figure 3.35, the frequency spectrum (Figure 3.36) and autocorrelation function coefficient (Figure 3.37) indicate that the periodic motion has a fundamental frequency of about 260 Hz, identical to the oscillation frequency of the axial velocity fluctuation. The fact that the axial and tangential oscillation frequencies are the same confirms that the oscillations are caused by a coherent structure.

3.2.3.2 Oscillation damping in the barrel

Frequency analysis was also applied to the tangential velocity record in the barrel (Figure 3.38). No noticeable peaks are observed (as shown in Figure 3.39), although some irregular low frequency oscillations seem to be present in the time series record (Figure 3.38) and autocorrelation function (Figure 3.40). It is clear that periodic motions are greatly damped out in the barrel, if they exist at all. For a D_{outlet}/D_{barrel} ratio of 0.63, one broad peak can be observed in the frequency spectrum (Figure 3.41) although the coherent fluctuations revealed by the power spectrum was much less energetic (the PSD only reaches to 10^6) and only contain a modest proportion of the power contained in the flow fluctuations. For a D_{outlet}/D_{barrel} ratio of 0.33, the frequency spectrum does not show any distinct peaks (Figure 3.42).

3.2.3.3 Oscillations in the cone

To test if there are oscillations in the cone, a large number of runs were carried out in the cone (180 runs). A representative spectrum is presented in Figure 3.43. No peak of any significant magnitude can be detected. The autocorrelation function (Figure 3.44) looks like a combination of several dominant frequencies, indicating that the flow fluctuations could be more random. The velocity fluctuations in the cone with the other two gas outlet tube diameters yield similar spectra to this one.

3.2.4 Measurements at different inlet velocities

By setting the percentage of the full motor load on the motor drive, the inlet velocity can be changed. Figure 3.45, 3.46 and 3.47 show the continued existence of periodic motion in the flow field at a motor load of 50% (i.e. at about 13 m/s superficial inlet velocity). At this inlet velocity the oscillation has a fundamental frequency of 130 Hz. Experiments show that the frequency of the oscillations scales linearly with the superficial velocity of the inlet for all the three gas outlet tube diameters as shown in Figure 3.48. The different symbols along the regression lines denote different runs. If the lines are extended to zero frequency, they do not pass through the origin. This suggests that the coherent structure is lost at some point in the transition to laminar flow. The dimensionless frequency can be characterized using the Strouhal number, and it is a function of both Reynolds number and Swirl number. This will be discussed in detail in the dimensionless group analysis in the next chapter. Similar phenomena were also observed for the other two gas outlet tubes.

3.2.5 Measurements at different gas outlet tube diameters

Changing the outlet tube diameter greatly changes the frequency of the oscillations. Fig 3.49 shows that the frequency of oscillation at a selected point just outside the gas outlet tube with a D_{outlet}/D_{barrel} ratio of 0.33 is about 490 Hz. The time averaged mean and rms axial velocities at 2mm above the gas outlet for this ratio are shown on Figure 3.50 and 3.51. Figure 3.50 shows similarity with Figure 3.28, but the back flow region is slightly narrower. Experiments indicated that the back flow and oscillations only penetrate down to about 1/3 of the gas outlet tube. The shape of the rms velocity profile in Figure 3.51 is a little different from Figure 3.29. Near the wall, the rms velocities become higher. This may be because turbulence energy generation is higher near the wall.

The frequency of oscillation drops to 180 Hz when the diameter-barrel ratio is increased to 0.63 as shown in Figure 3.52. A possible explanation for the decrease of oscillation frequency with increasing gas outlet tube diameter is that when the passage narrows, the frequency of oscillation must increase in order to preserve the angular momentum of the vortex core, and vice versa. The time averaged axial and rms axial velocities (Figure 3.53

and Figure 3.54) show the same trends as those of the small gas outlet tube. Our experiments also show that the back flow can penetrate to the roof of the gas outlet tube of this gas outlet tube diameter.

Changing the diameter of gas outlet tube will change the swirl in the cyclone; this will be discussed in detail in the next chapter.

3.3 Discussion

3.3.1 The mechanism of back flow

As mentioned in Chapter 1, back flow or reverse flow is a well known phenomenon in highly swirling flow. In order to analyze the reverse flow using the Navier-Stokes equations, imposing axi-symmetry is unfortunately necessary. By doing so, the continuity equation can be expressed as:

$$\frac{1}{r}\frac{\partial(vr)}{\partial r} + \frac{\partial u}{\partial z} = 0 \qquad (3.8)$$

in which v is the radial velocity and u is the axial velocity.

The energy equation is given by:

$$\rho c_p[\frac{\partial T}{\partial t} + (v \cdot \nabla)T] = k\nabla^2 T + \mu[2(\varepsilon_{rr}^2 + \varepsilon_{\theta\theta}^2 + \varepsilon_{zz}^2) + \varepsilon_{\theta z}^2 + \varepsilon_{rz}^2 + \varepsilon_{r\theta}^2] \qquad (3.9)$$

in which the term in square bracket on the right hand side denotes viscous dissipation.

$$\varepsilon_{\theta z} = \frac{\partial w}{\partial z} \qquad (3.10)$$

equation 3.10 is viscous dissipation of swirl component on the axial direction when assuming θ independent.

$$\omega_r = -\frac{\partial w}{\partial z} \qquad (3.11)$$

and equation 3.11 is the vorticity component in the r direction.

In swirling flows, axial gradients are much smaller than radial gradients, so that the interaction of the pressure and the swirl may be examined using the quasi-cylindrical

approximation $\partial p / \partial r = w^2 / r$, in which w is the swirl velocity (Hall 1966). This equation expresses the balance of the centrifugal acceleration of a fluid volume with restraining pressure force. Integration with respect to r from axis to radius R, where $P_R =$ const, gives

$$P_R - P_0 = \int_0^R \frac{w^2}{r} dr \qquad (3.12)$$

followed by differentiation with respect to z, yields

$$\left(\frac{\partial p}{\partial z}\right)_{r=0} = -2 \int_0^R \frac{w}{r} \frac{\partial w}{\partial z} dr \qquad (3.13)$$

Since viscous dissipation of swirl (Eq. 3.10) or, equivalently, diffusion of vorticity (Eq. 3.11) is always less than or equal to zero, the axial pressure gradient will be positive (this is the adverse pressure) and will tend to decelerate the axial flow. However, $\left| w \frac{\partial w}{\partial z} \right|$ decreases slightly with z, so that shear forces are eventually able, after the initial flow retardation, to accelerate the flow in the core to the free stream velocity in both barrel and cone. When the flow enters the gas outlet tube, the axial velocity retardation arising from dissipation of the swirl is large enough to require a significant amount of radial outflow according to the continuity equation. Since, except for viscous effect, the angular momentum of a fluid particle is conserved as it moves radially outward, its swirl velocity must decrease. The reduction in swirl velocity resulting from radial outflow and diffusion is associated with a large increase in the pressure near the axis. The shear forces in the gas outlet tube are attenuated through friction with the wall and they may not be able to carry the flow in the core. At this point, the adverse pressure along the centerline is no longer negligible, and it can lead to reverse flow or back flow in the gas outlet tube. Grabowski & Berger (1976) mentioned that in the flow where the swirl velocities are not too large, the axial retardation may be such as to produce a region of flow in the vortex core unstable to certain spiral disturbances. This instability can be amplified to oscillations in the flow field.

Since we believe the dominant factor causing reverse flow to be the decline of swirl velocity in the gas outlet tube, it is possible to explain that the back flow can occur nearer to the top with a smaller gas outlet tube. In this case, due to angular momentum conservation through barrel to the gas outlet tube, the swirl velocity has to increase more in a small gas outlet tube to some extent. Therefore it may compensate the swirl loss which is caused by radial outflow so that the back flow may occur at a later stage.

3.3.2 Origin of coherent structure and asymmetric flow filed

For decades, people have tried to determine the origin of oscillations in highly swirling flows. Clark et al.(1990) stated that the coherent structures originate from the upstream boundary due to the interaction between different sizes of eddies, or due to the interaction between the eddies with the boundaries. They seem to retain much of their shape and character as they convect downstream, but eventually die out. Faler &Leibovich (1977) found that the increase of swirl will move the axial location of the oscillations upstream. In our case, the experimental results show that the coherent structures are the strongest at the top within the range of measurements, this may indicate that they are generated at the top somewhere, i.e. far downstream, which contradicts most of the phenomena observed in the literature. Squire(1960) applied wave theories to explain these structures which are generated downstreams. From his experiment he concluded that waves may propagate upstream from a downstream disturbance source (e.g. created by the tube exit). This seems to be the case in our study.

In this research, an unsteady three-dimensional asymmetric flow field has also been observed. Due to the single inlet of the cyclone, it is difficult to decide whether the asymmetric geometry or the oscillations contribute to the asymmetric flow field. Leibovich (1984) stated that flows which suffer breakdown can be made to have a high degree of axial symmetry, yet the flows in the breakdown zone lose symmetry.

3.3.3 Volumetric flow rate

The volumetric flow rate Q is defined as follows when assuming axi-symmetric flow:

$$Q = \int_{area} UdA = \int_0^R U \cdot 2\pi r dr \qquad (3.14)$$

where U is the mean axial velocity. By averaging the two sides of the axial velocity profile at each cross-section and applying the above integration, an approximation of the volumetric flow rate at different elevations can be obtained. Calculations show that the volume flow rate increases up the gas outlet tube as shown in Table 3.1. This is because the gas in the cyclone is pressurized. Towards the exit of the gas outlet tube, the pressure is converted to kinetic energy, hence increasing the volumetric flow rate.

3.3.4 Momentum balance

The axial momentum conservation in each cross section can be expressed as follows:

$$M = \int_0^R (U^2 + \overline{u'^2} + \frac{P}{\rho})r dr \qquad (3.15)$$

where $\overline{u'^2}$ is the averaged axial fluctuating velocity. Neglecting the pressure term, the first two terms represent the total axial momentum in the cyclone.

$$M = \int_0^R (U^2 + \overline{u'^2})r dr \qquad (3.16)$$

LDA measurements of the separate velocity terms allows direct calculation of momentum according to the equation. By calculation, a significant increase in momentum up the gas outlet tube is observed . This is consistent with the presence of a negative pressure gradient acting to accelerate the flow.

The momentum was calculated at four vertical positions: $h_{top} = -13$ mm, $h_{top} = -2$ mm, $h_{top} = 90$ mm and $h_{top} = 135$ mm with $D_{outlet}/D_{barrel} = 0.50$. Up the gas outlet tube, momentum at $h_{top} = 135$ increases in this region of up to 28% compared with that of $h_{top} = 135$ mm were found. These momentum increases were opposite to the decrease in static pressure, thus giving the necessary conservation of momentum embodied in the Navier-Stokes equations.

It is of interest to note that at h_{top} = -13 mm, the momentum carried by the mean motion (first component of momentum integral in Eq. (3.16)) is 2.7 times that carried by the streamwise fluctuations. On the other hand, at h_{top} = 135 mm, the momentum of the mean motion is 20 times that of the turbulence contribution. This is because most of the momentum associated with the fluctuation term is in the periodic component (precessing vortex core), which dominates the flow at the top but has decayed to almost negligible levels down the gas outlet tube. Thus, momentum increase due to the pressure effects and significant transfer of momentum takes place from the periodic component to the mean flow in the gas outlet tube.

3.4 Conclusions

A detailed experimental investigation was carried out to determine the effects of inlet velocity and gas outlet diameter on the back flow and coherent large-scale oscillations observed in the flow field. The results have shown the existence of a well-defined, energetic low-frequency oscillations (precessing vortex core) and reverse flow for all gas outlet tube diameters to barrel diameter ratios tested (0.33, 0.50 and 0.63).

Frequency spectra and autocorrelation functions show that at a given velocity, the oscillating frequency does not depend on the measurement location. In all three-diameter gas outlet tubes, the back flow and oscillation decayed down the gas outlet tube. The frequency of the oscillations is dependent on the flow rate and the diameter ratio D_{outlet}/D_{barrel}. For all gas outlet tube diameters, the oscillations were observed over a wide range of velocities with a frequency that scales linearly or slightly parabolically with the inlet flowrate.

The oscillations contribute significantly to the high fluctuation levels at the top of the gas outlet tube. They may derive their energy from a fluid dynamic instability and originate at the top of the gas outlet tube. The fluctuation magnitudes vary considerably in the gas outlet tube. At the top, they are intense and dominate the flow, while down the gas outlet, they are negligibly small. The two peaks of axial fluctuating velocity are in agreement with the steepest velocity gradient in the averaged axial velocity.

Table 3.1: Mass flow ratio and averaged rms value at different elevations

	Mass flow ratio as a percentage of inlet mass flowrate	Averaged rms along the cross section of the elevation (m/s)
h_{top} = -13 mm	120%	12.85
h_{top} = -3 mm	102%	9.027
h_{top} = 90 mm	98%	5.088
h_{top} = 135 mm	94%	4.085
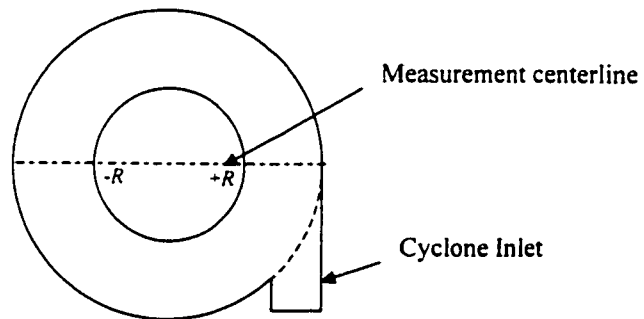
Figure 3.1: Measurement positions in experiments
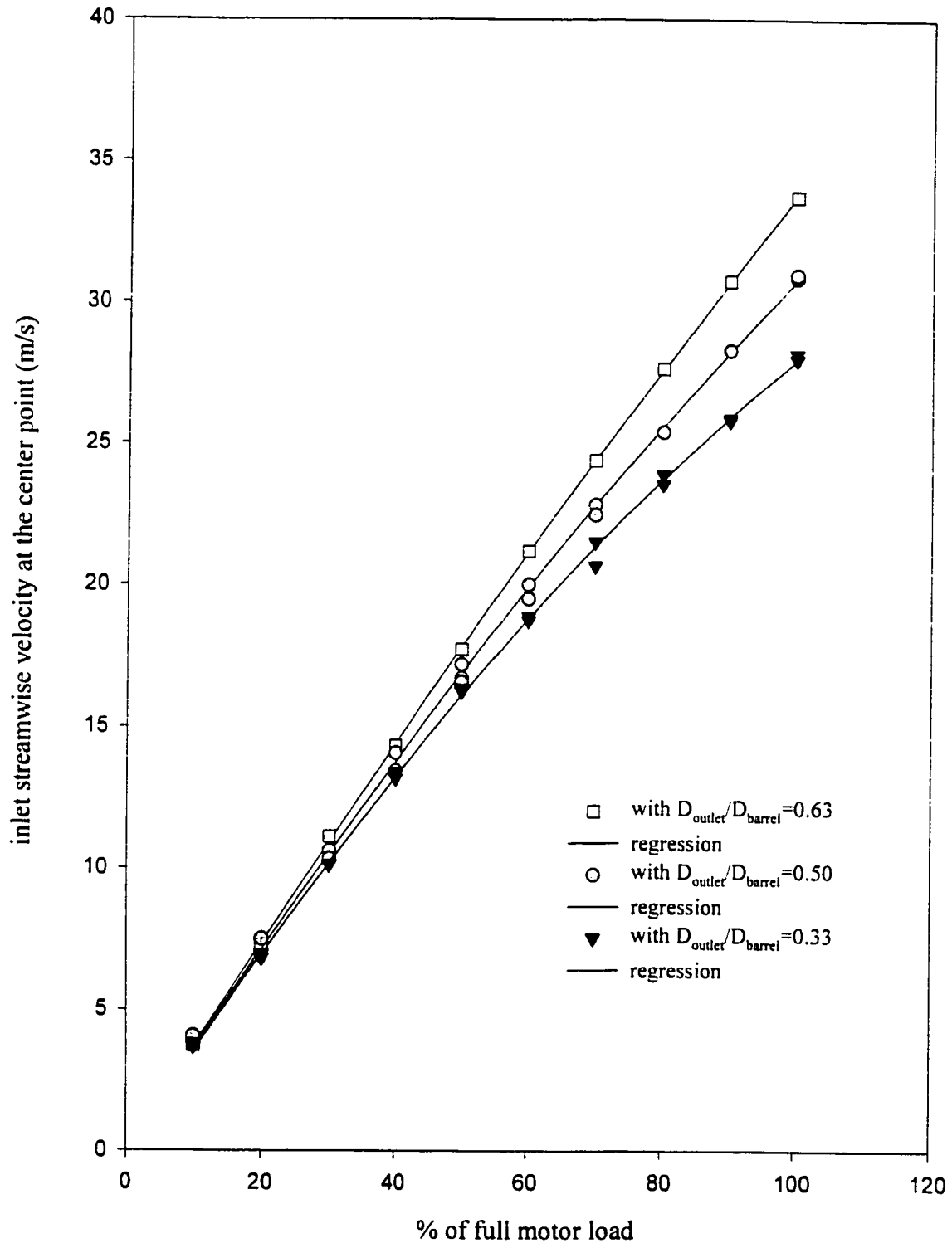
Figure 3.2 Repeatability and calibration of inlet velocity for different diameter of gas outlet tube. The velocity measurements were taken at x/a=0.5 and y/b=0.5, where a and b are the width and height of the inlet
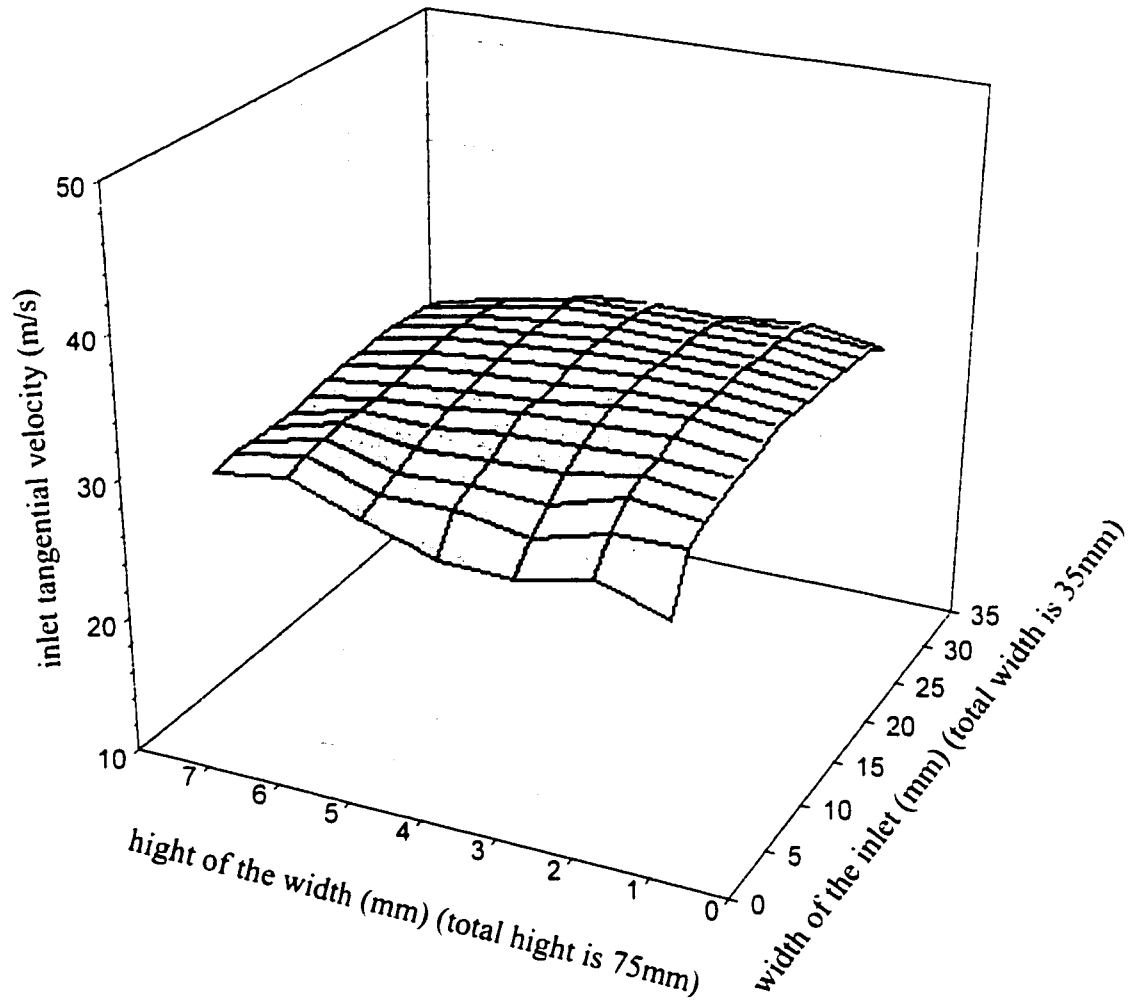
Figure 3.3 Inlet tangential velocity profile at 100% motor load
(with $D_{outlet}/D_{barrel}=0.63$)
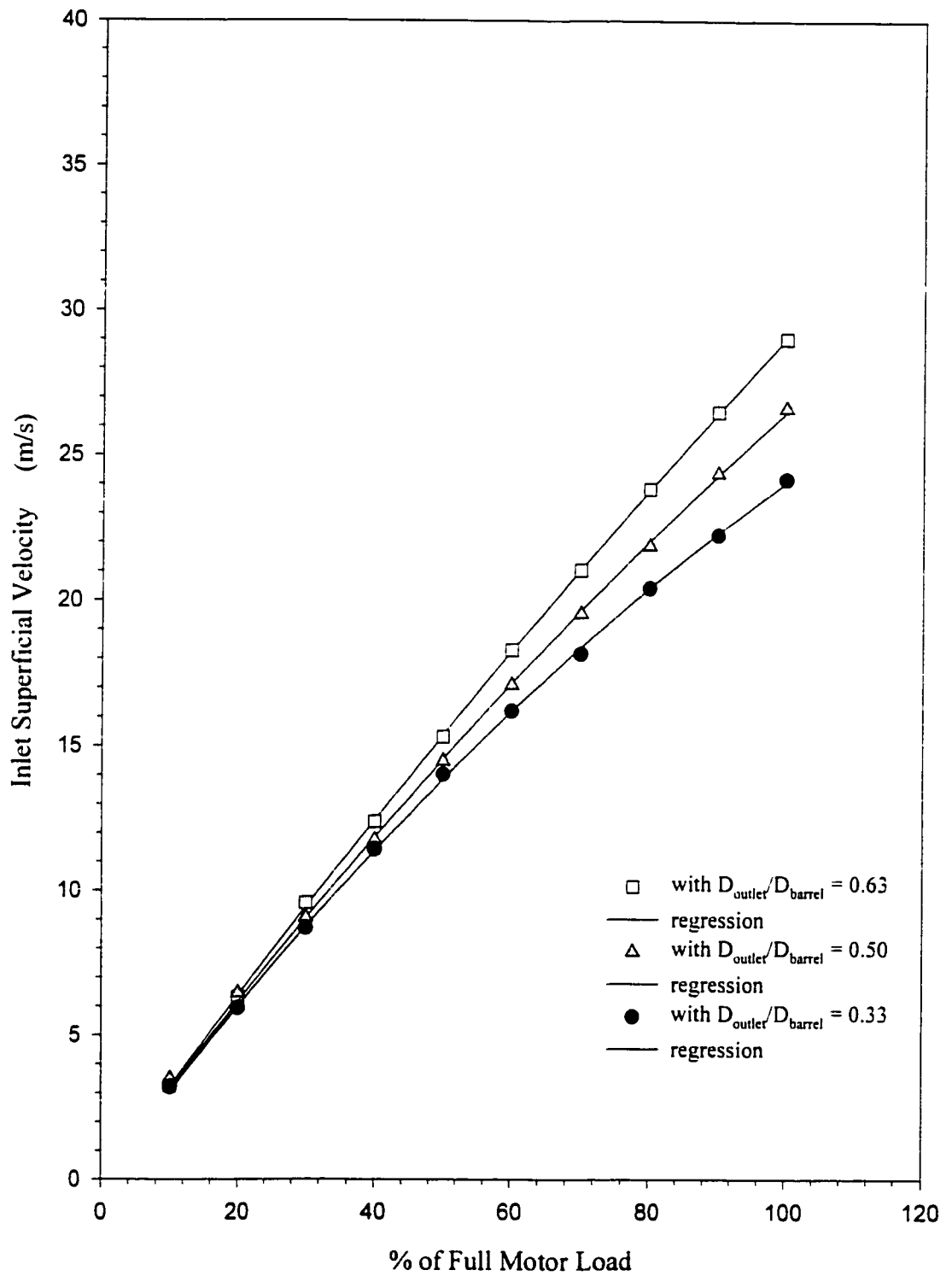
Figure 3.4: Inlet superficial velocity at three different
gas outlet tube diameters
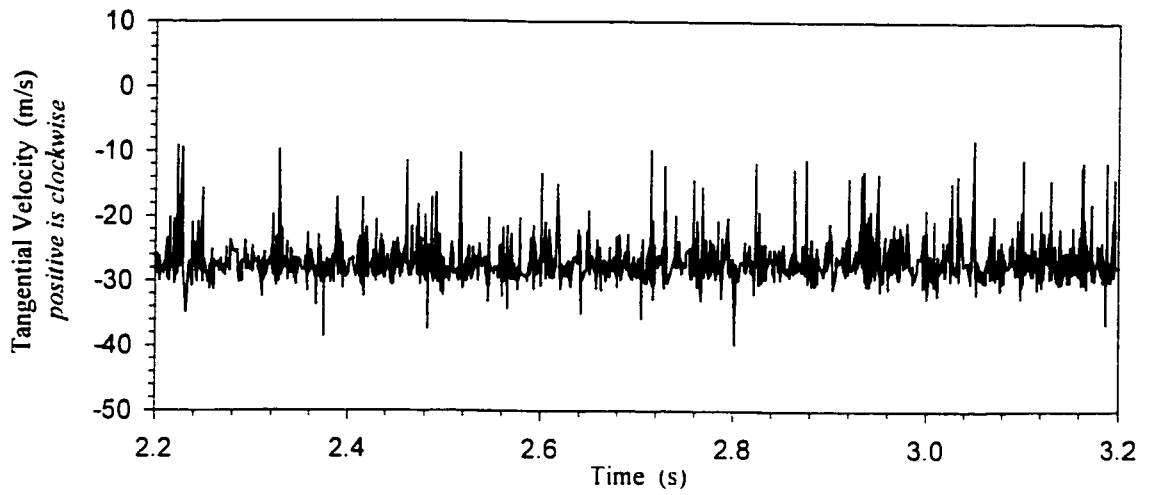
Figure 3.5: Time series of tangential velocity in cyclone inlet at x/a = 0.33 and y/b = 0.4 (with D_{outlet}/D_{barrel} = 0.50; a and b are the width and height of the inlet)
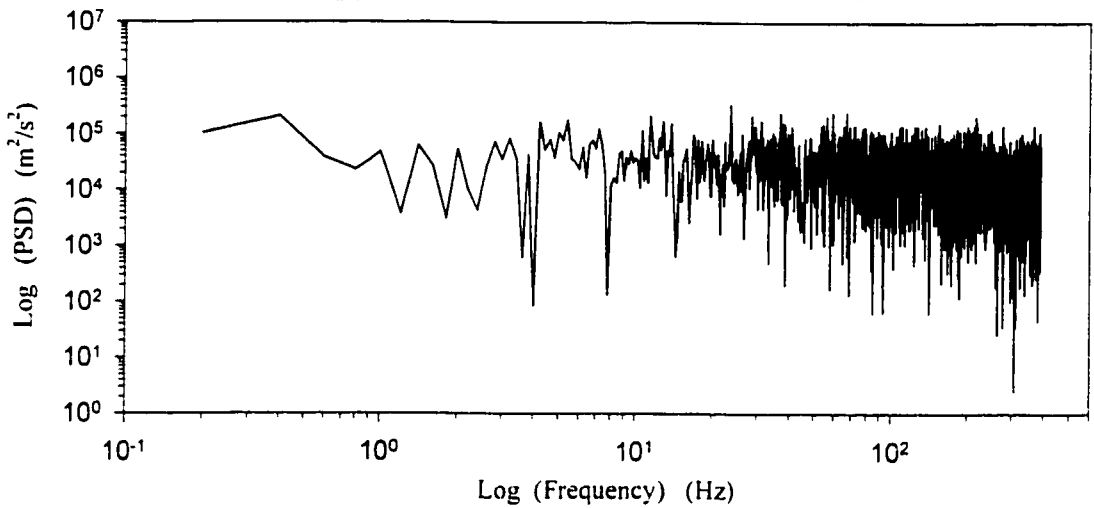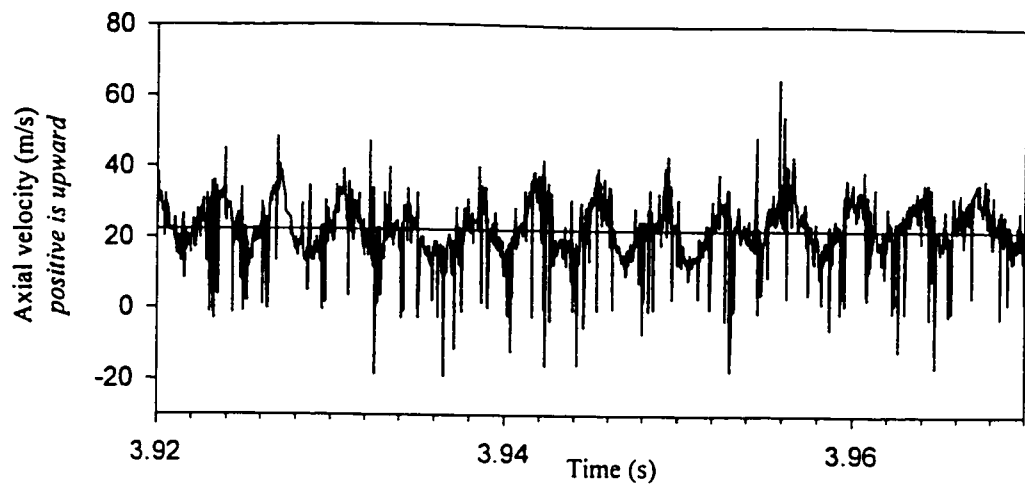

Figure 3.6: Frequency analysis in cyclone inlet at x/a = 0.33 and y/b = 0.4 (with D_{outlet}/D_{barrel} = 0.50: a and b are the width and height of the inlet)
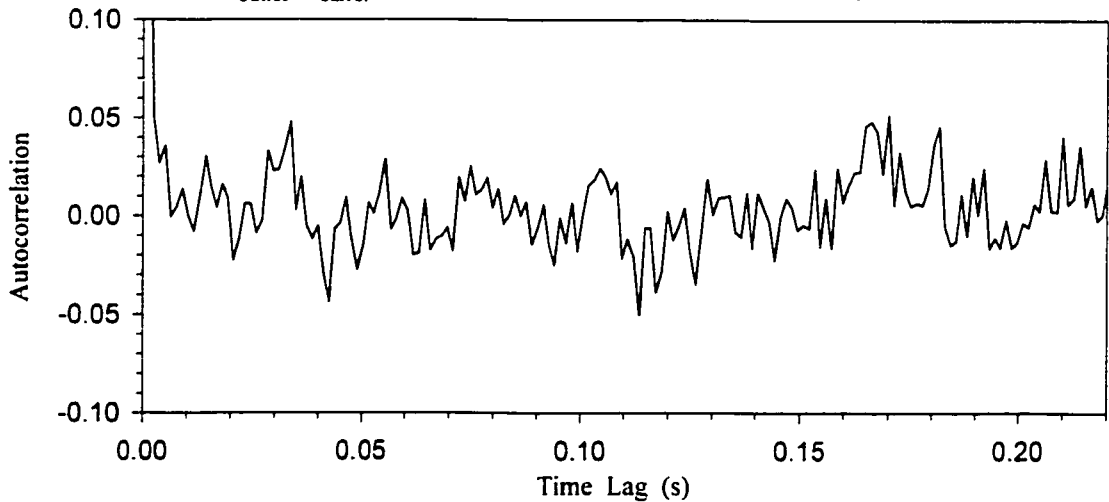
Figure 3.7: Autocorrelation coefficient in cyclone inlet at x/a = 0.33 and y/b = 0.40 (with D_{outlet}/D_{barrel} = 0.50; a and b are the width and height of the inlet)

Figure 3.8 Time series of axial velocity in cyclone outlet at h_{top}= 50 mm
and r = 32.5 mm (with D_{outlet}/D_{barrel} = 0.50)
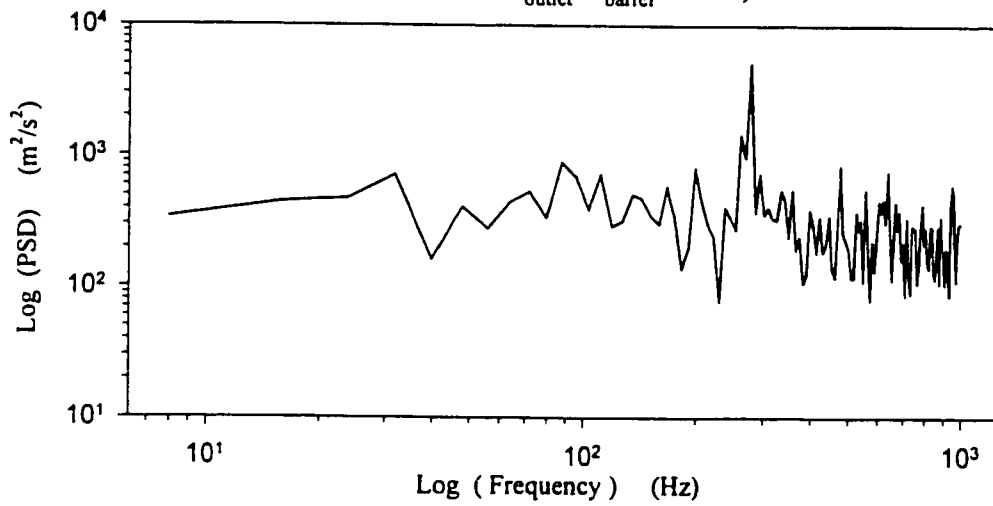
Figure 3.9 Frequency analysis in cyclone outlet at h_{top}= 50 mm
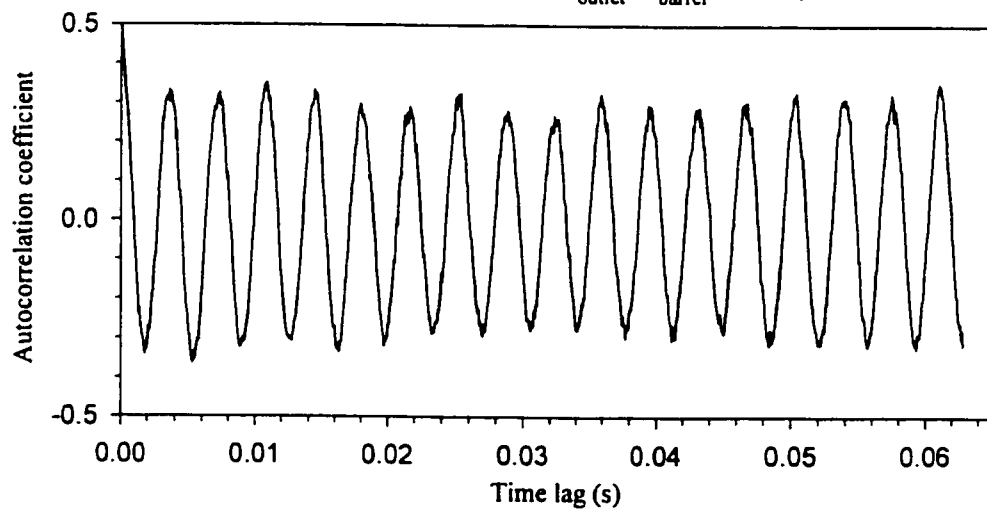and r = 32.5 mm (with D_{outlet}/D_{barrel} = 0.50)

Figure 3.10 Autocorrelation coefficient in cyclone outlet at h_{top}= 50 mm
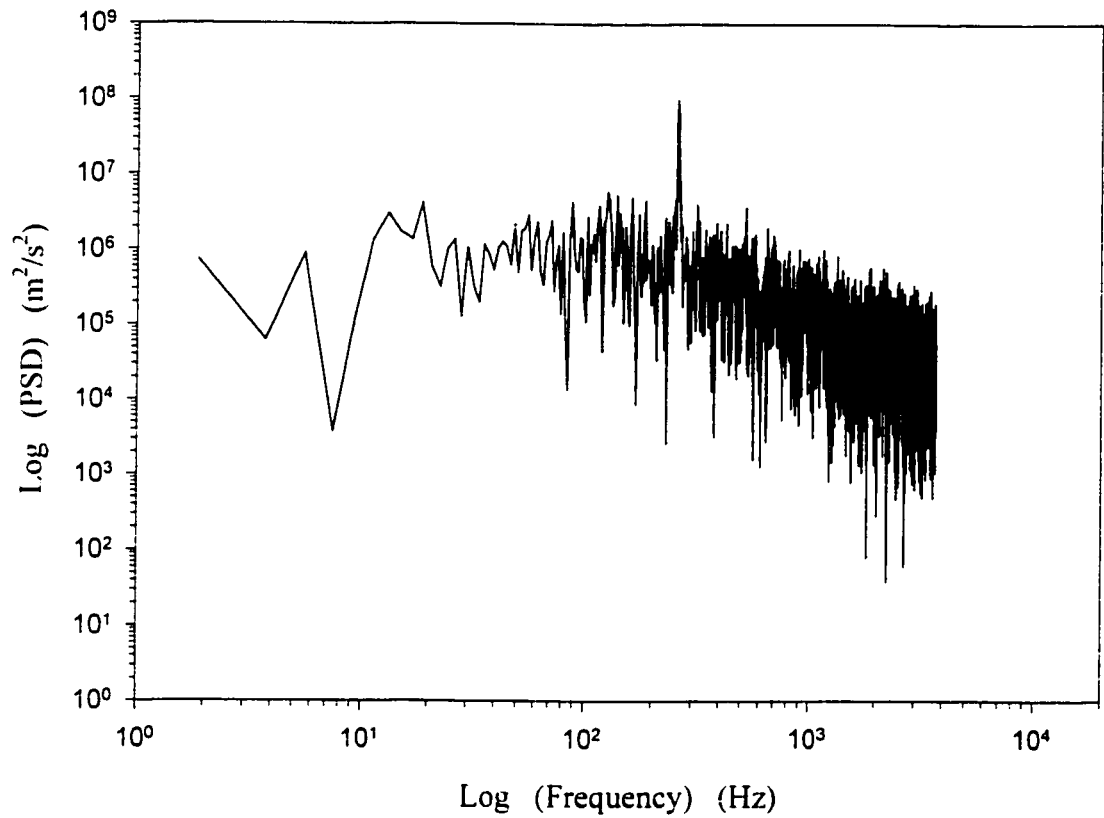and r = 32.5 mm (with D_{outlet}/D_{barrel} = 0.50)

Figure 3.11: Frequency analysis at the top of cyclone outlet at
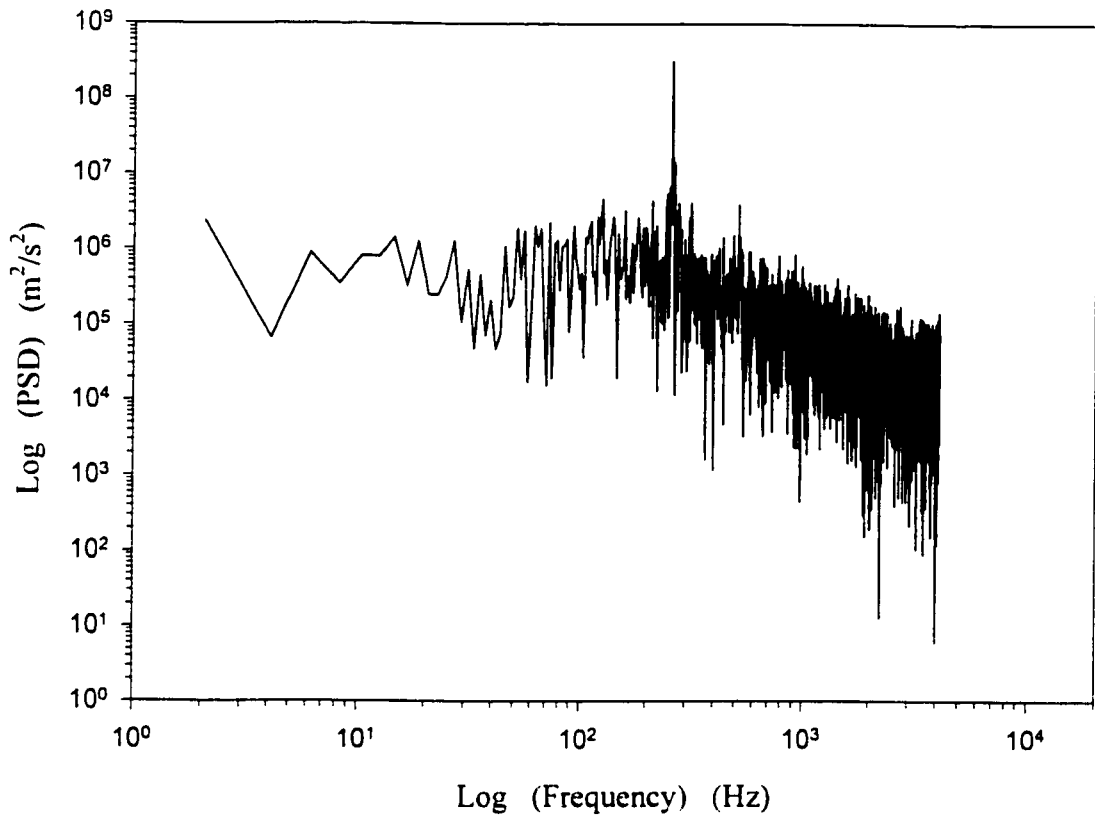$h_{top} = -2$ mm and r = 30 mm (with $D_{outlet}/D_{barrel} = 0.50$)

Figure 3.12: Frequency analysis at the top of cyclone outlet at
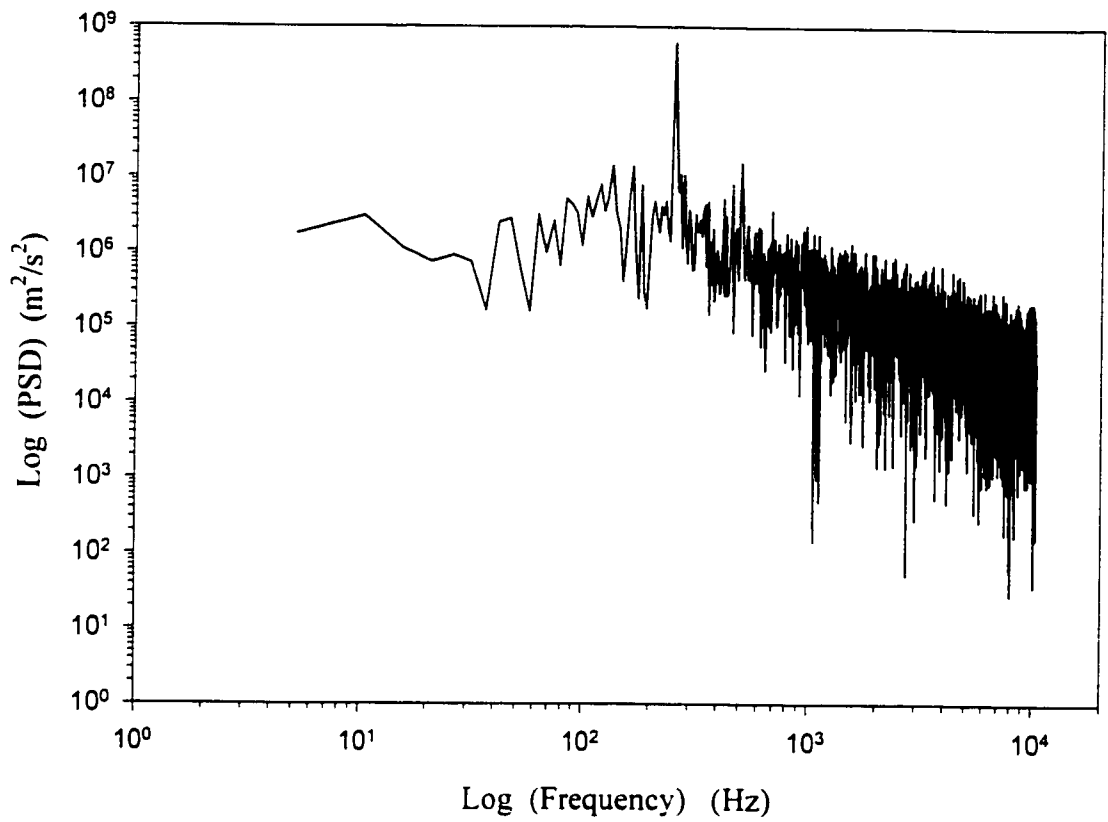h_{top} = - 2 mm and r = 20 mm (with D_{outlet}/D_{barrel} = 0.50)

Figure 3.13: Frequency analysis at the top cyclone outlet at
h_{top} = -2 mm and r = 10 mm (with D_{outlet}/D_{barrel} = 0.50)
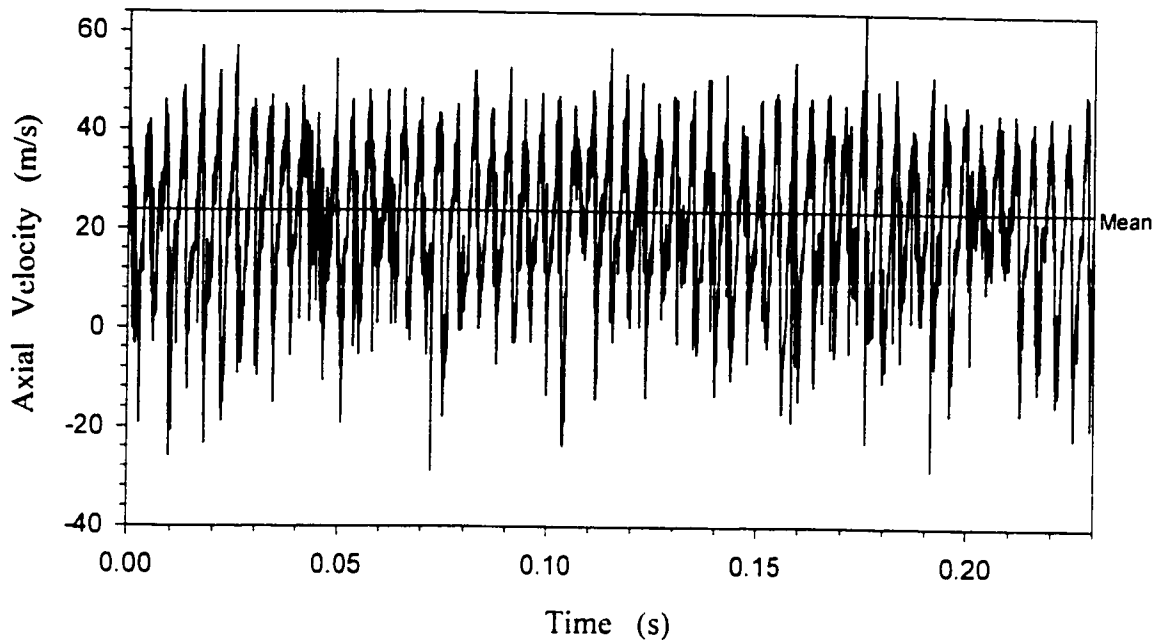
Fig. 3.14: Time series of axial velocity at the top of cyclone outlet at
h_{top} = -13 mm and r = 30 mm (with D_{outlet}/D_{barrel} = 0.50)

Fig. 3.15: Frequency analysis of axial velocity at the top cyclone outlet
at h_{top} = -13 mm and r = 30 mm (with D_{outlet}/D_{barrel} = 0.50)

Figure 3.16: Time series of axial velocity at the top of cyclone outlet at h_{top} = -2 mm and r = 30 mm (with D_{outlet}/D_{barrel} = 0.50)

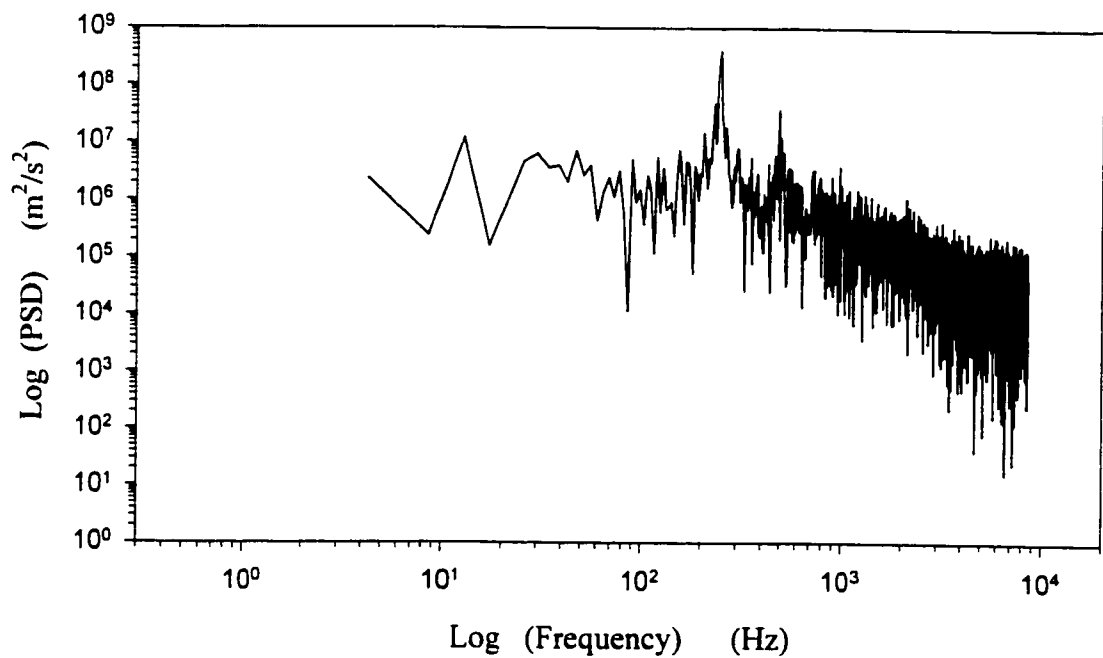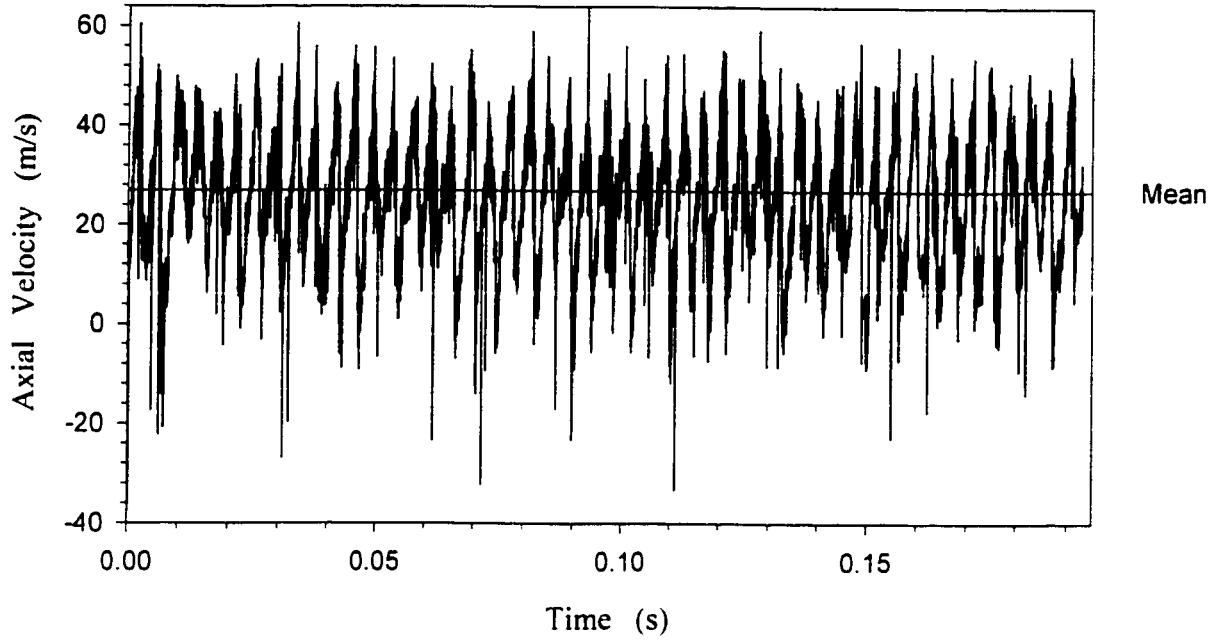Figure 3.17: Frequency analysis of axial velocity at the top of cyclone outlet at h_{top} = -2 mm and r = 30 mm (with D_{outlet}/D_{barrel} = 0.50)

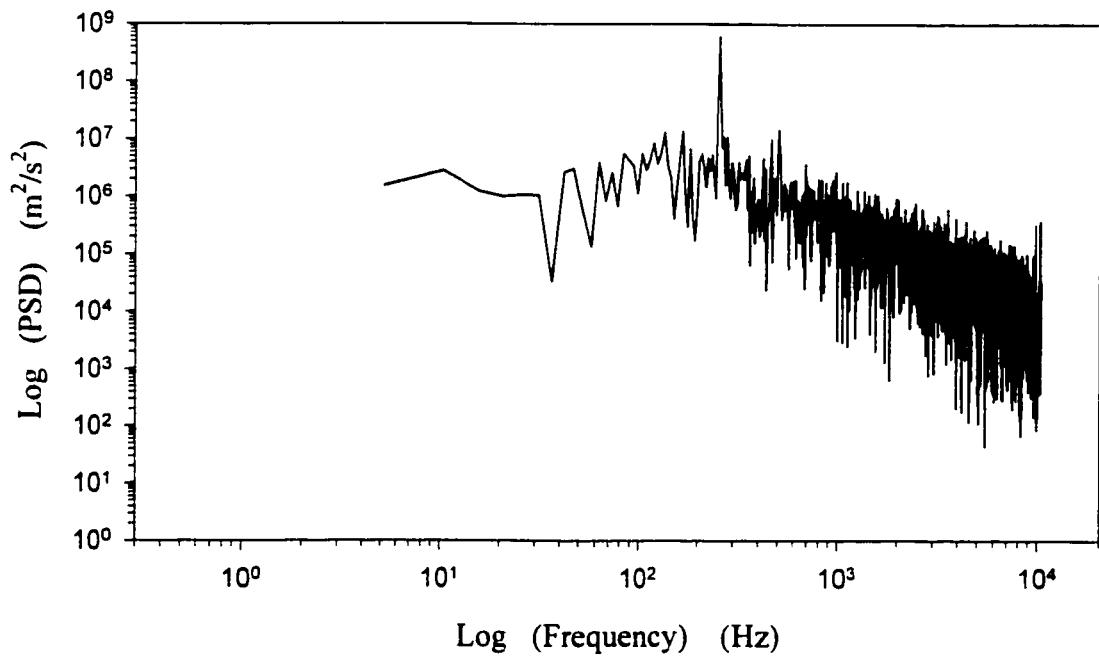Figure 3.18: Time series of axial velocity in cyclone outlet at h_{top} = 40 mm
and r = 30 mm (with D_{outlet}/D_{barrel} = 0.50)

Figure 3.19: Frequency analysis of axial velocity outlet at h_{top} = 40 mm
and r = 30 mm (with D_{outlet}/D_{barrel} = 0.50)

Figure 3.20: Time series of axial velocity in cyclone outlet at h_{top} = 90 mm and r = 30 mm (with D_{outlet}/D_{barrel} = 0.50)

Figure 3.21: Frequency analysis of axial velocity in cyclone outlet at h_{top} = 90 mm and r = 30 mm (with D_{outlet}/D_{barrel} = 0.50)
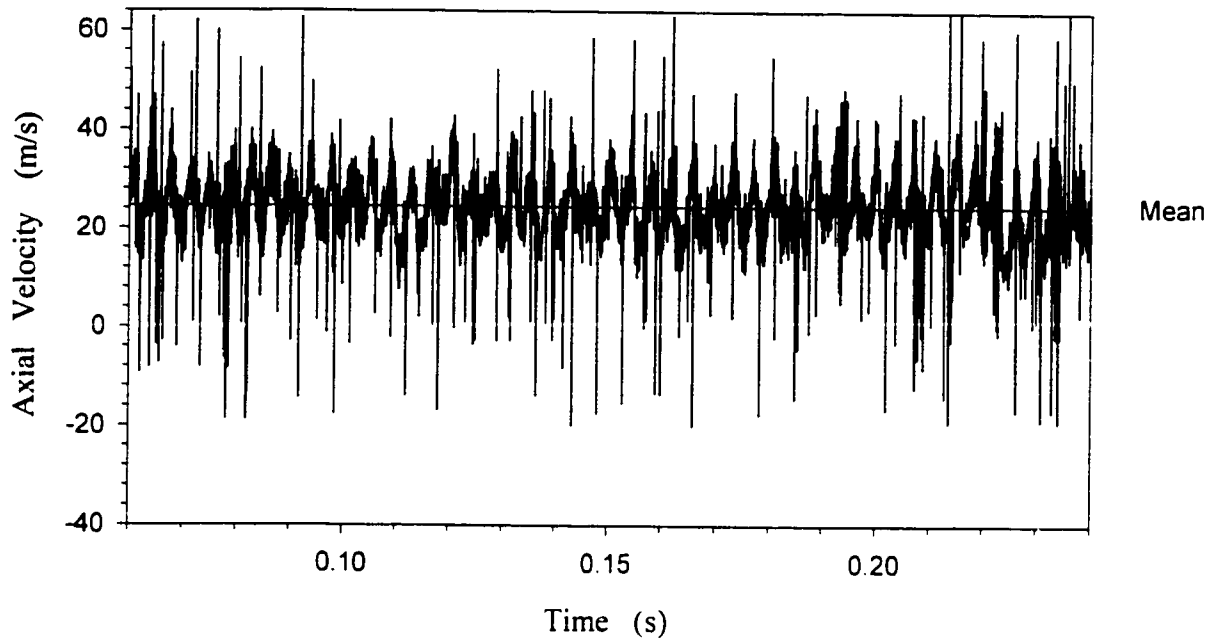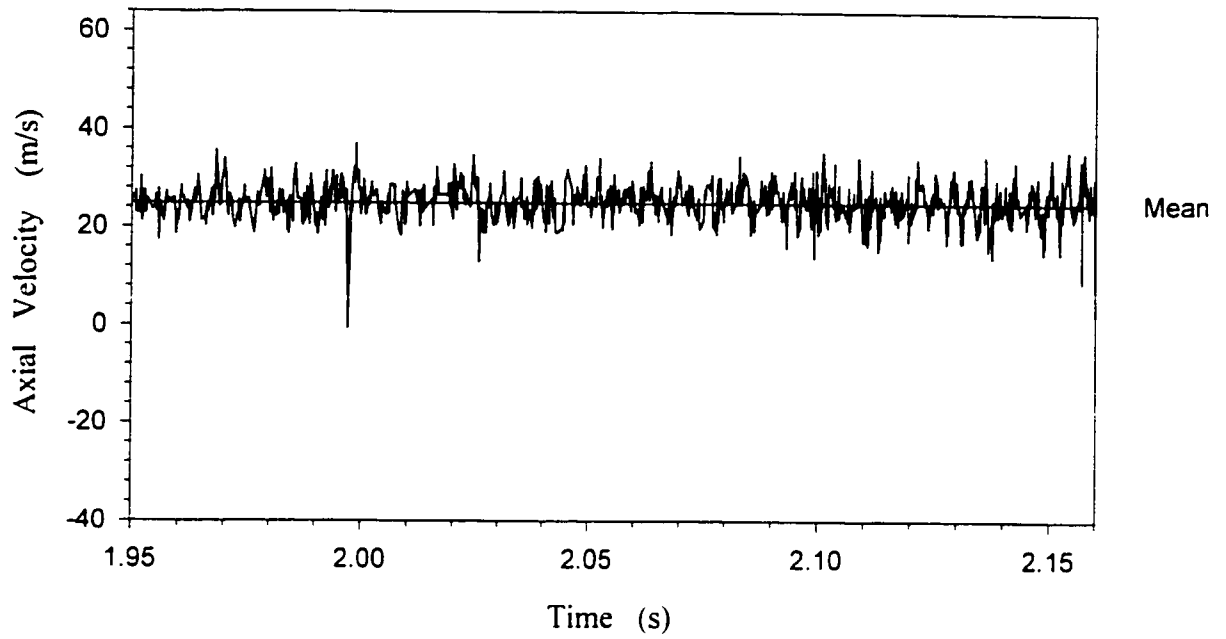
Figure 3.22: Time series of axial velocity in cyclone outlet at
h_{top} = 110 mm and r = 30 mm (with D_{outlet}/D_{barrel} = 0.50)
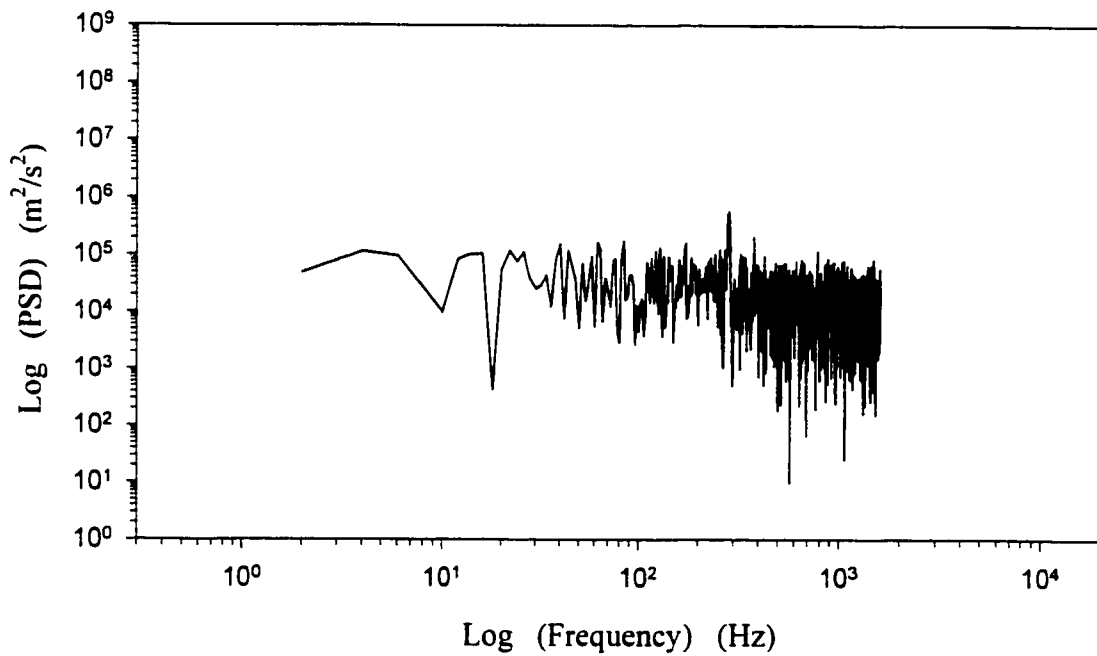
Figure 3.23: Frequency analysis of axial velocity in cyclone outlet at
h_{top} = 110 mm and r = 30 mm (with D_{outlet}/D_{barrel} = 0.50)
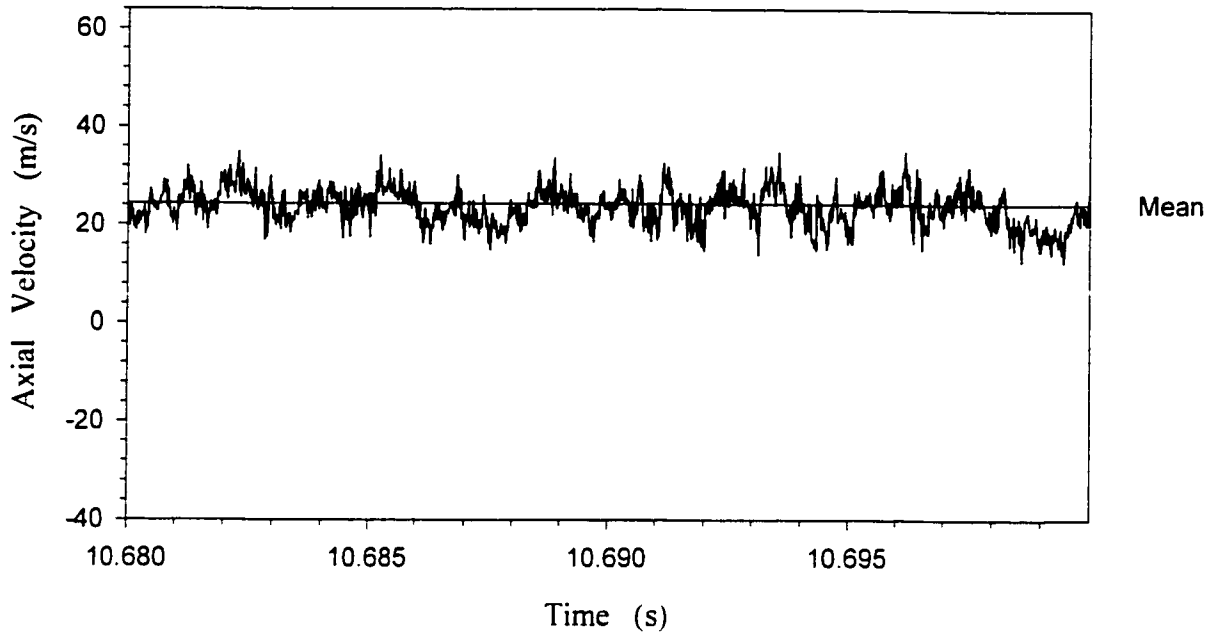
Figure 3.24: Time series of axial velocity in cyclone outlet at h_{top} = 135 mm and r = 30 mm (with D_{outlet}/D_{barrel} = 0.50)
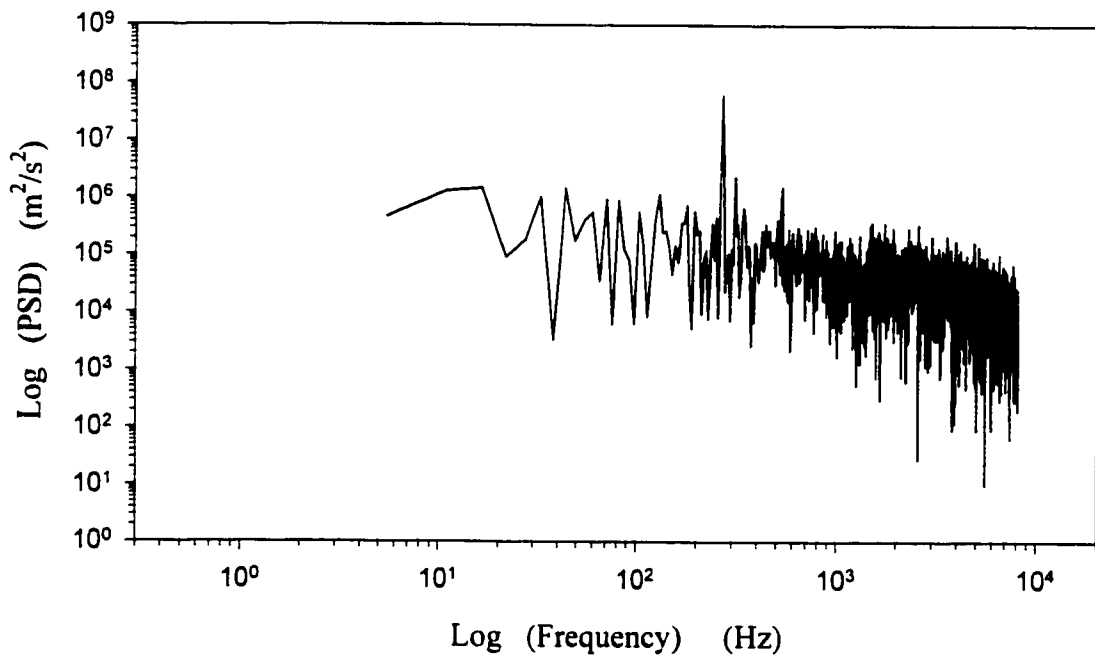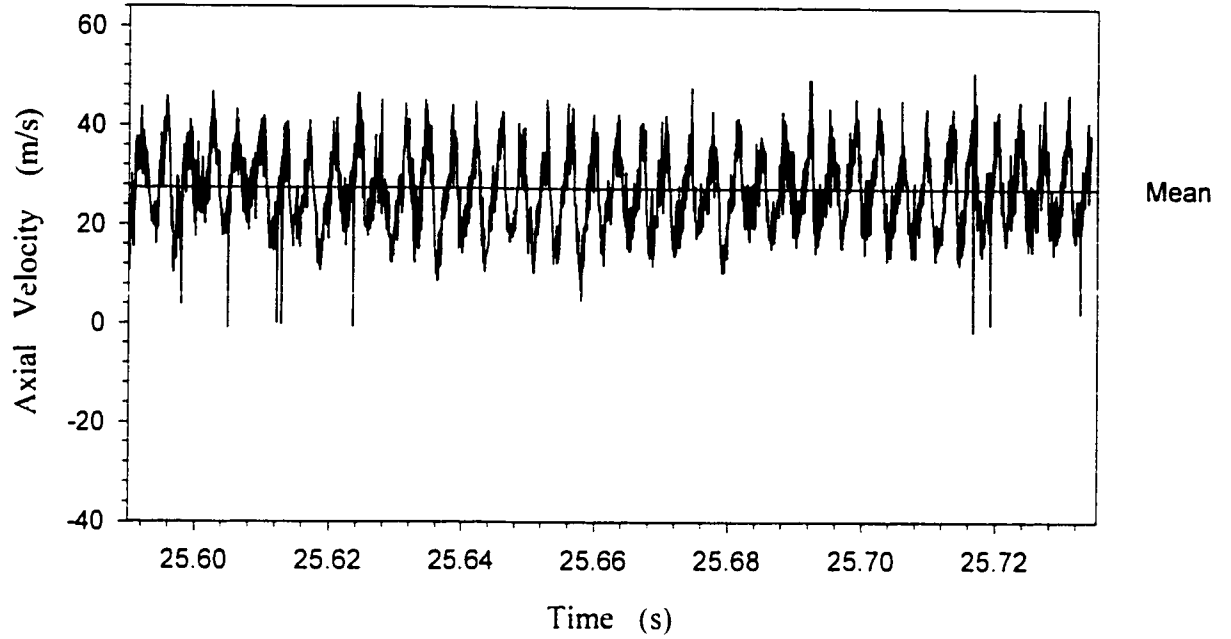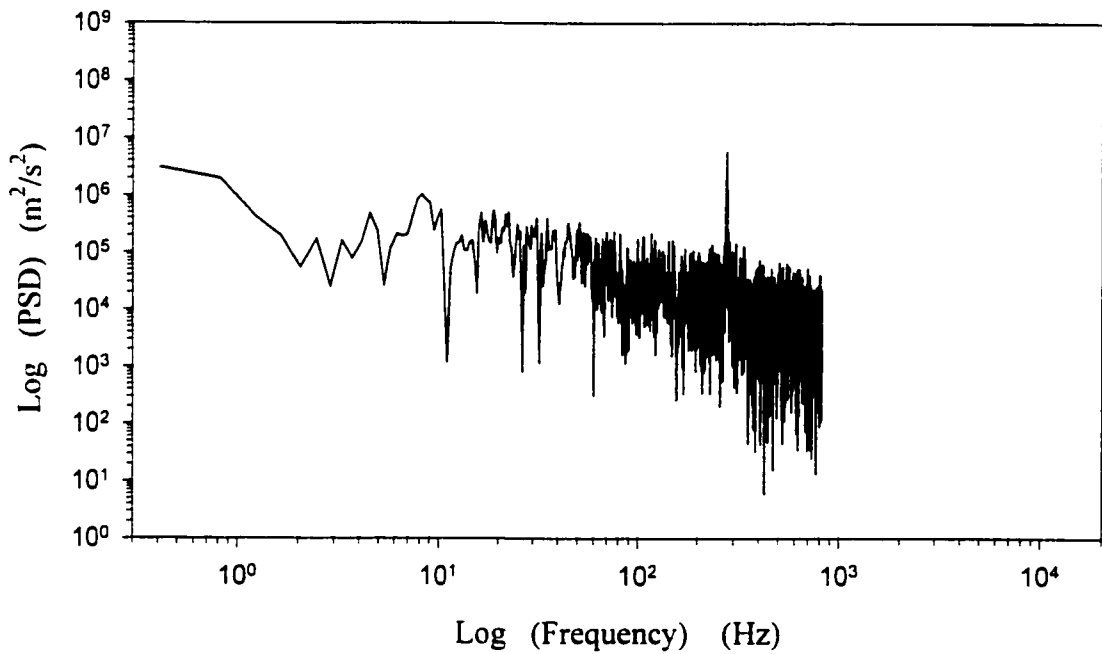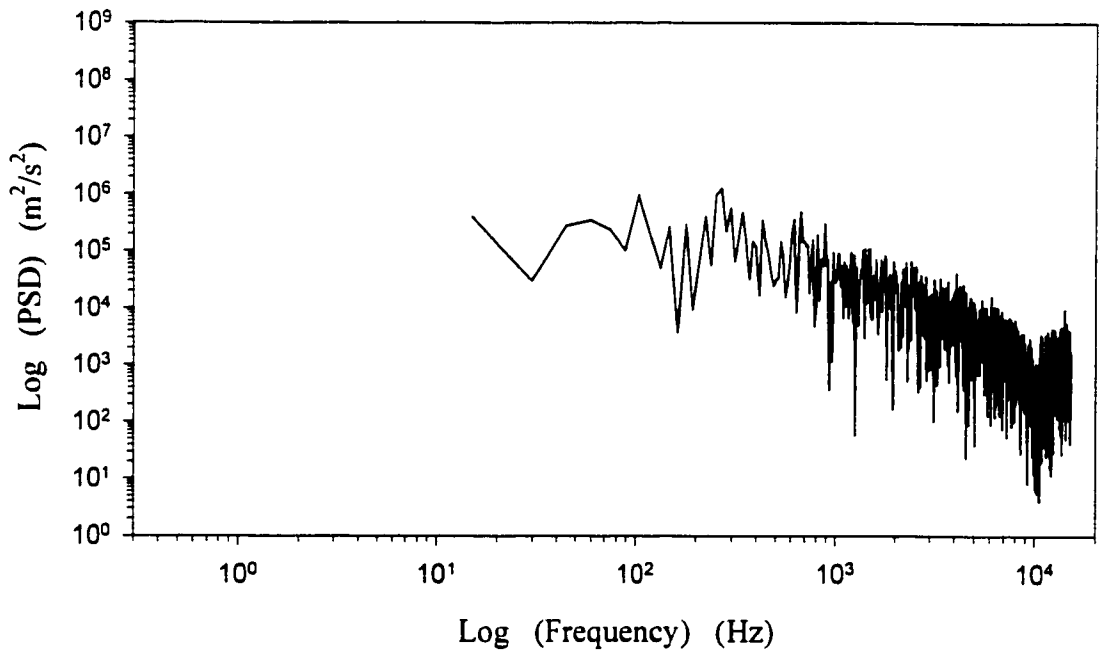

Figure 3.25: Frequency analysis of axial velocity in cyclone outlet at h_{top} = 135 mm and r = 30 mm (with D_{outlet}/D_{barrel} = 0.50)
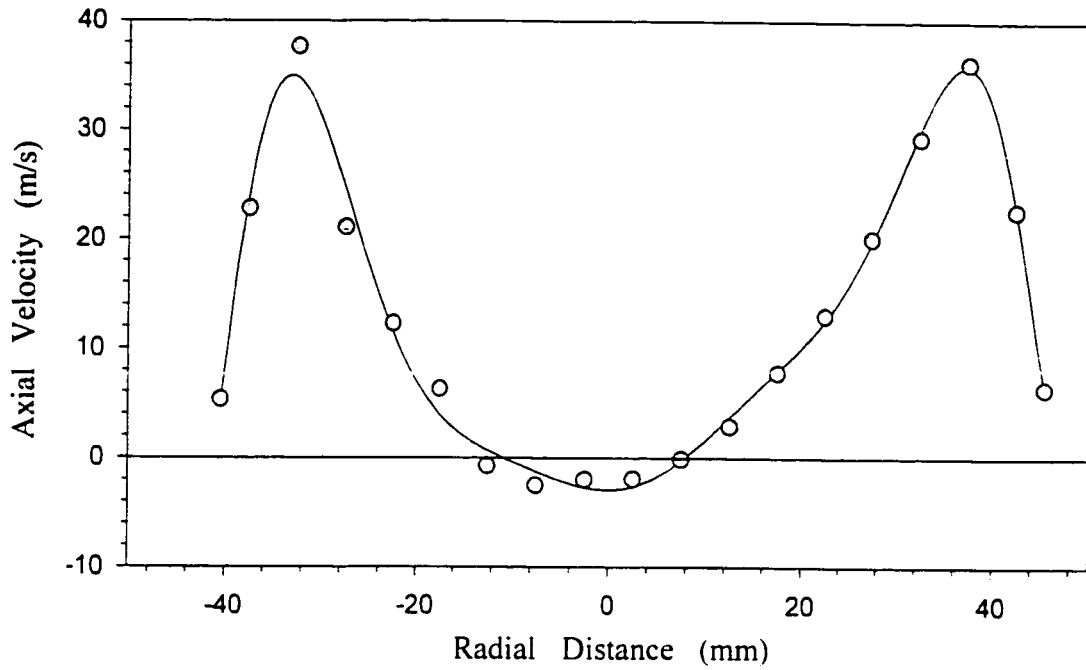
Figure 3.26: Axial velocity profile 13 mm above the top of cyclone outlet tube (with $D_{outlet}/D_{barrel} = 0.50$)
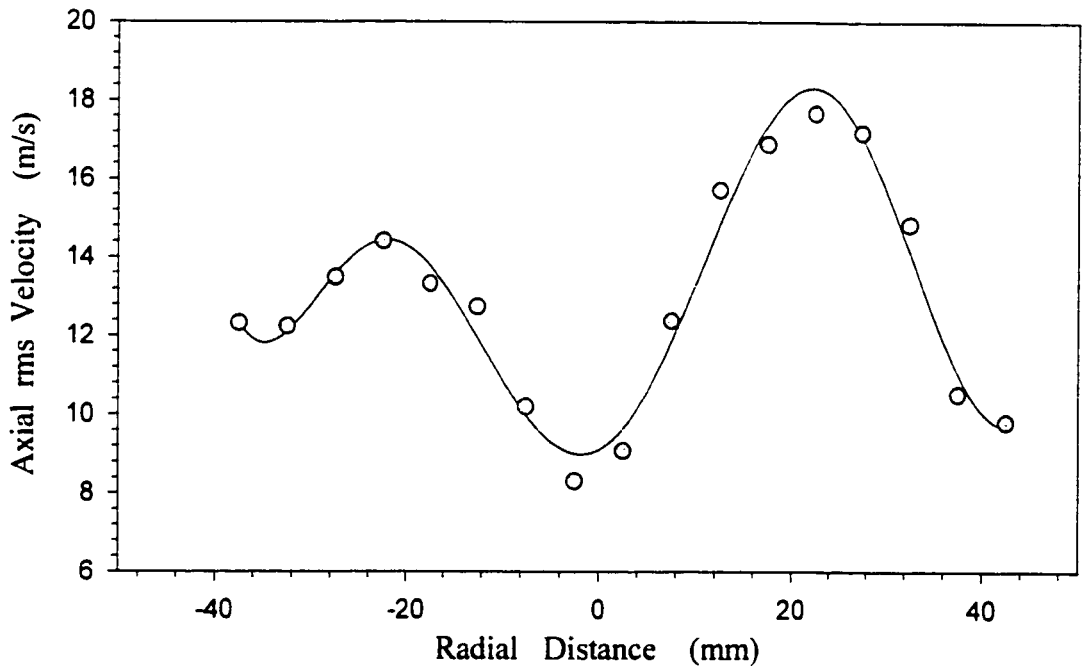
Figure 3.27: The axial rms velocity profile 13mm above the top of cyclone outlet tube (with $D_{outlet}/D_{barrel} = 0.50$)
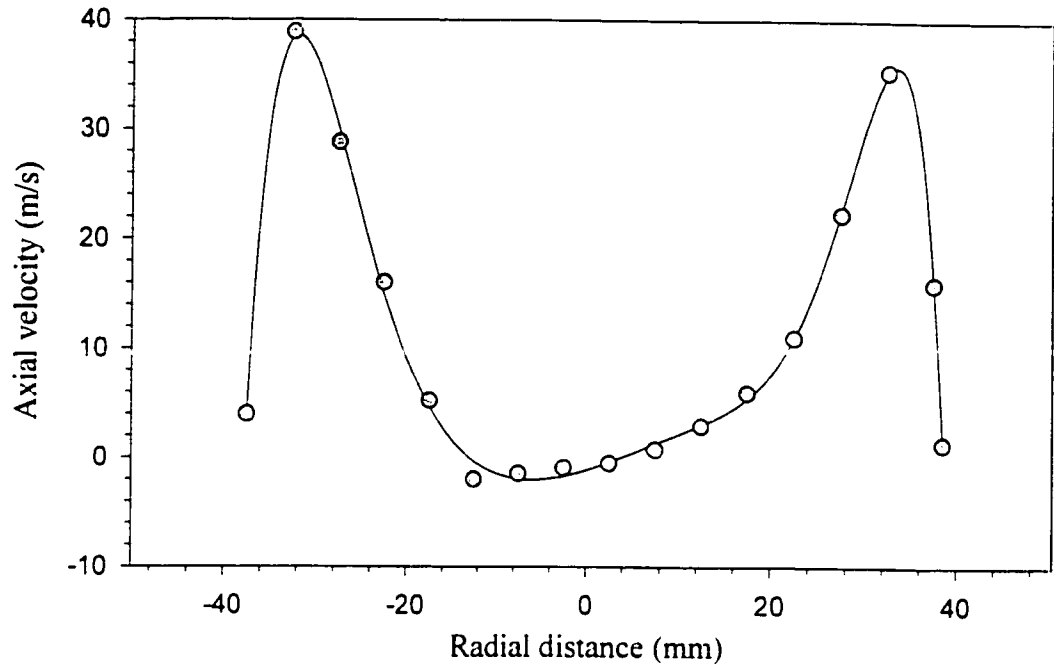
Figure 3.28: Axial velocity profile 2mm above the top of cyclone outlet tube (with $D_{outlet}/D_{barrel}=0.50$)

Figure 3.29: The axial rms velocity 2mm above the top of cyclone outlet tube (with $D_{outlet}/D_{barrel}=0.50$)

Figure 3.30: Axial velocity profile 90 mm from the top of cyclone outlet tube (with $D_{outlet}/D_{barrel} = 0.50$)

Figure 3.31: Axial rms velocity profile 90 mm from the top of cyclone outlet tube (with $D_{outlet}/D_{barrel} = 0.50$)

Figure 3.32: Axial velocity profile in the gas outlet tube 135mm from the top of cyclone outlet tube (with D$_{outlet}$/D$_{barrel}$ = 0.50)
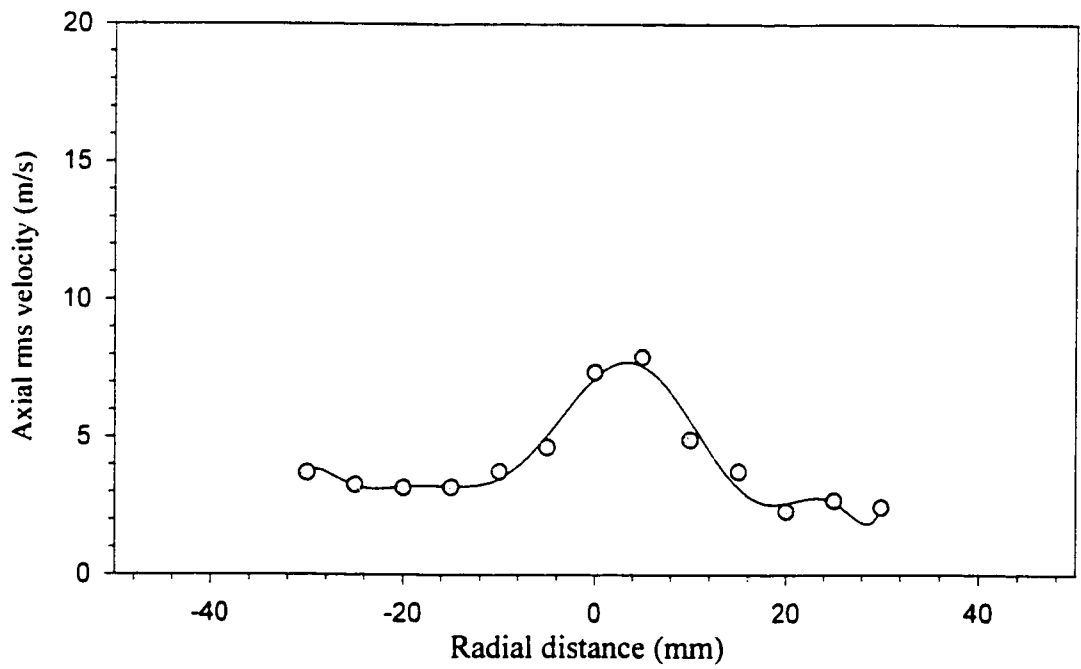
Figure 3.33: Axial rms velocity in the gas outlet tube 135mm from the top of cyclone outlet tube (with D$_{outlet}$/D$_{barrel}$ = 0.50)
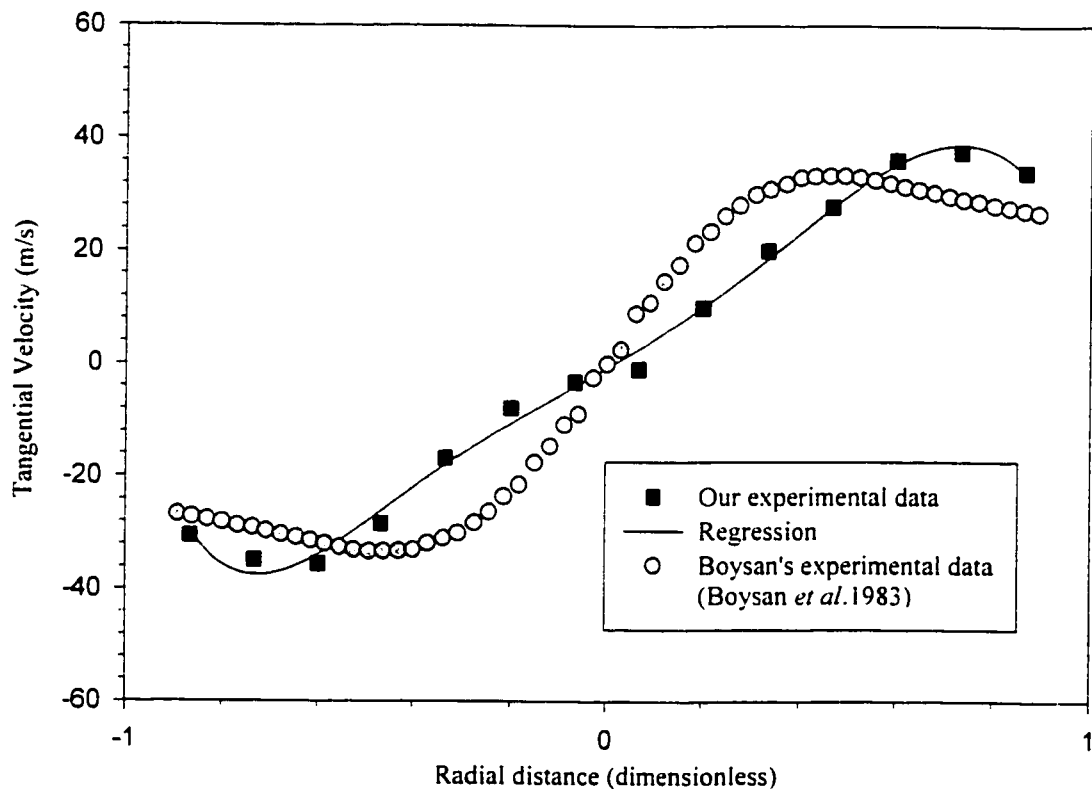
Figure 3.34: Tangential velocity profile in the barrel at
h_{top} = 415 mm (15 mm from cyclone roof)
(with D_{outlet}/D_{barrel} = 0.50)
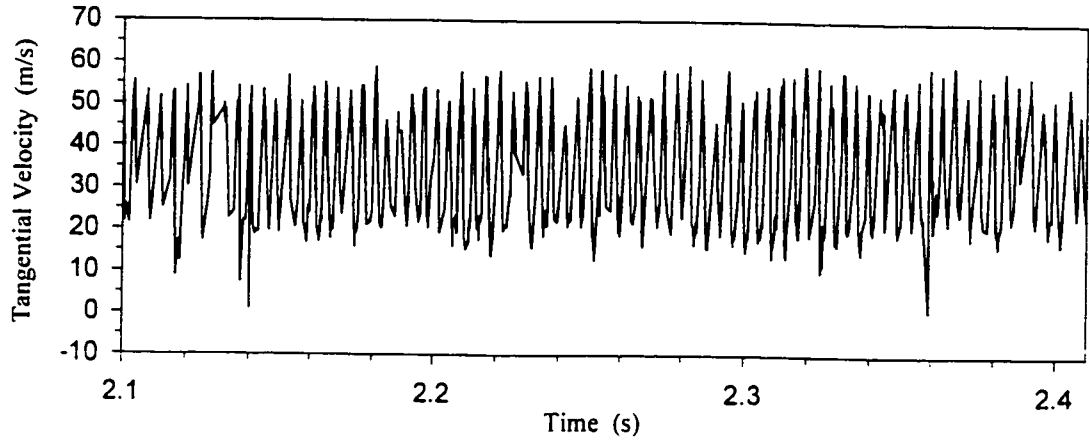
Figure 3.35: Time series of tangential velocity at the top of cyclone outlet at h_{top} = -1 mm and r = 27.5 mm (with D_{outlet}/D_{barrel} = 0.50)
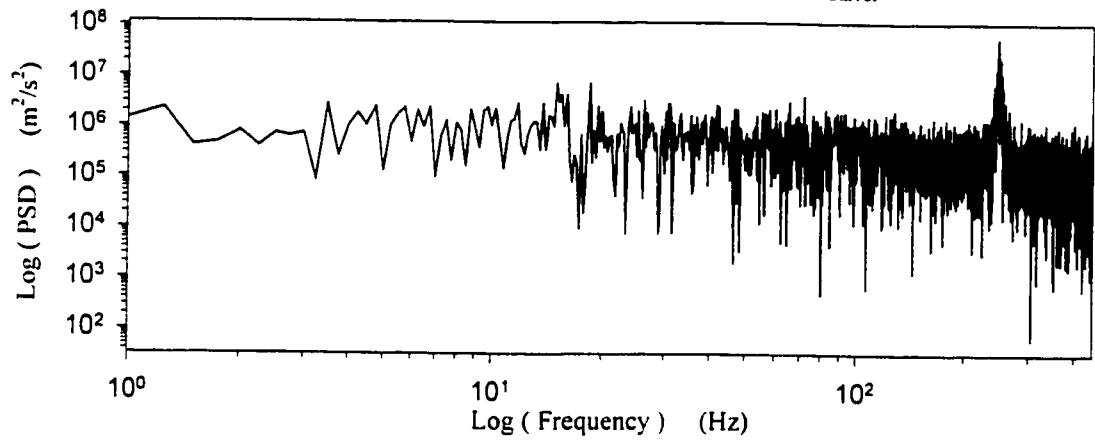
Figure 3.36: Frequency analysis at the top of cyclone outlet at h_{top} = -1 mm and r = 27.5 mm (with D_{outlet}/D_{barrel} = 0.50)
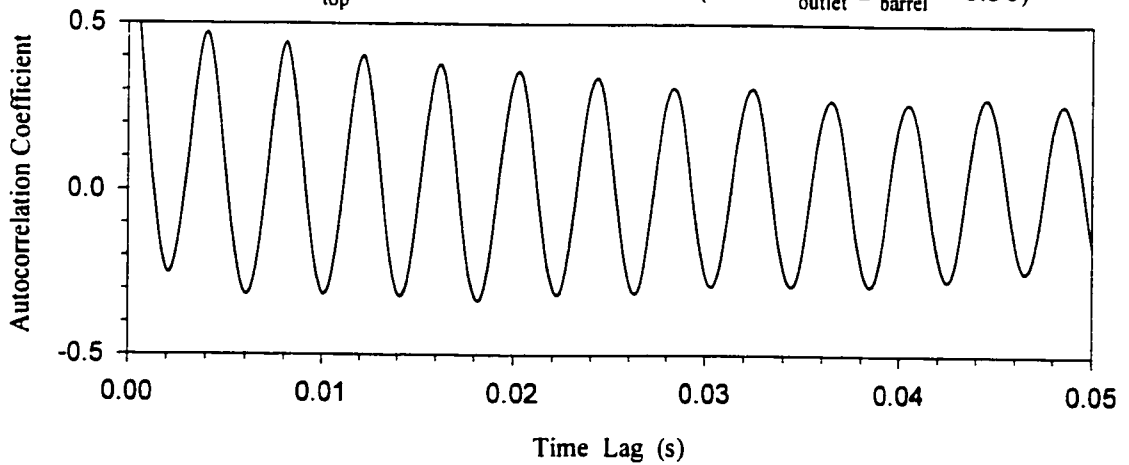
Figure 3.37: Autocorrelation coefficient at the top of cyclone outlet at h_{top} = -1 mm and r = 27.5 mm (with D_{outlet}/D_{barrel} = 0.50)
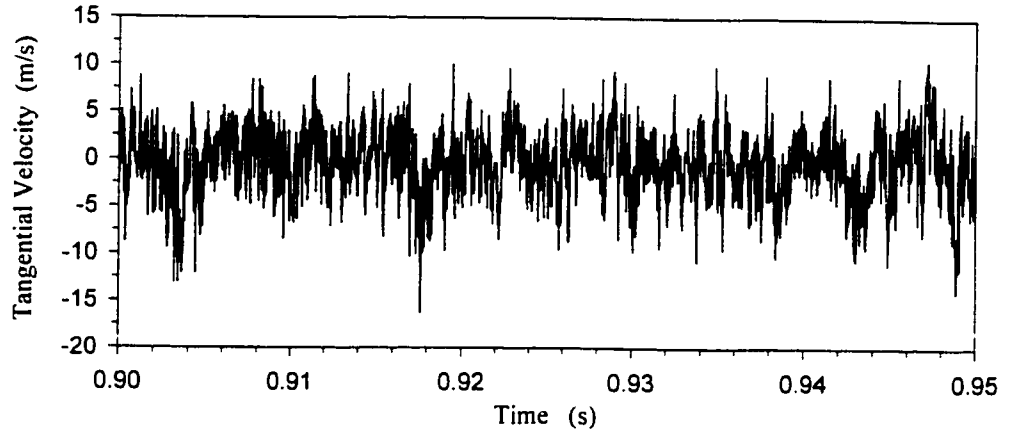
Figure 3.38: Time series of tangential velocity in cyclone barrel at $h_{top} = 415$ mm and $r = 20$ mm (with $D_{outlet}/D_{barrel} = 0.50$)
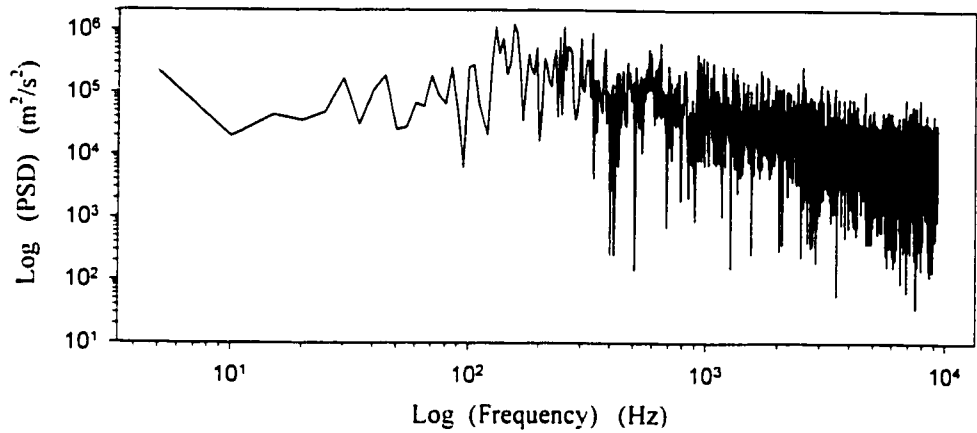
Figure 3.39: Frequency analysis in cyclone barrel at $h_{top} = 415$ mm and $r = 20$ mm (with $D_{outlet}/D_{barrel}=0.50$)
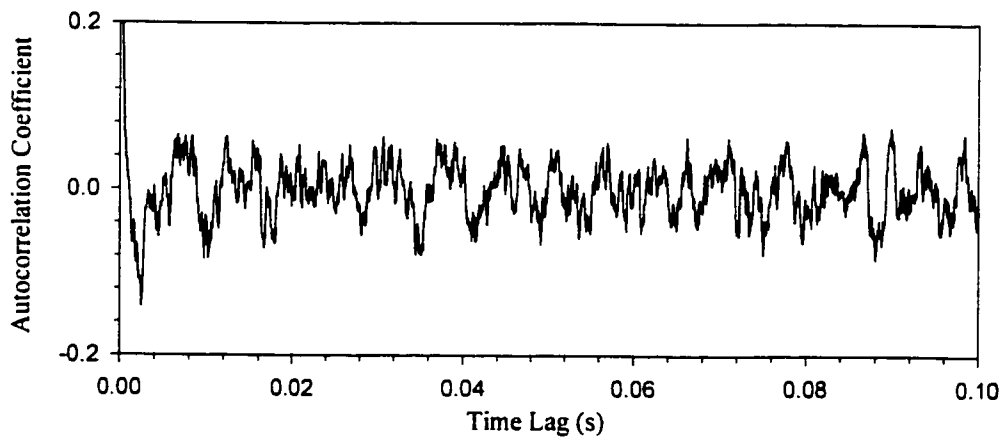
Figure 3.40: Autocorrelation coefficient in cyclone barrel at $h_{top} = 415$ mm and $r = 20$ mm (with $D_{outlet}/D_{barrel}=0.50$)
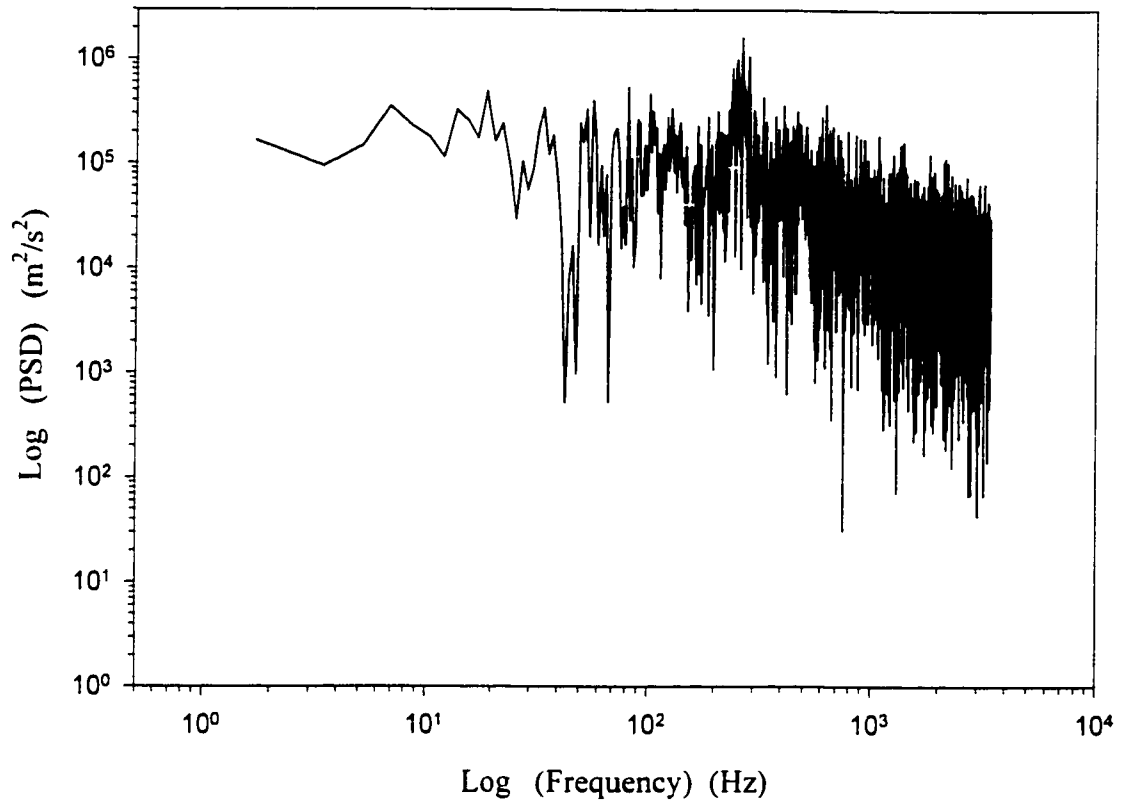
Figure 3.41: Frequency analysis in cyclone barrel at h_{top} = 415 mm
(150 mm from the cyclone roof) and r = 40 mm (with
D_{outlet}/D_{barrel} = 0.63)
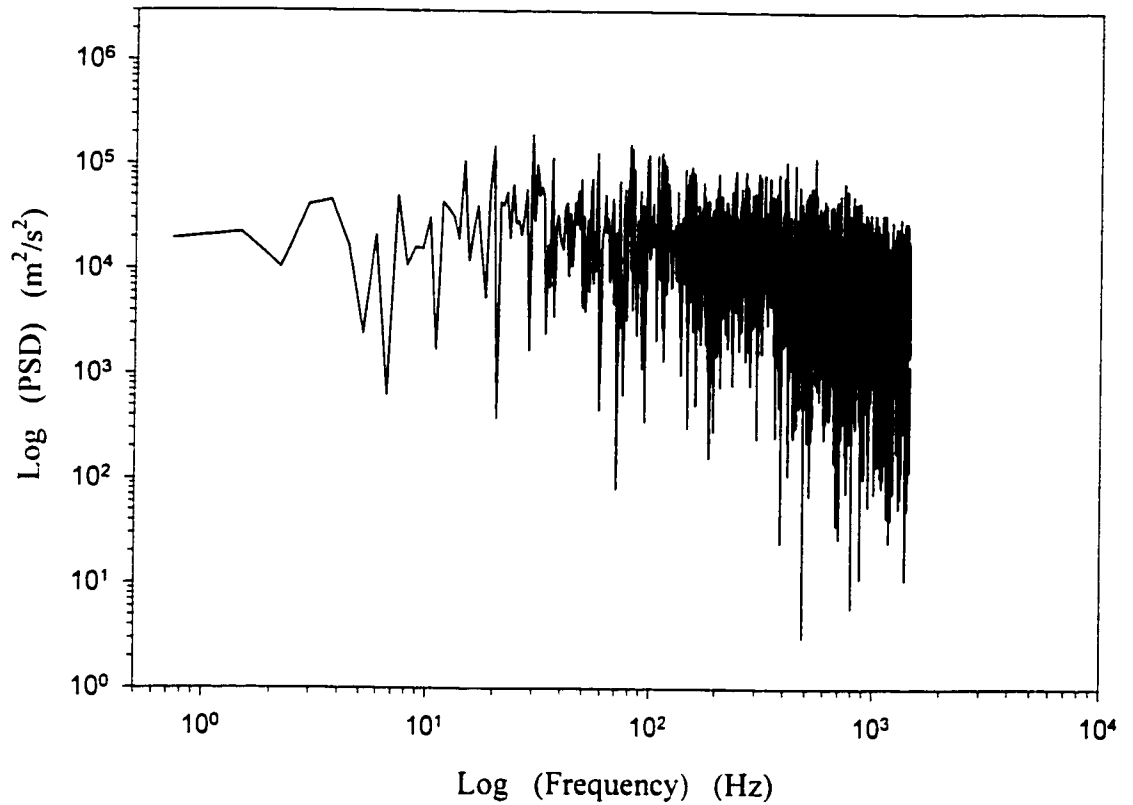
Figure 3.42: Frequency analysis in cyclone barrel at h_{top} = 380 mm (115 mm from cyclone roof) and r = 40 mm (with D_{outlet}/D_{barrel} = 0.33)
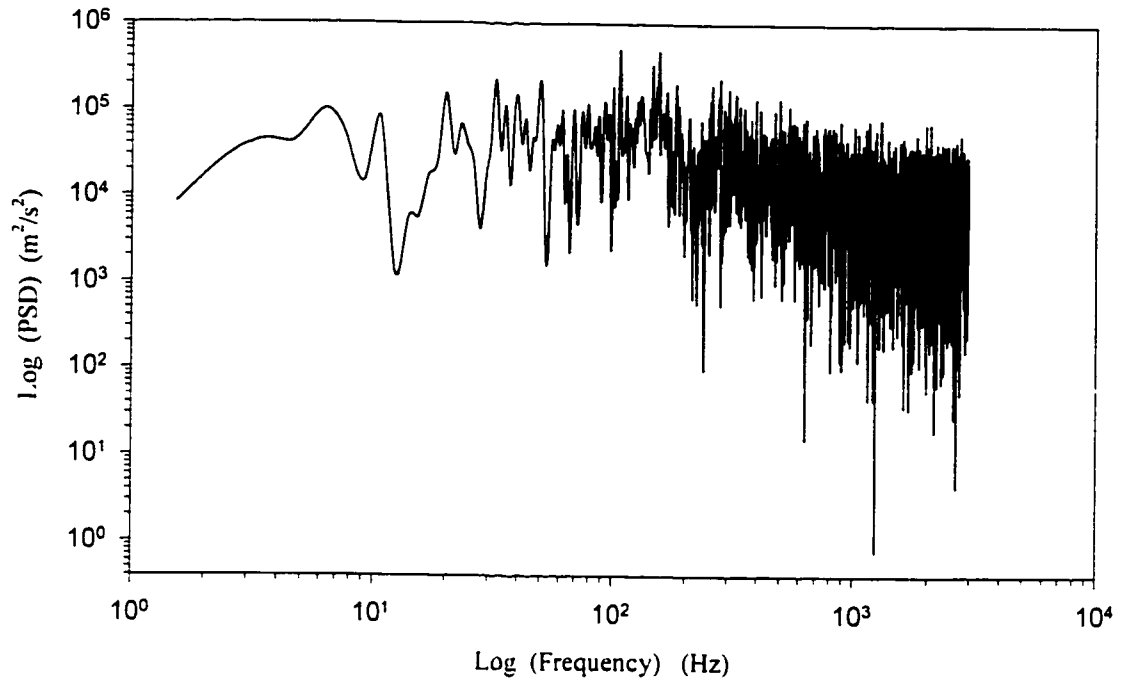
Figure 3.43: Frequency analysis in cyclone cone at h_{top} = 770 mm
and r = 25 mm (with D_{outlet}/D_{barrel} = 0.50)
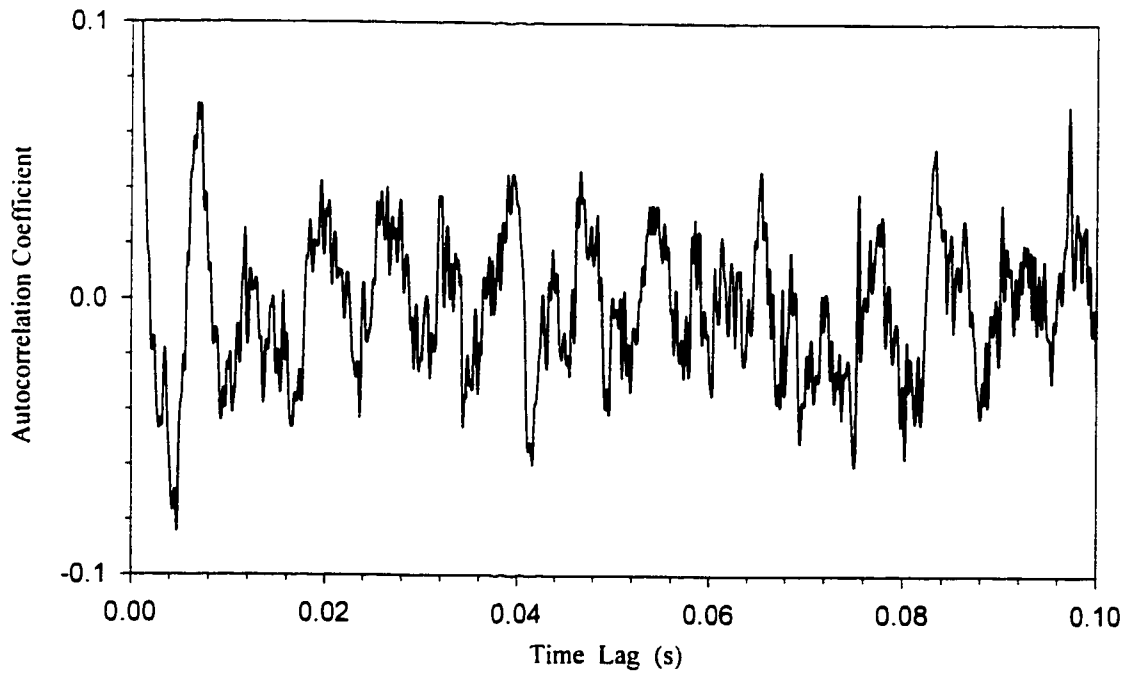
Figure 3.44: Autocorrelation coefficient in cyclone cone at
h_{top} = 770 mm and r = 25 mm (with D_{outlet}/D_{barrel} = 0.50)
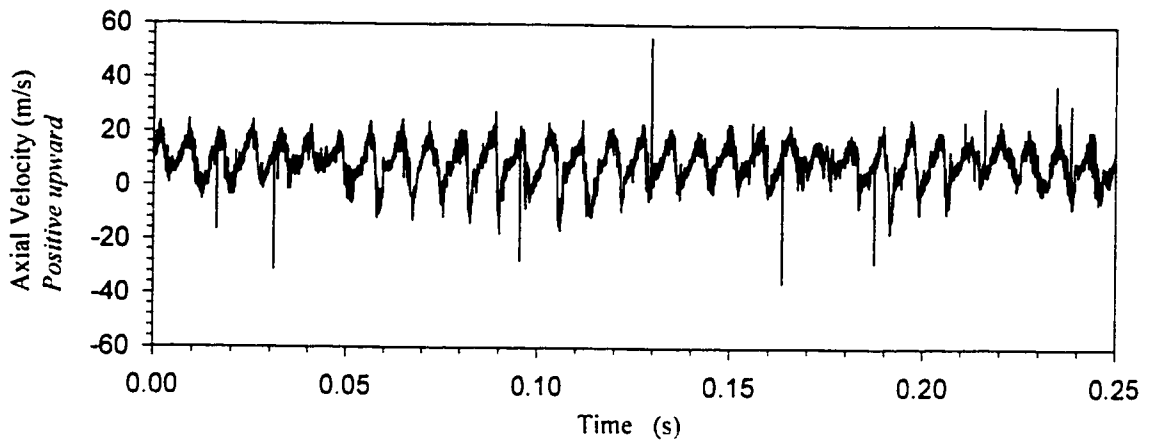
Figure 3.45: Time series of axial velocity in cyclone outlet at h_{top} = 50 mm and r = 20 mm, at 50% motor load (with D_{outlet}/D_{barrel} = 0.50)
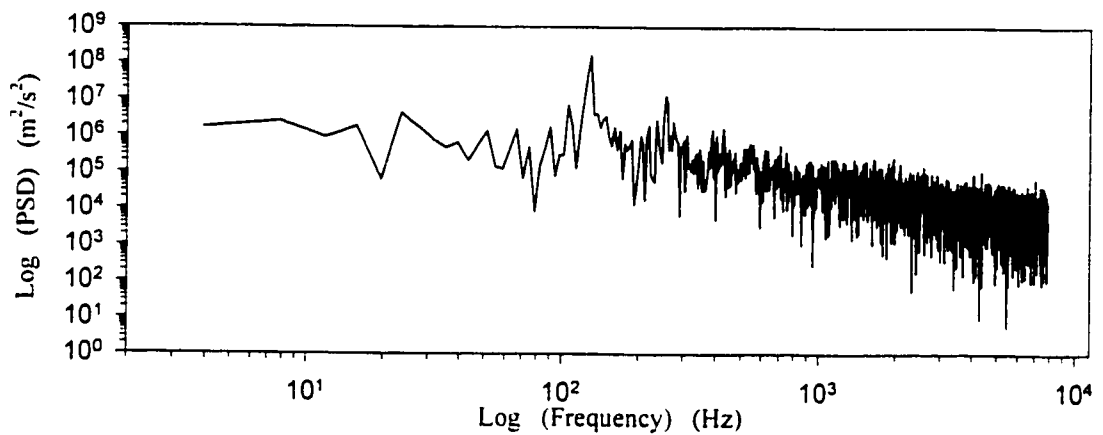
Figure 3.46: Frequency analysis in cyclone outlet at h_{top} = 50 mm and r = 20 mm, at 50% motor load (with D_{outlet}/D_{barrel} = 0.50)
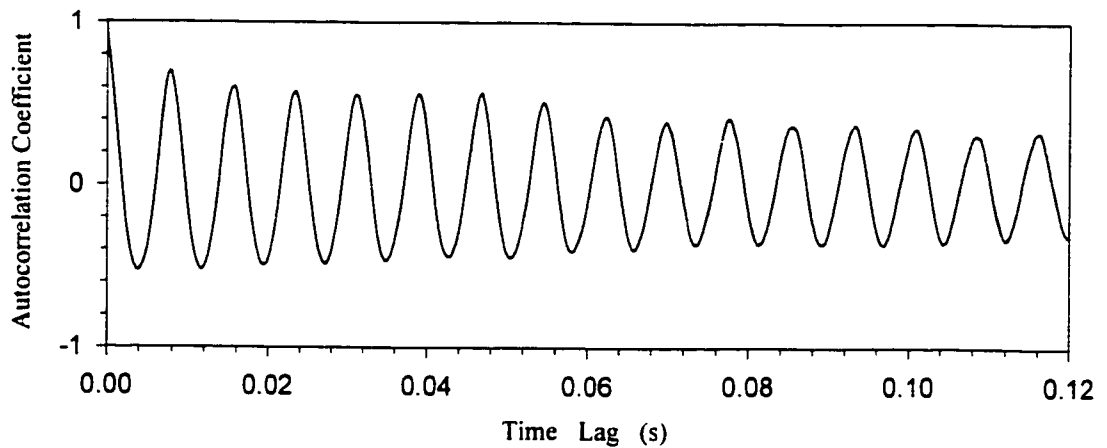
Figure 3.47: Autocorrelation coefficient in cyclone outlet at h_{top} = 50 mm and r = 20 mm, at 50% motor load (with D_{outlet}/D_{barrel} = 0.50)
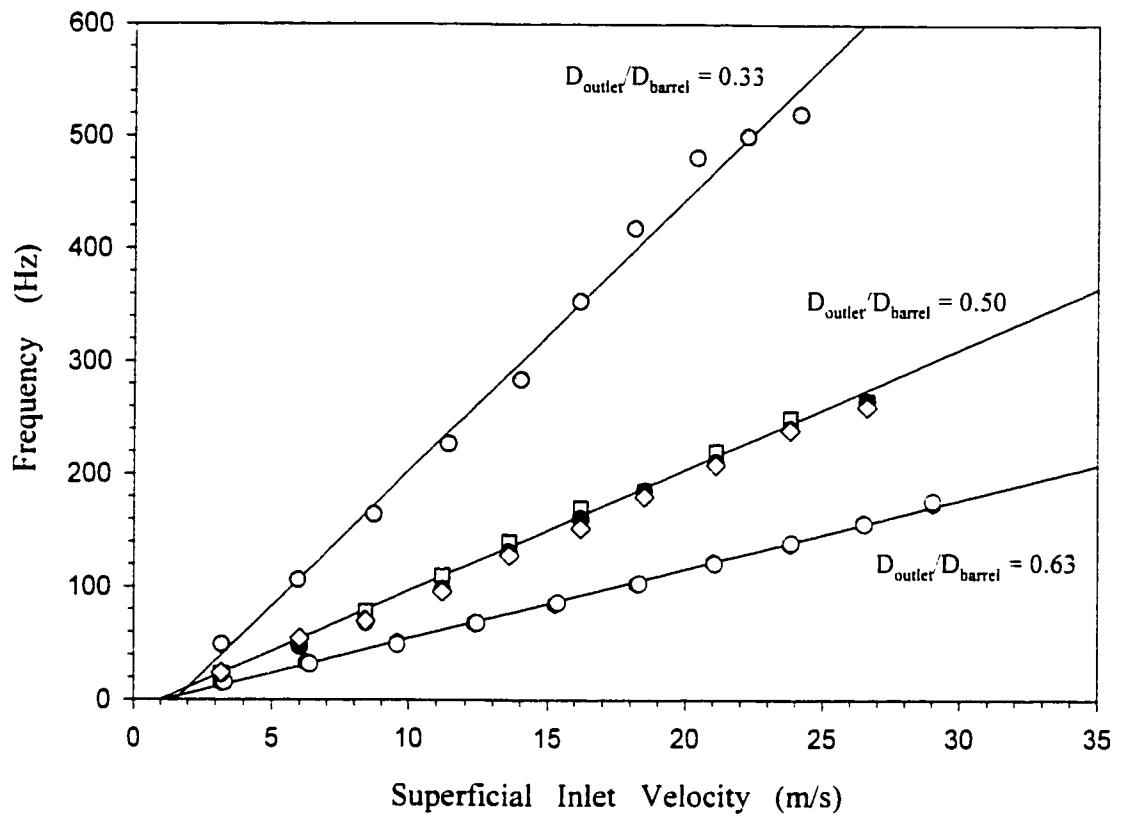
Figure 3.48: Oscillation frequency in the gas outlet tube
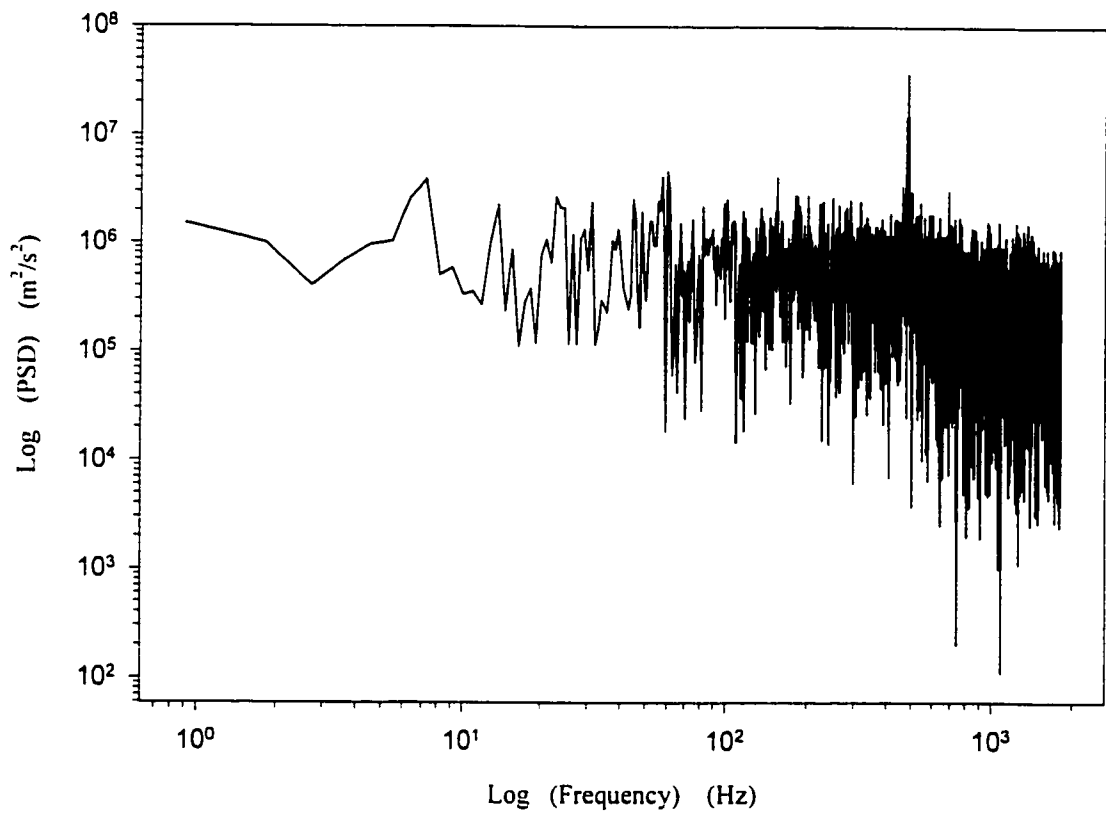
Figure 3.49: Frequency analysis just outside of gas outlet tube at $h_{top} = -1$ mm and $r = 20$ mm (with $D_{outlet}/D_{barrel} = 0.33$)
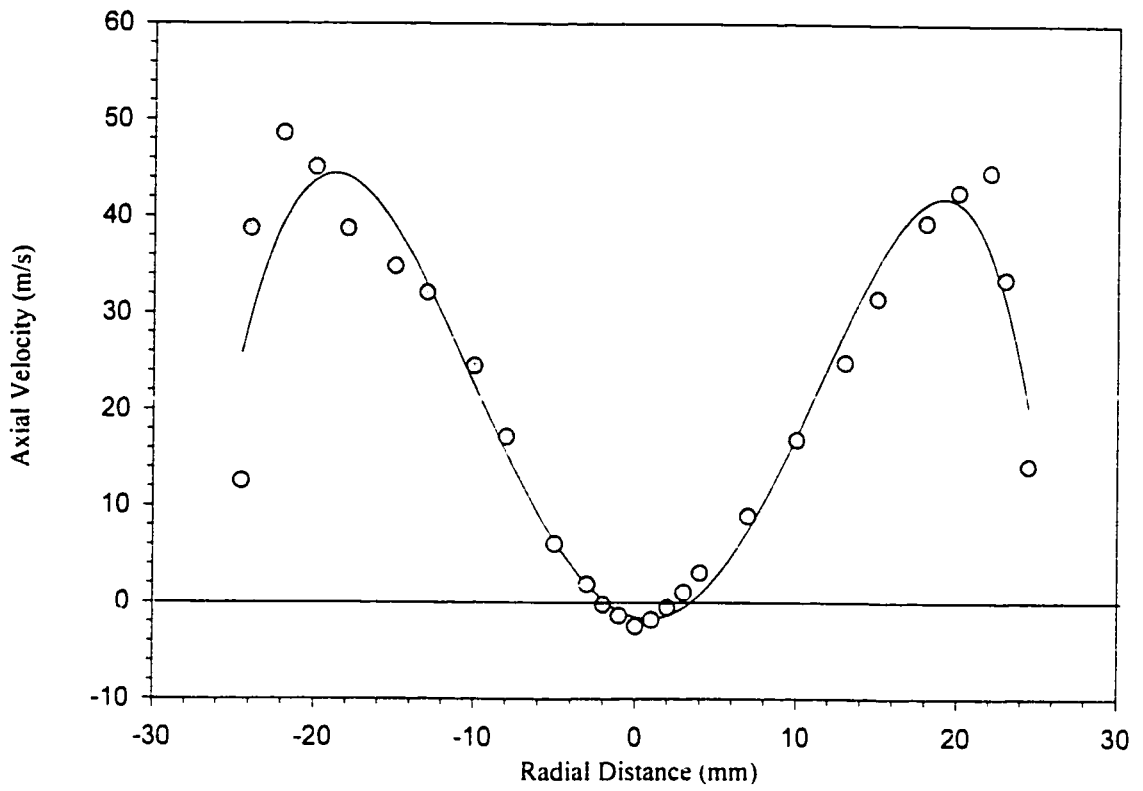
Figure 3.50: Axial velocity profile 2 mm above the top of cyclone
gas outlet tube (with D_{oultet}/D_{barrel} = 0.33)
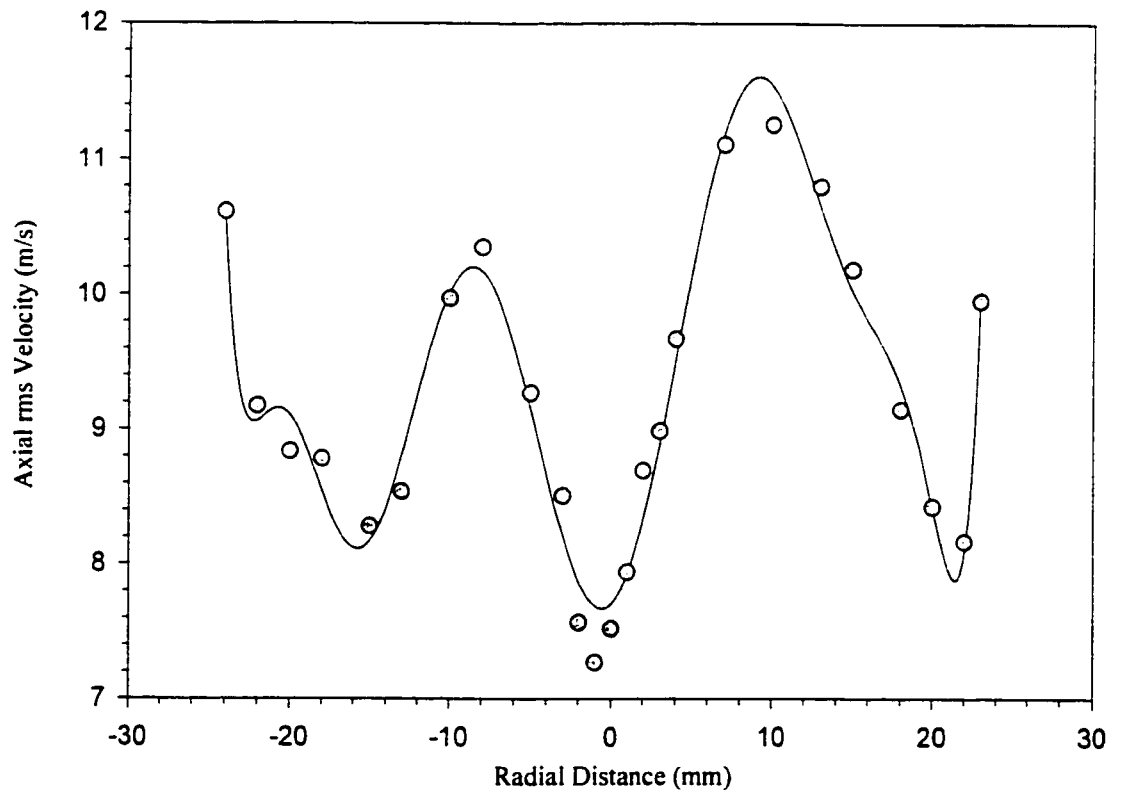
Figure 3.51: Axial rms velocity profile 2 mm above the top of cyclone
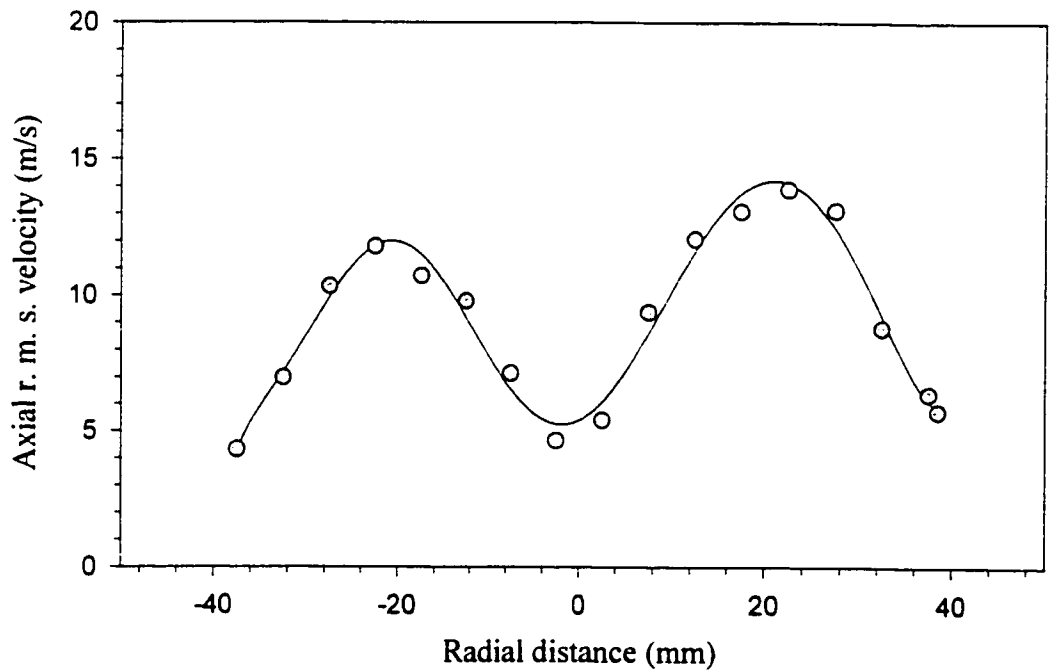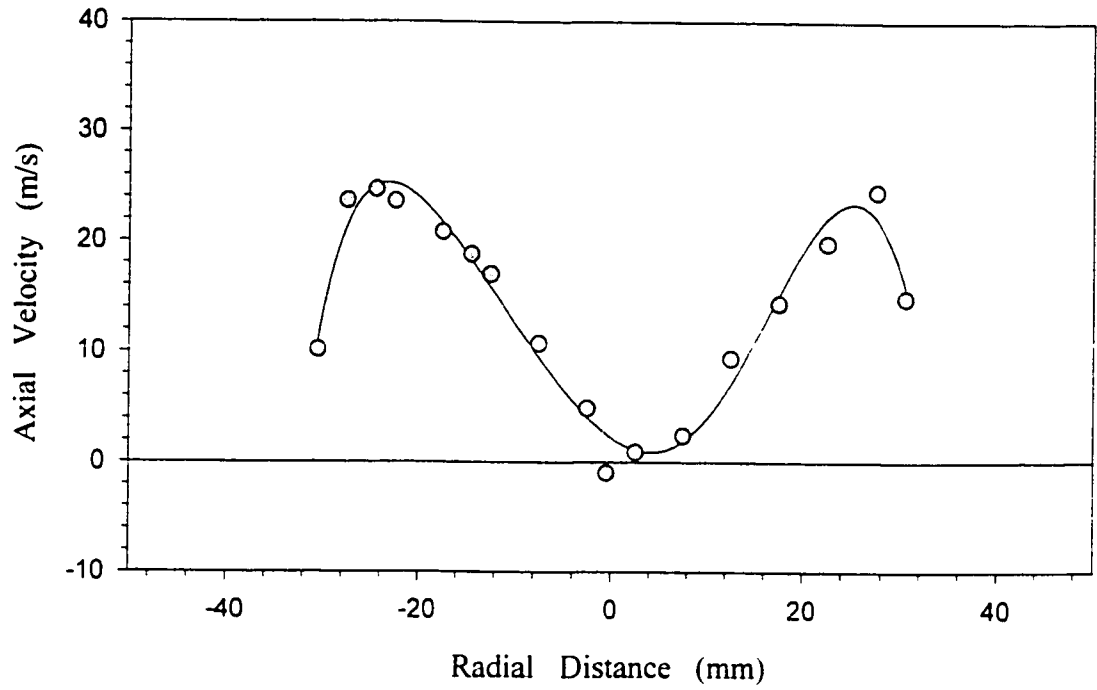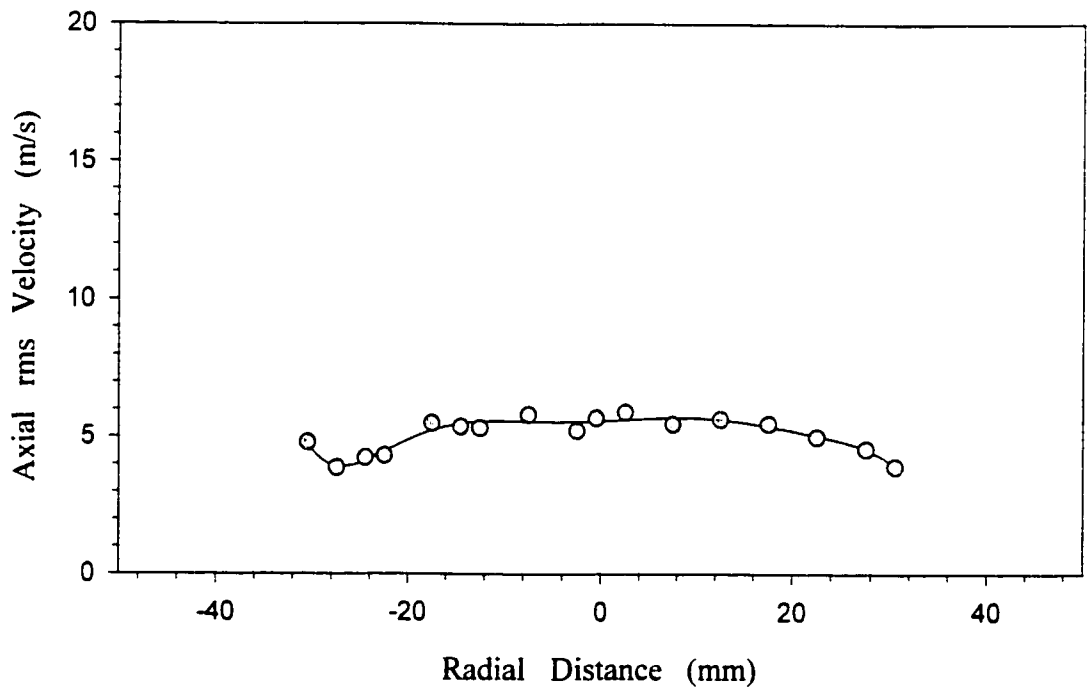outlet tube (with D_{outlet}/D_{barrel} = 0.33)
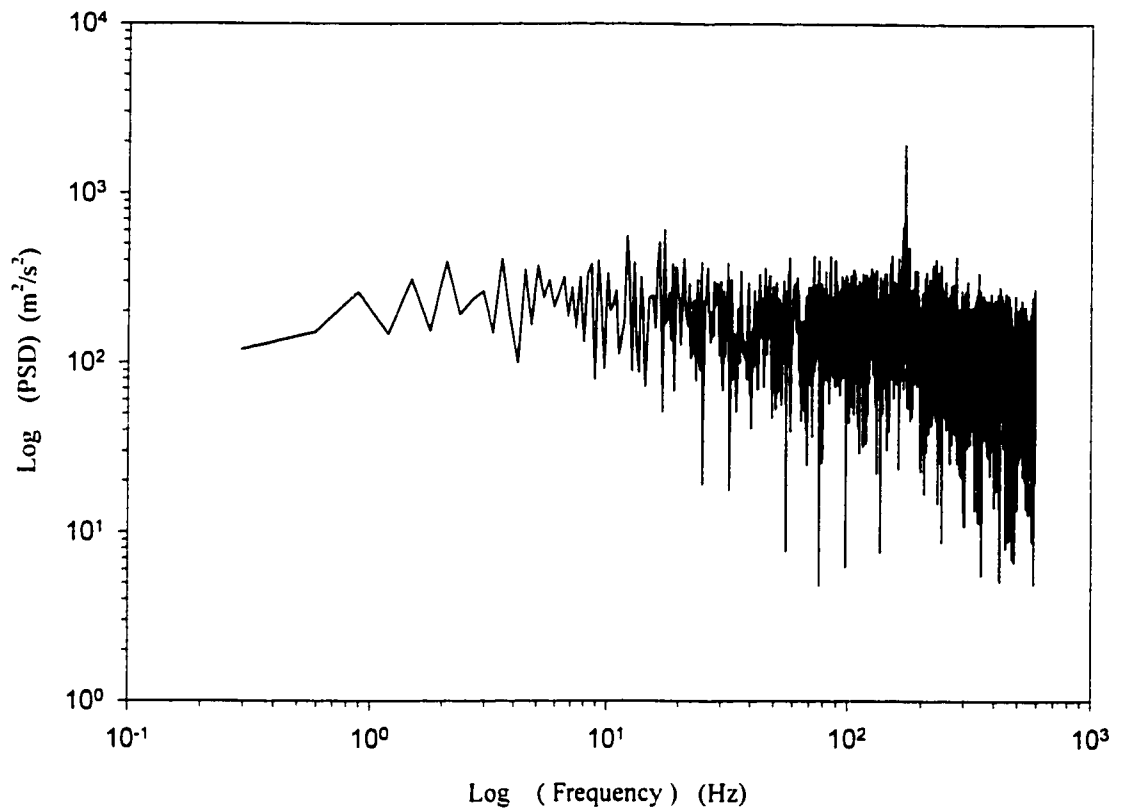
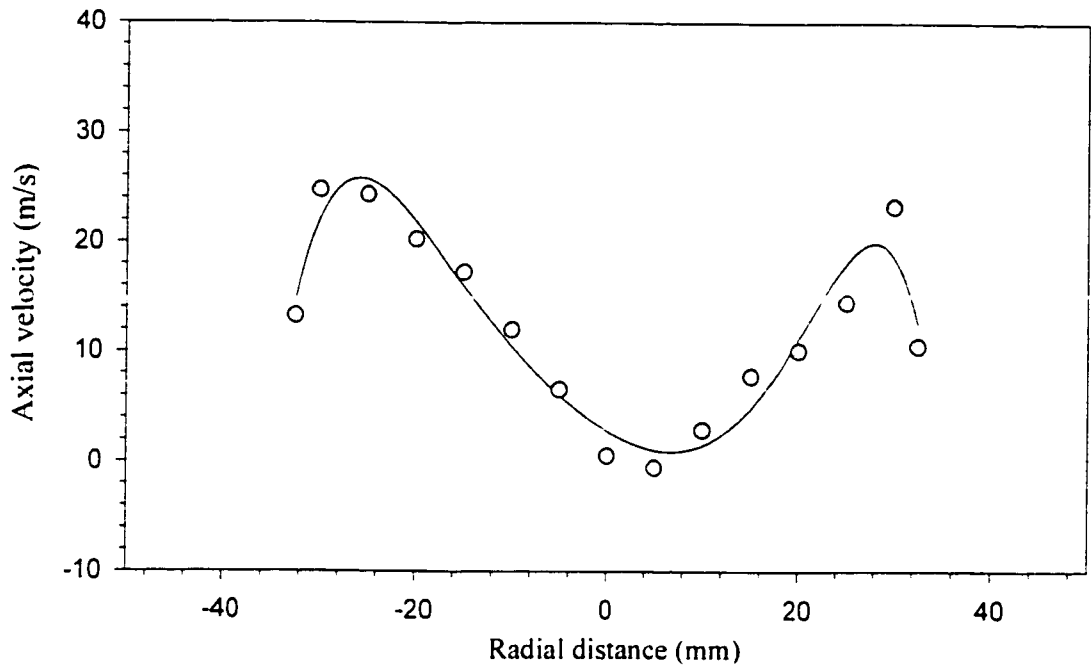Figure 3.52: Frequency analysis in cyclone outlet at
h_{top} = 160 mm and r = 35 mm (with D_{outlet}/D_{barrel} = 0.63)
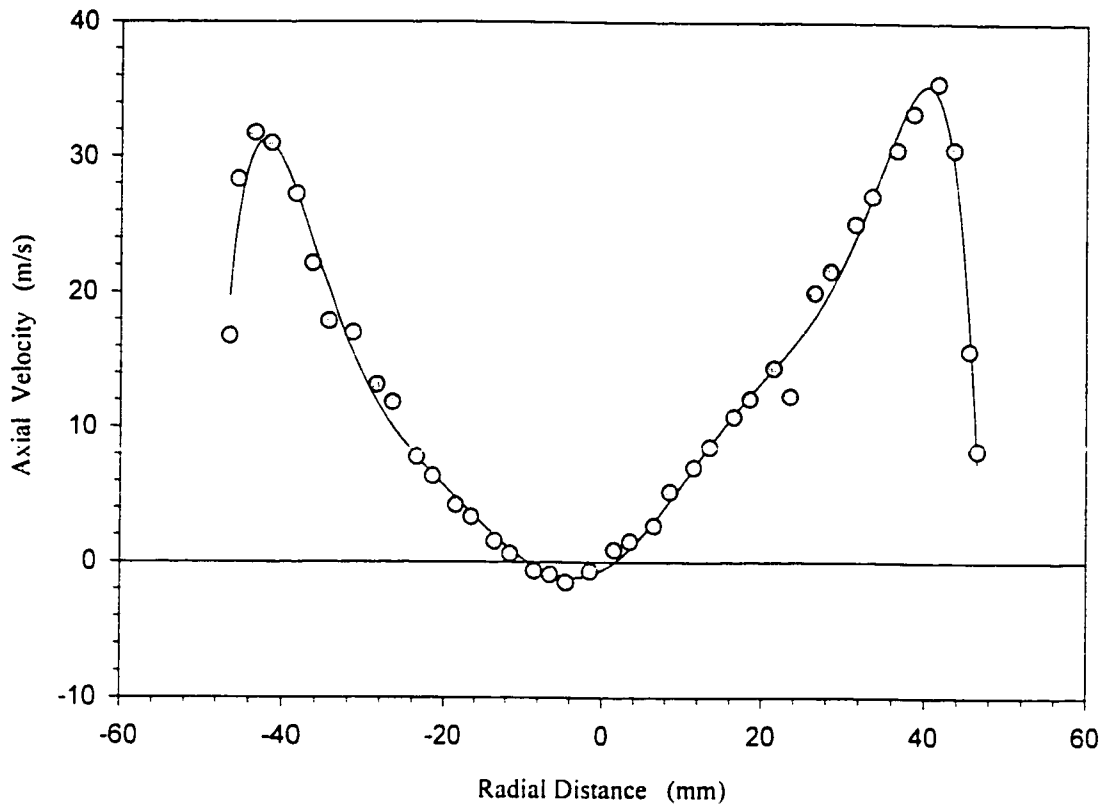
Figure 3.53: Axial velocity profiles 2 mm above the top of cyclone outlet tube (with $D_{outlet}/D_{barrrel} = 0.63$)
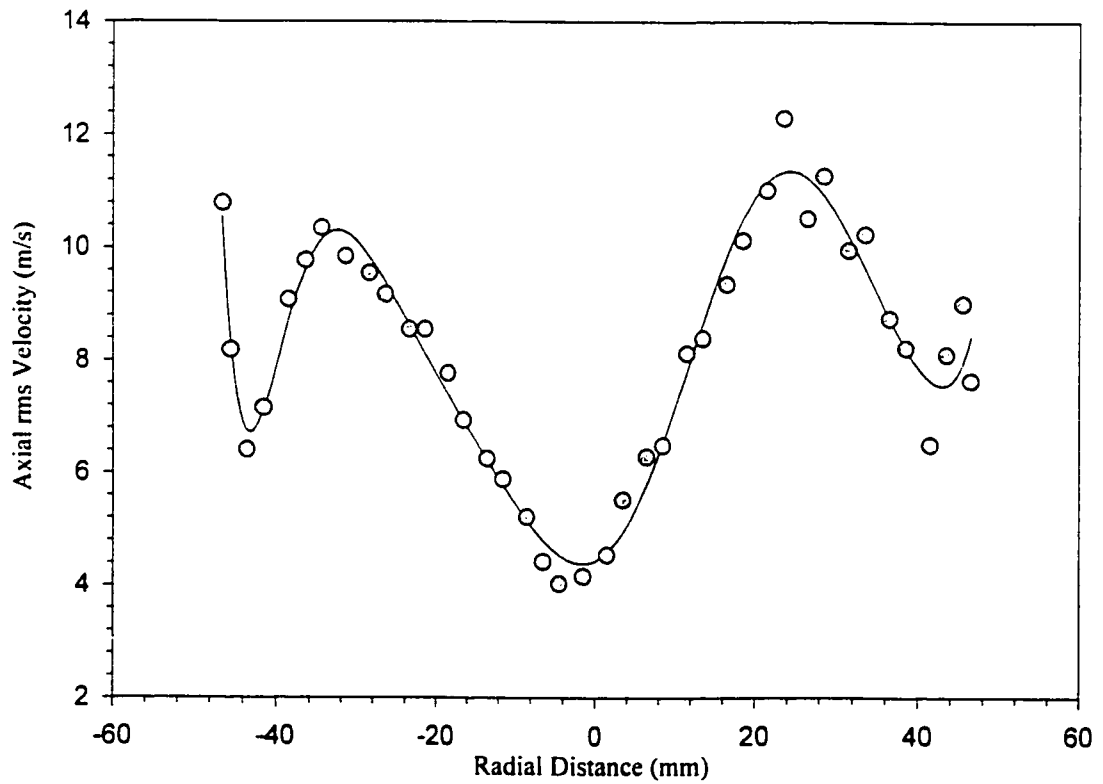
Figure 3.54: Axial rms velocity profile 2 mm above the top of cyclone outlet tube (with $D_{outlet}/D_{barrel} = 0.63$)

References:

Benjamin, T. B., 1962, *Theory of the vortex breakdown phenomenon*, J. Fluid Mech., **14**, 593-629.

Boysan, F., B.C.R. Ewan, J. Swithenbank, and W.H. Ayers, 1983. *Experimental and theoretical studies of cyclone separator aerodynamics*. I.Chem. E. Symp. Ser., **69**, 305-319.

Clark, R. L., W.F. Ng, D. A. Walker, and J. A. Schetz, 1990, *Large-scale structure in a supersonic slot-injected flowfield*. AIAA Journal. **28**, 1045-1051

Grabowski, W. J., and S. A. Berger, 1976, *Solutions of the Navier-Stokes equations for vortex breakdown*. J, Fluid Mech., **75**, 525-544

Faler, J.H., and S. Leibovich, 1977, *Disrupted states of vortex flow and vortex breakdown*. The Physics of fluids, **9**. 1385-1400

Hall, M.G., 1966. *The structure of concentrated vortex cores*. Progress in Aeronautical Sciences. **7**, 53-110

Hinze, J. O., 1975, *Turbulence*, 2nd edition, Mc Graw Hill, Toronto.

Hussain Fazle A.K.M. 1986, *Coherent structures and turbulence*. J. Fluid Mech. **173** 303-356.

Leibovich, S., 1984, *Vortex stability and breakdown: survey and extension*, AIAA Journal, **22**, 1192-1206.

Mees, A. J. Philip, 1990, *Spectrum analysis of randomly sampled signals, a review*, Internal report. University of Alberta, Edmonton.

Mees, P.A.J., 1997, *Three dimensional transient gas cyclone simulations*, 47th Canadian Chemical Engineering Conference, Oct. 5-8, Edmonton, Alberta. Paper 482.

Press, W.H., B.P. Flannery, S. A Teukolsky, and W. T. Vetterling, 1989, *Numerical Recipes, the art of scientific computing*, Cambridge University Press, New York.

Reynolds, A. J., 1975, *Turbulent flows in engineering.* John Wiley & Sons

Squire, H. B. 1960, *Analysis of the vortex breakdown phenomena.* Part1 , Aero. Dept., Imp. Coll. Rep. No.102

Wills, J. A. B. 1991, *Data sampling and data recovery,* Experiments in Fluids. **12,** 23-28

Chapter 4 Characterization of swirling flows in cyclone using dimensional analysis

Because the periodic component of flow is of primary interest in this study, it is desirable to develop a gross parameter descriptive of the expected dominant frequency, based on easily measured variables such as geometry and volumetric flow rate. This group will be used to correlate and then to anticipate oscillatory characteristics in scaled-up geometries. Of particular interest is the effect of the gas outlet tube diameter.

4.1 Dimensional analysis:

Dimensional analysis is a method by which we deduce information about a phenomenon based in the premise that the phenomenon can be correlated by a dimensionally correct equation among certain variables (Langhaar 1980). The result of dimensional analysis is a reduction in the number of variables in the problem. Non-dimensional parameters for a problem can be determined in two ways. They can be determined by applying Buckingham's Pi theorem to the variables involved, or they can be deduced directly from the governing differential equations, if these equations are known. These two methods will be illustrated for the case of the cyclone in the next two sections.

4.1.1 Buckingham's Pi theorem

Buckingham's theorem states that n variables can always be combined to form exactly $(n-r)$ independent non-dimensional variables, where r is the rank of the dimensional matrix, or the number of fundamental dimensions among the variables. Each non-dimensional parameter is called a Π number or more commonly a non-dimensional product.

The first step in the dimensional analysis of a problem is to decide what variables enter into the problem. Concerning the 3-dimensional time-dependent periodic motion in the cyclone, the oscillation frequency f in the gas outlet tube is expected to depend on the inlet velocity V_0, the gas outlet tube diameter D_e, the barrel diameter D_b, the inlet area

90

A_{in}, the fluid density ρ, and fluid viscosity μ. The functional dependence can be written as:

$$f = g(V_0, D_e, D_h, A_m, \rho, \mu) \qquad (4.1)$$

in which the rank of the determinant is $r=3$.

To obtain all the fundamental dimensions M (mass), L (length), and T (time), we can choose a characteristic velocity, a characteristic length, and a fluid property as the repeating variables in many fluid flow problems. In our case, V_0, D_e and ρ are chosen. Each non-dimensional product is formed by combining the three repeating variables with one of the remaining variable. The results are as follows:

$$\Pi_1 = V_0^a D_e^b \rho^c f = f D_e / V_0 \qquad (4.2)$$

$$\Pi_2 = V_0^a D_e^b \rho^c D_h = D_h / D_e \qquad (4.3)$$

$$\Pi_3 = V_0^a D_e^b \rho^c \mu = \rho V_0 D_e / \mu \qquad (4.4)$$

$$\Pi_4 = V_0^a D_e^b \rho^c A_m = A_m / D_e^2 \qquad (4.5)$$

Therefore, the nondimensional representation of the problem has the form:

$$\frac{f D_e}{V_0} = \phi\left(\frac{D_h}{D_e}, \frac{\rho V_0 D_e}{\mu}, \frac{A_m}{D_e^2} \right) \qquad (4.6)$$

The dimensionless products can also be obtained by combining the four above. For example, Π_1 can be a function of Π_3 and the formation of Π_4 / Π_2 and retain either Π_2 or Π_4, that is:

$$\frac{f D_e}{V_0} = \phi\left(\frac{\mu}{\rho V_0 D_e}, \frac{A_m}{D_h D_e}, \frac{D_h}{D_e} \right) \qquad (4.7)$$

Equation (4.7) states that the dimensionless frequency fD_e/V_0 is dependent on the

Reynolds number $D_e V_0 \rho / \mu$ and geometric ratio $D_b D_e / A_m$ and D_b / D_e. The form of

$D_b D_e / A_m$ is similar to the swirl number which will be discussed in the next section.

Although the Π-theorem can be employed most usefully for transforming a relationship of independent physical parameters into one of non-dimensional groups, the method has the disadvantage that it can be applied formally without requiring a better understanding of the reasons underlying modeling laws. It can also lead to dimensionless groups which are unfamiliar or irrelevant, though certainly valid regarding requirements of dimensional analysis. Making the governing equation dimensionless may help us understand the relationships between physical phenomena behind it. or between terms in the equation.

4.1.2 Nondimensional parameter determined from differential equations.

The governing differential equation describing the gas flow field in a cyclone is the Navier-Stokes equation:

$$\rho \frac{Dv}{Dt} = -\nabla p + \mu \nabla^2 v \tag{4.8}$$

here, the body force is neglected.

Choosing the characteristic length, D_e, and characteristic velocity, V, which is the mean axial velocity in the cyclone, gives a characteristic time, D_e / V. Once this choice has been made, we may define the following dimensionless variables and differential operators:

$$v^{\bullet} = \frac{v}{V}; \quad p^{\bullet} = \frac{p - p_0}{\rho V^2}; \quad t^{\bullet} = \frac{tV}{D_e}; \quad x^{\bullet} = \frac{x}{D_e}; \quad y^{\bullet} = \frac{y}{D_e}; \quad z^{\bullet} = \frac{z}{D_e}$$

$$\nabla^{\bullet} = D_e \nabla = (\delta_1 \frac{\partial}{\partial x^{\bullet}} + \delta_2 \frac{\partial}{\partial y^{\bullet}} + \delta_3 \frac{\partial}{\partial z^{\bullet}})$$

$$\nabla^{*\,2} = D_e^2 \nabla^2 = \frac{\partial^2}{\partial x^{*\,2}} + \frac{\partial^2}{\partial y^{*\,2}} + \frac{\partial^2}{\partial z^{*\,2}}$$

by setting $v = v^* V$, $p - p_0 = p^* \rho V^2$, etc

$$\rho \frac{V^2}{D_e} \frac{Dv^*}{Dt^*} = -\frac{1}{D_e}\rho V^2 \nabla^* p^* + \mu \frac{V}{D_e^2}\nabla^{*\,2} v^* \qquad (4.9)$$

Since $f = \dfrac{V}{D_e}$ (neglecting physical meaning. it has the same units as frequency),

$Q = \dfrac{\pi}{4} D_e^2 V$. substituting them into equation (4.9). and omitting *'s. we obtain

$$\frac{f D_e^3}{Q} \frac{Dv}{Dt} = -\frac{4}{\pi}\nabla p + \frac{4}{\pi}\frac{1}{Re}\nabla^2 v \qquad (4.10)$$

in which $Re = \dfrac{D_e V \rho}{\mu}$.

The Strouhal number is defined as $\dfrac{f D_e^3}{Q}$ in this study, although the original form of the

Strouhal number is $\dfrac{f D_e}{V}$. The Strouhal number is a dimensionless group often used in

time-dependent motion. Equation 4.10 indicates that the Strouhal number $\dfrac{f D_e}{V}$ is at least

a function of Reynolds number. Experiments have shown that the dimensionless

frequency is a function of both swirl number and Reynolds number (Griffiths et al. 1998).

For strongly turbulent flows, it is often assumed that turbulent diffusion dominates the

structure in such a way that the terms in equation (4.10) involving $\dfrac{1}{Re}$ can be neglected.

This suggests that at high Re number, the Strouhal number should be independent of the

Reynolds number.

4.2 Swirl number

The most commonly used parameter for the characterization of swirling flows is the swirl number S_w, which is a non-dimensional group representing the axial flux of swirl momentum divided by the axial flux of axial momentum times the equivalent nozzle radius (Gupta et al.1984). In a physical sense, the swirl number represents how much axial momentum the swirl needs to maintain advancing and rotating motion.

Experimental studies show that the degree of swirl imparted to the flow has a large-scale effect on the flow field. For example, in combustion, increasing the swirl can cause jet growth, entrainment, and progressively enhanced decay. The combustion intensity (reacting flows) is affected by the degree of swirl imparted to the flow (Lilley, 1977). Various forms of swirl number have been suggested. For example, in a jet, the swirl number S_w is related approximately by

$$S_w = \frac{2}{3}\tan\varphi \qquad (4.11)$$

in which φ denotes the swirl vane angle. This expression illustrates that the swirl vane angle is the key factor in determining the swirl in a jet since it is this angle that decides the ratio of tangential component to axial component of velocity. The purpose of determining the swirl number is to quantify the flow phenomena, since the low swirl phenomena are quite different from high swirl phenomena. For example, strongly swirling flows (approximately $S_w > 0.6$) possess sufficient radial and axial pressure gradients to cause a central tororidal recirculation zone, which is not observed at weaker degrees of swirl. Cassidy and Falvey (1970) have also shown that a series of non-dimensionalized parameters are useful for characterizing the precessing vortex core in swirling flow. One of them is a momentum parameter $\Omega D_e / \rho Q^2$, which can also be related to the swirl number.

From the definition of swirl number, the swirl expression in a cyclone can be derived by the following procedure:

The axial flux of angular momentum G_θ into a volume V through the surface element dA is:

$$G_\theta = (r \times w)(\rho u \cdot dA) \tag{4.12}$$

since $\rho u \cdot dA$ is the axial mass flux through the surface element and $r \times w$ is the angular momentum per unit mass. Here r and u correspond to the location of dA. The axial flux of axial (linear) momentum is:

$$G_z = u(\rho u \cdot dA) \tag{4.13}$$

since u is the axial momentum per unit mass. Integrating over the area under consideration, the swirl number can be expressed as:

$$S_w = \frac{G_\theta}{G_z \cdot R_e} = \frac{1}{R_e} \frac{\int_A (r \times w)\rho u \cdot dA}{\int_A u\rho u \cdot dA} = \frac{1}{R_e} \frac{\int_0^R 2\pi \rho r^2 uw\, dr}{\int_0^R 2\pi \rho r u^2\, dr} \tag{4.14}$$

Here R_e is the exhaust radius which is the radius of the gas outlet tube in the cyclone. The parameters of axial flux of angular momentum, which is the numerator of equation (4.14), are taken from the barrel of the cyclone, since this is the input angular momentum. The gas outlet parameters of the cyclone are applied for the calculation of axial flux of axial momentum that is in the denominator of equation (4.14), since this is the exit momentum.

The swirl number should, if possible, be calculated from measured values of velocity. As this is frequently not possible owing to a lack of detailed experimental results, the swirl number may be estimated from the geometry of the cyclone. To simplify equation (4.14) to this form, three assumptions are made:

1) Uniform axial velocity profiles are imposed in both the barrel and the gas outlet tube, although this is a major simplification. The basis for this assumption is from analysis of plug flow in a free jet.

2) The local swirl velocity can be adequately represented by the inlet velocity.

95

3) All the gas flow exits from the gas outlet tube.

Applying these three assumptions, equations (4.12) and (4.13) become:

$$G_\theta = \int_0^R 2\pi\rho r^2 uw\, dr = \frac{2}{3}\pi\rho R_b^3 wu = \frac{2}{3}\frac{\rho Q^2 R_b}{A_m}$$

(4.15)

$$G_z = \int_0^R 2\pi\rho r u^2\, dr = \pi\rho R_e^2 u^2 = \frac{\rho Q^2}{\pi R_e^2}$$

(4.16)

in which A_m is the tangential inlet area, R_b is the barrel radius, and Q is the volumetric flow rate at the inlet. Substituting (4.15) and (4.16) into equation (4.14), we obtain the swirl number:

$$S_w = \frac{2\pi}{3}\frac{R_b R_e}{A_m}$$

(4.17)

The expression for swirl number in equation (4.17) is a little different from the literature (Yazdabadi et al. 1994). The difference is that they do not have the coefficient 2/3 in the expression of the swirl number.

The other way to simplify the equation is to assume that angular momentum is conserved throughout the cyclone, instead of assuming a constant global swirl velocity. Then in equation (4.14), $r \times w$ can be taken out of the integral. The final expression for swirl number is:

$$S_w = \frac{\pi R_b R_e}{A_m}$$

(4.18)

Equation (4.18) is the same definition as used by Yazdabadi et al. (1994). Comparing (4.18) to the term $A_{in}/D_b D_e$ in equation 4.7, we can conclude that $A_{in}/D_b D_e$ term describes the swirl motion in cyclone. The expression (4.18) is employed for swirl number in the remainder of this study.

4.2.1 Generation of swirl and calculation of swirl number

Swirling flows are generated by three principal methods:

(a) tangential entry of the fluid stream, or of a part of it, into a cylindrical duct;

(b) the use of guide vanes in axial tube flow;

(c) rotation of mechanical devices which impart swirling motion to the fluid passing through them. This includes rotating vanes or grids and rotating tubes.

The swirl generated in a cyclone belongs to (a). Swirling flows having similar swirl generators can be characterized by the non-dimensional swirl number which is device-independent. The study of the swirl number is to provide criteria to compare the flow phenomena in similar generators. As mentioned before, when lacking accurate measurements of local velocity in a cross section in cyclone and velocity varying along the flow over the integral, we have to make several assumptions. This can cause significant errors. For example, for higher degree of swirl, the axial velocity distribution deviates considerably from plug flow, and the major portion of the flow leaves the gas outlet near the outer edge (as shown in the previous chapter). Therefore the theoretical correlation (4.16) will provide too low an estimate of the linear momentum. The same situation occurs for calculation of angular momentum. For example, when calculating the G_θ from equation (4.15), the deviation can be 20% compared with the original form of equation (4.12), where we use the velocity profile at the top of the cyclone to calculate of the angular momentum in equation (4.12). Table 4.1 describes these errors in three different gas outlet tube diameters.

Although using the geometry of the cyclone to calculate the swirl number is just a rough estimate, it gives us the basic criteria to compare swirling flow phenomena in similar geometries.

4.3 Strouhal number

The Strouhal number is applied in frequency scaling for periodic flow structures. It is often used to characterize the oscillating wake in a Karman vortex street downstream of a circular cylinder. The passage of regular vortices causes the velocity measurements in the wake to have a dominant periodicity. The frequency f is expressed as a nondimensional parameter known as Strouhal number, defined as:

$$S_{tr} = fd / U_\infty$$ (4.19)

in which U_∞ is the upstream velocity, and d is the cylinder diameter. The Strouhal number cannot be interpreted as physically as the Reynolds number which is a ratio of forces, but Zierep (1971) explains it as the ratio of the local acceleration to the convective acceleration in a flow field.

Shih *et al.* (1992) measured the frequency of oscillations near a laminar boundary layer at the exit of a rectangular jet. By using the laminar boundary momentum thickness as the length scale in the Strouhal number and jet exit velocity as the uniform velocity, i.e. $S_{tr} = f\theta / U_c$, in which θ is the initial momentum thickness, they concluded that the jet's preferred Strouhal number is approximately proportional to the square root of the Reynolds number.

In our study, the form used for Strouhal number is:

$$S_{tr} = \frac{fD_e^3}{Q}$$ (4.20)

since all the flow quantities are known at the exit, and it is easy to compare these results with the available references.

In our experiment, the inlet volumetric flow rate is obtained by the inlet velocity distribution measurement. The axial velocity profile at the top of the gas outlet tube is also measured, giving us a volumetric flow rate at the exit as well. Since the inlet volumetric flow rate is lower than that of the outlet due to the compressibility of gas, all

the volumetric flow rate calculations at different gas outlet tube diameters are based on the flow at the top of the gas outlet tube. The frequency of the oscillation is obtained by analyzing the time series record using a fast Fourier transformation after binning the original data from the measurement.

4.4 Results

Three dimensionless parameters $4Q / \pi D_e \nu$ (Reynolds number), $\dfrac{fD^3}{Q}$ (Strouhal number),

and $\dfrac{\pi R_h R_e}{A_m}$ (swirl number) are utilized to correlate the experimental data on frequency.

From Fig. 4.1, a plot of Strouhal number versus average-velocity Reynolds number at different swirl number shows that the dimensionless frequency of the flow increases rapidly with the increasing swirl number or Reynolds number but tends to have the trend to become constant at a particular value of Reynolds number except $S_w = 4.26$. This also indicates that the frequency of the flow is indeed essentially independent of viscosity for a very large Reynolds number which is consistent with the dimensional analysis in section 4.2. The three lines with swirl number 2.208, 2.626 and 3.043 are taken from Yazdabadi 's geometry (1994). They fall approximately in the range that agrees with our data. The reference data also show that there could be a minimum critical Reynolds number below which no periodic motion would occur at any swirl number (the three lines in reference do not pass through the origin when they are extended).

In Fig. 4.2, all the data collapse onto one line when S_{tr}/S_w versus Reynolds number is plotted. At high Reynolds numbers, the measurements show more scattering. This could be due to the uncertainties at high velocity measurement. The figure indicates that for different geometries, the S_{tr}/S_w ratio is approximately a constant at a given Reynolds number, i.e. the non-dimensional frequency scales linearly with the swirl at a given Reynolds number. The ratio of S_{tr}/S_w increases parabolically with the Reynolds number till 50000. Beyond that critical Reynolds number, it seems that the non-dimensional frequency is only dependent on the swirl number.

These figures provide us with the information needed to predict the oscillation frequency for different geometries and fluid properties. For example, if we scale up the geometry with the same inlet velocity, the swirl number will be the same as before, and the Reynolds will be increased, this will lead to a frequency decrease according to the above correlation. Hot air flow with the same geometry and same volumetric flow rate will cause a decrease in the frequency of the periodic motion in the cyclone since the combined effect on the viscosity and density will lead to a Reynolds number decrease.

Table 4.1 Simplified calculation of both angular momentum and linear momentum errors for three different gas outlet diameters

	$D_{outlet} / D_{barrel} = 0.3$	$D_{outlet} / D_{barrel} = 0.5$	$D_{outlet} / D_{barrel} = 0.63$
G_θ Error Eq. 4.12 vs. Eq. 4.15	22.3 %	19.5 %	16.8 %
G_z Error Eq. 4.13 vs. Eq. 4.16	35.2 %	34.3 %	25.8 %
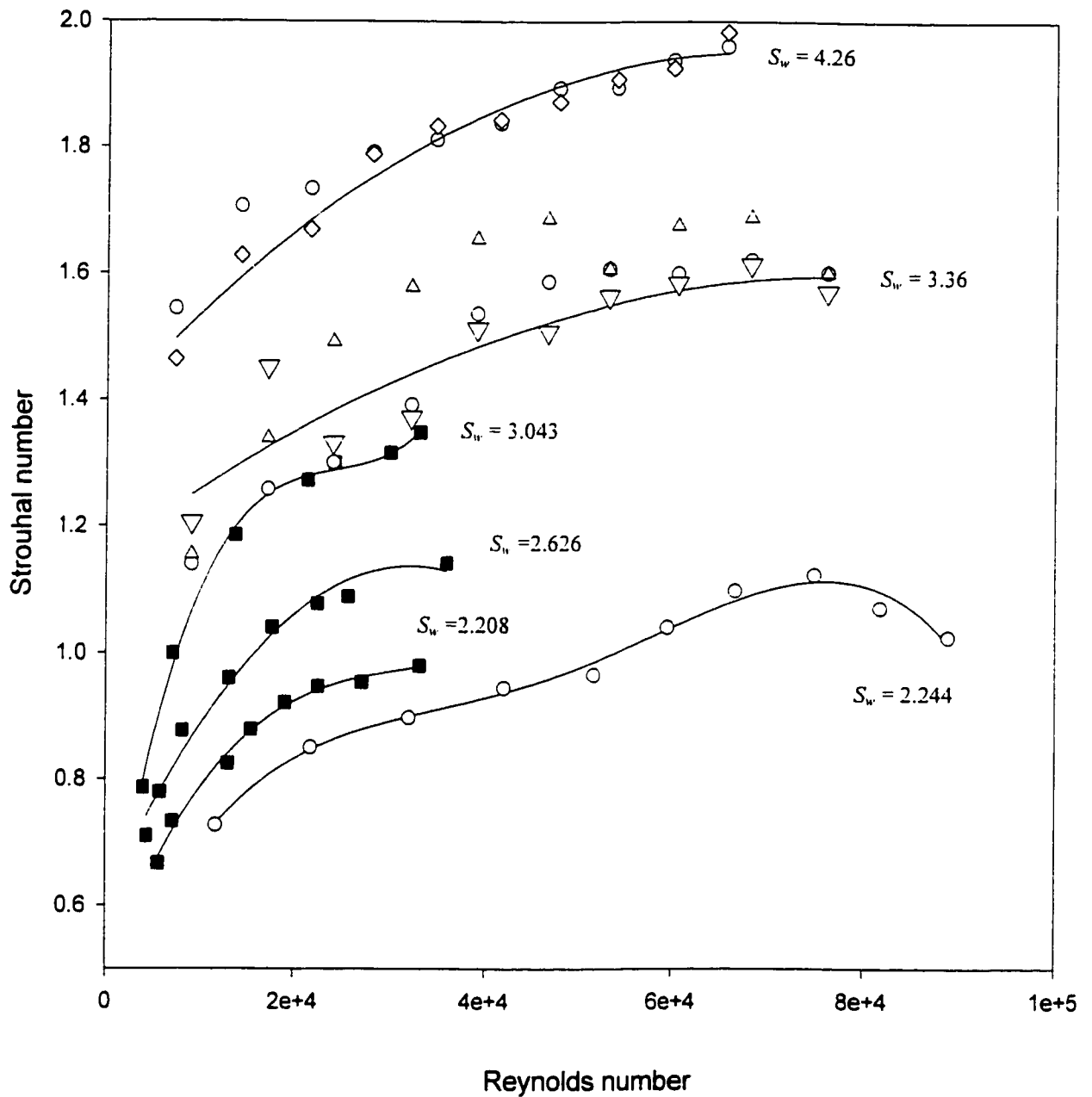
Figure. 4.1 Frequency parameter as a function of Reynolds number
(Filled square symbols represent data from reference
Yazdabadi et al (1994) and open simbols are our data)

101
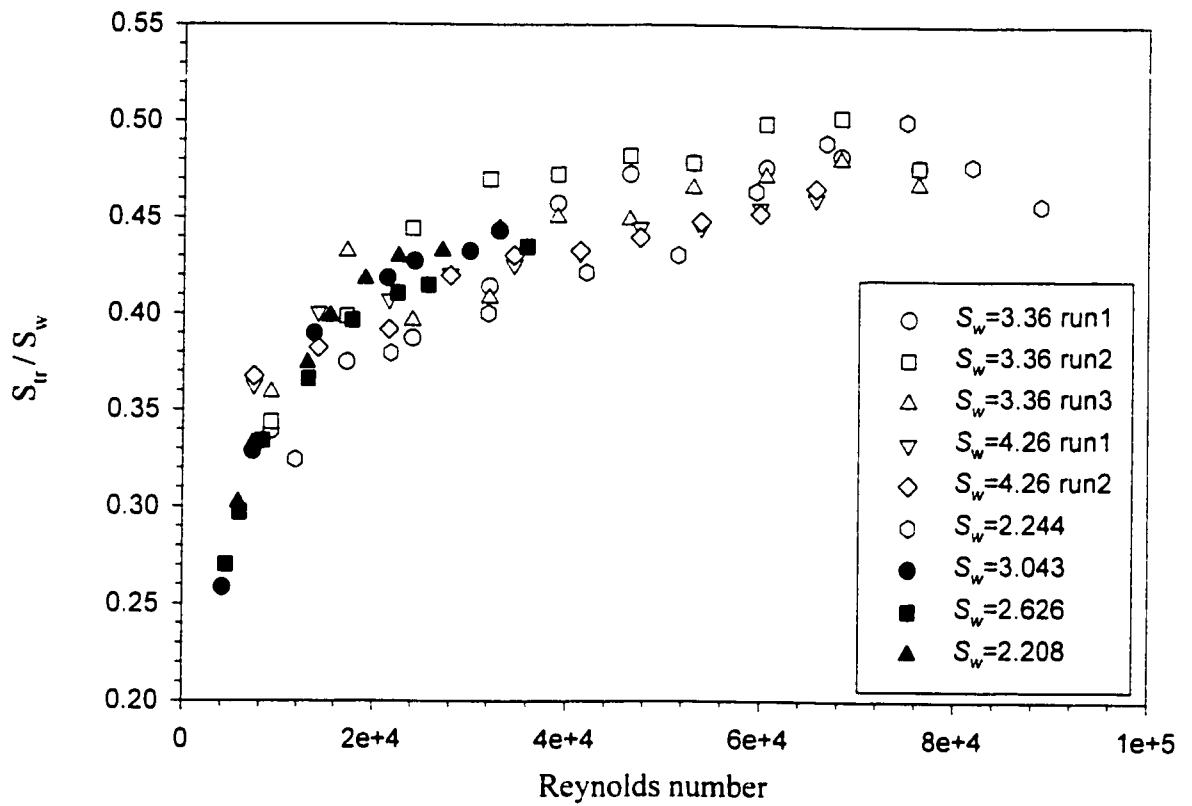
Fig.4.2 Frequency swirl ratio as a function of Reynolds number.
Open symbols are our experimental data and filled
symbols represent data from reference (Yazdabadi 1994)

Reference:

Cassidy, John J., and Henry T. Falvey, 1970, *Observations of unsteady flow arising after vortex breakdown*. J.Fluid Mech, 41, 727-736

Griffiths, A.J., P.A. Yazdabadi, and N. Syred, 1998, *Alternative eddy shedding set up by the nonaxisymmetric recirculation zone at the exhaust of a cyclone dust separator.* Journal of Fluids Eng., 120, 193-199.

Gupta, A.K., D. G. Lilley, N. Syred, 1984, *Swirl flows*. Abacus Press

Langhaar, L. Herry, 1980, *Dimensional analysis and theory of models* Huntigton, N.Y.

Lilley, David. G., 1977, *Swirl flows in combustion: A review.* AIAA Journal, 15, 1063-1078

Shih, C., A. Krothapalli, and S. Gogineni, 1992. *Experimental observation of instability modes in a rectangular jet.* AIAA Journal, 30, 1992.

Yazdabadi, P.A., A.J. Griffiths, and N. Syred, 1994. *Investigations into the precessing vortex core phenomenon in cyclone dust separators.* Proc. I. Mech. E., 208, 147-154.

Zierep, J., 1971, *Similarity laws and modeling*, Marcel Dekker, Inc. New York

Chapter 5: Computational Techniques

5.1 Introduction

It is not always feasible to measure the flow field accurately in all regions of a cyclone. Hence, there are few detailed data on the three-dimensional flow field in large-scale cyclones. On the other hand, Computational Fluid Dynamics (CFD) could potentially provide a complete picture of the flow field. At its current level, CFD has been useful primarily for understanding the important qualitative features of a flow system for engineering applications.

Use of Computational Fluid Dynamics (CFD) codes by the engineering community has increased dramatically in the last few years, as several commercial CFD codes have become available for this puopose. Each code has its advantages and disadvantages and none of them are perfect in dealing with complex flow systems. Freitas (1995) has made constructive comments on commercial CFD package based on five-selected benchmark simulation results.

In this investigation, the commercial CFD code FLUENT has been used. It has been found to be capable of predicting the flow field in cyclones.

5.2 Computational Fluid Dynamics Solver FLUENT

5.2.1 Mathematical Formulation

FLUENT solves the partial differential equations for the conservation of mass, momentum and energy in a general form which can be written in Cartesian tensor notation as:

$$\underbrace{\frac{\partial}{\partial t}(\rho\phi)}_{transient} + \underbrace{\frac{\partial}{\partial x_i}(\rho\upsilon_i\phi)}_{convection} = \underbrace{\frac{\partial}{\partial x_i}[\Gamma_\phi\frac{\partial\phi}{\partial x_i}]}_{diffusion} + \underbrace{S_\phi}_{dissipation} \qquad (5.1)$$

Where ϕ is the conserved quantity, S_ϕ is a source term for ϕ and Γ_ϕ is an exchange coefficient. Equation (5.1) gives rise to a large set of non-linear simultaneous equations. These equations can be solved with various numerical algorithms. The equations are

reduced to their finite-difference analogues by integrating over the computational cells into which the domain is divided. After discretization, the resulting algebraic equations in two dimensions for a general variable ϕ_P can be written in the following common form:

$$A_P \phi_P = A_E \phi_E + A_W \phi_W + A_N \phi_N + A_S \phi_S + S_C \qquad (5.2)$$

Where

$$A_P = A_E + A_W + A_N + A_S - S_p \qquad (5.3)$$

The nomenclature for these equations is displayed in Figure 4.1 which shows a typical computational cell surrounding the node n_p with neighboring nodes n_e, n_u, n_s and n_v. The coefficients A_E, A_W, A_N, A_S are the finite difference coefficients which combine convection and diffusion through the control volume surrounding node n_p. The quantities S_P and S_C are components of the linearized source terms obtained in the finite difference equation. $S_\phi = S_C + S_P \phi_P$, which incorporates any terms that do not fall into the convection/diffusion form (5.1). n_p is the central node relative to a computing cell and the summation is over the neighboring finite difference cells. Three different spatial discretization schemes were used for the interpolation between grid points and for the calculation of the derivatives of flow variables: power-law, second-order upwind, and QUICK, a bounded third-order method. These features are accessible through a graphical-user interface permitting problem definition, problem solution, and post-processing. The interested reader is referred to the user's guide for FLUENT (1998). In this investigation, discretization is done using a second-order finite difference upwind scheme

Pressure/velocity coupling is achieved in the SIMPLE algorithm resulting in a set of algebraic equations which are solved by a line-by-line tridiagonal multigrid method and/or block-correction in terms of the primitive variables. The discretization and the solution algorithm are well documented. A detailed discussion of the advantages and disadvantages of the schemes may be found elsewhere, for example, Patankar (1980).

5.2.2 Turbulence Models

Turbulent motion is extremely difficult to predict theoretically and experimentation is expensive. In turbulent flows, the velocity at a point is considered as a sum of the mean (time average) and fluctuating components:

$$u_i = \overline{u_i} + u_i'$$

(5.4)

The time-averaged momentum equation applied by FLUENT for turbulent flow is:

$$\frac{\partial}{\partial t}(\rho u_i) + \frac{\partial}{\partial x_i}(\rho u_i u_j) = \frac{\partial}{\partial x_j}(\mu[\frac{\partial u_i}{\partial x_j} + \frac{\partial u_j}{\partial x_i}] - \frac{2}{3}\mu\frac{\partial u_i}{\partial x_i}) - \frac{\partial p}{\partial x_i} + F_i + \rho g_i + \frac{\partial}{\partial x_j}(\rho\overline{u_i'u_j'})$$

(5.5)

FLUENT ignores the term $\frac{2}{3}\mu\frac{\partial u_i}{\partial x_i}$ under the assumption that the divergence of the velocity is negligible compared to the strain rate. The effect of turbulence is incorporated through the "Reynolds stresses" $\overline{u_i'u_j'}$.

Generally, turbulence models relate the turbulent Reynolds stresses $\overline{u_i'u_j'}$ to the average velocity gradient $\frac{\partial U}{\partial x_i}$ by simple relationships as reviewed by White (1991) and Rodi (1980). The selection of a turbulence model for CFD prediction of flow fields is always a concern. Of the more recent models, the κ-ε model, which was developed for isotropic, free shear flows, has received wide acceptance in engineering applications. Details of the transport equations with the standard κ-ε turbulence models in cylindrical coordinates have been presented elsewhere (Ranade & Joshi, 1989). However, the turbulent flow driven by the swirling motion in cyclone is not isotropic. FLUENT uses the standard κ-ε turbulence model as default, but FLUENT also provides three options to select a non-isotropic turbulence model for some applications. They are the Reynolds stress model (RSM), the renormalized group κ-ε two-equation model (RNG), and large eddy

simulation (LES). Detailed analysis of the three turbulence models is beyond the scope of this study. The interested reader can find reference by Moin (1995) and Launder (1974). In this study, we select the RSM model as our turbulent model.

RSM model: The Reynolds Stress Model involves the calculation of the individual Reynolds stresses, $\overline{u_i' u_j'}$ via a set of differential equations of the form:

$$\frac{\partial}{\partial t}(\overline{u_i' u_j'}) + u_k \frac{\partial}{\partial x_k}(\overline{u_i' u_j'}) = -\frac{\partial}{\partial x_k}[\overline{u_i' u_j' u_k'} + \frac{\overline{P}}{\rho}(\delta_{kj} u_i' + \delta_{ik} u_j') - v \frac{\partial u_i'}{\partial x_k}(\overline{u_i' u_j'})]$$

$$-[\overline{u_i' u_k'} \frac{\partial u_j'}{\partial x_k} + \overline{u_j' u_k'} \frac{\partial u_i'}{\partial x_k}] + \frac{\overline{P}}{\rho}[\frac{\partial u_i'}{\partial x_j} + \frac{\partial u_j'}{\partial x_i}] - 2v[\overline{\frac{\partial u_i'}{\partial x_i} \frac{\partial u_j'}{\partial x_i}}] - 2\Omega_k[\overline{u_j' u_m'}\varepsilon_{ikm} + \overline{u_i' u_m'}\varepsilon_{jkm}]$$

$$(5.6)$$

FLUENT approximates several of the terms in the above equation in order to close the set of equations. First, the diffusive transport term is described as a scalar coefficient:

$$-\frac{\partial}{\partial x_k}[(\overline{u_i' u_j' u_k'}) + \frac{\overline{P}}{\rho}(\delta_{kj} u_i' + \delta_{ik} u_j') - v \frac{\partial}{\partial x_k}(\overline{u_i' u_j'})] = \frac{\partial}{\partial x_k}(\frac{v_i}{\sigma_k} \frac{\partial}{\partial x_k}\overline{u_i' u_j'})$$

$$(5.7)$$

Secondly, the pressure-strain term is approximated as:

$$\frac{\overline{P}}{\rho}[\frac{\partial u_i'}{\partial x_k} + \frac{\partial u_j'}{\partial x_k}] = -C_3 \frac{\varepsilon}{k}[\overline{u_i' u_j'} - \frac{2}{3}\delta_{ij} k] - C_4[P_{ij} - \frac{2}{3}\delta_{ij} P]$$

$$(5.8)$$

where C_3 and C_4 are empirical constants whose values are $C_3 = 1.8$ and $C_4 = 0.60$. Furthermore, $P = \frac{1}{2} P_{ii}$, where

$$P_{ii} = -\overline{u_i' u_k'} \frac{\partial u_j}{\partial x_k} - \overline{u_j' u_k'} \frac{\partial u_i}{\partial x_k}$$

$$(5.9)$$

Finally, the dissipation rate term in Eq. 5.6 is assumed to be isotropic and is approximated via the scalar dissipation rate:

$$2v\overline{\frac{\partial u'_i}{\partial x_k}\frac{\partial u'_l}{\partial x_k}} = \frac{2}{3}\delta_{ij}\varepsilon \qquad (5.10)$$

The dissipation rate, ε, is computed via the transport equation as follows:

$$\rho\frac{D\varepsilon}{Dt} = \frac{\partial}{\partial x_j}[(\mu + \frac{\mu_t}{\sigma_\varepsilon})\frac{\partial\varepsilon}{\partial x_j}] + C_{\varepsilon 1}\frac{1}{2}[P_{ii}+C_{\varepsilon 3}G_{ii}]\frac{\varepsilon}{k} - C_{\varepsilon 2}\rho\frac{\varepsilon^2}{k} \qquad (5.11)$$

5.2.3 Computational domain, boundary conditions and time step

In swirling flows, the centrifugal forces created by the circumferential motion are in equilibrium with the radial pressure gradient:

$$\frac{\partial p}{\partial r} = \frac{\rho\omega^2}{r} \qquad (5.12)$$

As the distribution of angular momentum evolves, the form of this radial pressure gradient also changes, driving radial and axial flows in response to the highly non-uniform pressures that result. It is this high degree of coupling between the swirl and pressure field that makes the modeling of swirling flows complex. One strategy for solving swirling flow (not used in this work) is to start the calculations using a low inlet swirl velocity, increasing the swirl gradually in order to reach the final desired operating condition. In this work, the simulations were started with the k-ε model. Once the general pattern flow developed, the RMS was invoked.

The geometry of the cyclone was built in CFX-Flow3D with Cartesian coordinates. Cartesian coordinates avoid the singularity problem at r=0 which arise if cylindrical coordinates are used. Due to run-time problems with CFX-Flow3D, the geometry file was imported into FLUENT. The geometry of the cyclone, and the direction and origin of the Cartesian coordinates are shown in Figure 5.2. The rectangular inlet duct was not modeled in the simulation; only a patch from which the flow entered was simulated. In

simulation, the gas outlet barrel ration is kept as 0.50, no different diameters have been tried.

The grid size affected the accuracy as well as the efficiency of the numerical predictions. Generally, a fine grid will yield better accuracy at the cost of additional computations. A trade-off is often made to decide the optimum grid size for a particular application. Many authors have studied the effect of the grid size on the numerical predictions for the flow field in swirling flows. The detailed grid size of the cyclone under study is given in Butts (1996). In our study, we have tried three grid size. Since the grid is non-uniform, table 5.1 only provides a rough estimate of the grid size.

The boundary conditions at the inlet were measured values of mean velocities, turbulence kinetic energy k and turbulence energy dissipation rate ε. Remaining boundary conditions were determined as given in the report by Butts (1996). The boundary conditions are summarized as follows:

- Velocity inlet boundary condition was imposed at the rectangular inlet patch with only y component to be non-zero.

- A 3% mass flow condition was imposed at the underflow (bottom of the cyclone).

- An atmospheric pressure boundary condition was imposed at the overflow (top of the cyclone) with specification of a static (gauge)pressure at the outlet boundary and all other quantities being extrapolated to the outlets from the interior.

- The no slip condition was applied at the wall and on both surfaces of the gas outlet tube.

- FLUENT has the wall function built in as default. A detailed description of the wall function is available (Launder & Spalding, 1974; Rodi, 1980). The wall function has several advantages: (i) it requires less computer time and storage, (ii) it allows the introduction of additional empirical information, and (iii) it produces relatively accurate results with fewer node points in the near-wall region. In essence, the wall function relates the slip velocity near the wall U_w to the wall shear τ_w through the universal log law of the wall as:

$$(5.13)$$

-

$$\tau_w = \frac{\rho U_w (C_D^{\frac{1}{2}} \kappa^{\frac{1}{2}})^{\frac{1}{4}} K}{\log(Ey^+)}$$

-

- where K, U_w, E and y^+ are, Von Karmann's constant, the absolute value of the velocity tangential to the wall, the roughness constant and the wall Reynolds number, $\frac{\dot{u} y}{\mu}$ respectively. The friction velocity $\dot{u}$ is equal to $(\frac{\tau_w}{\rho})^{\frac{1}{2}}$. The derivation of the wall function assumes an equilibrium between the generation and dissipation of turbulence kinetic energy.

Since the simulation is time-dependent, the initial maximum time step was determined using the Courant number. For a stable solution, the Courant number should be smaller than 1.

$$c = \frac{u \Delta t}{\Delta x} \qquad (5.14)$$

The Courant number is the ratio of time step Δt to the characteristic convection time, $u/\Delta x$, and is the time required for a disturbance to be convected a distance Δx. For $c<1$, $\Delta t<\Delta x/u$. In our grid, $\Delta x/u$ is about 10^{-3}, to get a converged solution at the beginning, 10^{-4} was chosen as the initial time step.

FLUENT defines the residual as the imbalance in Eq. 5.2, summed over all the computational cells P. When the residuals are scaled, FLUENT scales the residual using a scaling factor representative of the flow rate through the domain.

$$\overline{R} = \frac{\sum_{cellsn_p} |[A_E \phi_E + A_W \phi_W + A_N \phi_N + A_S \phi_S + S_C - A_P \phi_P]|}{\sum_{cellsP} |(A_P \phi_P)|} \qquad (5.15)$$

FLUENT defines the residual for pressure as the imbalance in the continuity equation:

$$R_{pressure} = \sum_{cellP} |(C_W - C_E + C_S - C_N)| \qquad (5.16)$$

where C_W, C_E, C_S, and C_N are the convection of mass (kg/s) through each face of the control volume surrounding node P. Scaled pressure residual is accomplished by dividing

110

by the residual at the largest absolute value of the continuity residual in the first five iterations:

$$\overline{R}_{pressure} = \frac{R_{iterationN}}{R_{iteration5}} \qquad (5.17)$$

The scaled residual is a more appropriate indicator of convergence for most problems. In our study, within each time step, the mass residual converged to less than 1×10^{-3} within less than 20 iterations. The scaled residuals of ε converged to less than 1×10^{-5}, as recommended (Fluent Inc., 1998). The solution process for the 3 dimensional, transient CFD calculation is summarized in Figure 5.3.

5.2 Validation of CFD results

In computational fluid dynamics, the validity of the numerical solution is usually established by comparing the predicted flow field with well known cases of the phenomenon under study. The quantity of numerical data acquired from the three-dimensional simulation is extremely large. Experimental data are not as plentiful as numerical results. Therefore, the validation of the numerical CFD results is confined by the available experimental data. The evaluation of the results of the numerical predictions then becomes a reasonable task.

The validation of the CFD simulation has been performed with the following objectives:

• Swirling motion in cyclone. This should include accurate results for the swirling motion in both barrel and the outlet. The swirling motion in the barrel is shown in Figure 5.4. In Figure 5.5, the swirl velocity exhibits the familiar Rankine vortex profile of a cyclone with the location of the two peaks of the simulation coincide with the experiment peaks, but the agreement is qualitative only.

• Two vortices in the flow field, i.e. outer downward vortex and inner upward vortex. Figure 5.6 shows the velocity vectors in a xz plane with large upward flow in the middle and a small amount flow downward near the wall.

The qualitative agreement between the numerical CFD prediction and the experimental data is discussed in the next section.

5.3 Numerical results versus experimental results

Based on validation of the CFD numerical prediction for the basic flow pattern in cyclone, a prediction of periodic motions in different elevations on monitoring points is presented. The mean velocity and the fluctuation velocity in comparison with experimental data are to be analyzed.

Before presenting the results, the quantities obtained in the numerical simulation have to be clarified due to the presence of periodic motion. To analyze the flow field in the context of more general theories, let us consider the fluctuating velocity U_f or velocity disturbance. This is defined as:

$$U_f = U_{inst} - U_{Ta} \tag{5.18}$$

where U_{inst} is the instantaneous velocity, and U_{Ta} is the time-averaged (mean) velocity. The instantaneous velocity is divided into two components in order to isolate the turbulence from the mean flow field. Tropea *et al.* (1989) suggest that a further separation is necessary for a flow field containing periodicity:

$$U_f = U_{tur} + U_p \tag{5.19}$$

$$U_{tur} = U_{inst} - (U_{Ta} + U_p) \tag{5.20}$$

In this later representation, U_{tur} is the randomly (true) fluctuating portion of velocity. U_p is the periodic portion of velocity at time t. The sum of $U_{Ta} + U_p$ is the ensemble-averaged mean velocity U_{EM}. In simulation, the time varying mean velocity is the ensemble-averaged mean velocity. The axial fluctuating velocities are obtained by making square root of the Reynolds stress $\overline{w'^2}$.

It is important to note that the solutions obtained from the CFD simulations are unlikely to be of any greater accuracy than results from, for example, the experimental data. Hence the CFD simulations, at the current level of development, are primarily a tool for understanding the important features of a system and for predicting trends for scale-up purposes.

5.4 Prediction of the frequency of oscillation

The periodic motion observed in experiment was predicted by the numerical simulation. Figure 5.7 is the mean axial velocity (no turbulent fluctuating part) varying with time in the gas outlet tube. The flow is marked with periodic motion oscillating at about 135 Hz which is about half of the frequency of the experimental at the same inlet velocity ($V_{in}=26.677m/s$ and the $f_{exp}=260Hz$). Frequency analysis is no longer necessary since the frequency of the oscillation can be calculated easily from the time varying plot when no turbulent fluctuating velocity is showing there. By changing the inlet velocity, the frequency of oscillation changes as well. This can be shown on the second and third part of the oscillations in Figure 5.7. The frequency of oscillation scales with the inlet velocity at the same slope as the experiment (Figure 5.8).

The time varying mean velocities in barrel and cone have also been plotted, they do not show any stable oscillations (Figure 5.9 and 5.10). This is consistent with experimental results. Contours of velocity or pressure at certain cross sections can help us understand the global flow field in the cyclone. Figure 5.11 shows the contours of axial velocity in which blue and red are downward and upward velocity respectively. At the very top center part of the gas outlet tube, the axial velocity is negative which indicates the existence of back flow. It is interesting to note that there is a helical wave in the cone. This may reveal that the periodic motions at the top of gas outlet tube are attributed to helical waves triggered by dynamic instability in the upstream flow at the cone. A rather fascinating feature, not readily identifiable from Figure 5.11, but clearly visible in the animation is that the helix emanates from the bottom of the cyclone, moving along a circular trajectory, centered around the axis. As clearly seen in the animation, the spiral rotates in the same direction as the inlet flow.

5.4.1 Time averaged velocity prediction

The time averaged velocity is obtained by integrating the time varying velocity over one complete cycle. This is quite complicated, since the history information of velocity cannot be stored in the data file in FLUENT, instead, only the last interation information is retained. The time varying velocities can only be stored at several monitoring points, and FLUENT 5.0.2 only allows 11 monitoring points at maximum. Although FLUENT can autosave the data file at specific intervals during a calculation, this requires huge amount of disc space. In our case, the time varying data are acquired through the monitoring points. Figure 5.12 and Figure 5.13 show the time averaged axial velocity and rms velocity profile at a $z=0.738m$ (corresponding to the position of 90mm from the top of gas outlet in experiment) in comparison with the experimental results. It indicates that the simulation can follow the basic trend of the experimental data but under predicts both the mean and the fluctuating velocity. The time averaged mean velocity and fluctuation velocity profile are plotted at another elevation of 135mm from the top of gas outlet tube (Figure 5.14 and Figure 5.15). In Figure 5.14, the time averaged mean velocity agree quite will with the experiments, i.e. the basic flow at this position has been predicted, but the fluctuating velocity (Figure 5.15) is in extremely poor agreement with the measured levels. This discrepancy is because in experiment, both random turbulent fluctuation and periodic motion contribute to the rms velocity, but in simulation, only turbulence fluctuations are counted in the Reynolds stress.

From the above comparison, it can be concluded that the application of the CFD techniques has advanced to an extent that once a set of reliable boundary conditions has been provided, the numerical visualization of the entire flow field can be achieved with **reasonable** accuracy. On the other hand, the experimental measurements are quite limited due to the experimental difficulty including seeding in the center. It should be emphasized that the results of the numerical CFD simulations presented here give a **qualitative** understanding of the overall flow characteristic rather than **precise** numerical values themselves.

5.4.2 Solution sensitivity

A gird resolution study, performed by refining the number of grid points at the nearest layer of boundary and at the near z axis region (as shown on Figure 5.16), which results in 5 times the number of cells as the original one, did not significantly alter the results. All the cells in this calculation are in hexahedral shape. The diagonal appeared in the cells in Figure 5.15 is due to the projection of the side of cells from the other layers. The time step sensitivity and differencing scheme sensitivity have also been examined. The time averaged mean velocity changes when using a different size of time step as shown on Figure 5.17. Switching from the higher upwind (second order accurate) discretization scheme to the quick (third order accurate) scheme does not change the solution.

5.5 Possible reasons for the discrepancy between experiment and simulation

The difference between the numerical results of the CFD simulations and the experimental data can be mainly attributed to approximations in the modeling, the boundary conditions, and possibly to uncertainty in the experimental data. We discuss some of these below.

- Wall function approximation:

The application of a wall function is needed since not all turbulence models are valid in the near wall region ($y^* < 30$). The wall function approach works well when the underlying assumption of an equilibrium turbulent boundary layer is satisfied. This assumption breaks down when the boundary layer contains a significant pressure gradient, a near stagnant or re-attachment point, or a region of high curvature. The physical presence of swirling flow provides the highest curvature. It is suspect to assume equilibrium between the turbulence energy production rate and turbulence energy dissipation rate in such a flow. It may be better to investigate such a flow field by avoiding the wall function. FLUENT has extended the RSM model to the near wall region but it requires more demanding computing resources. It is still not clear that the extended RSM model will give more reasonable results, especially for the highly swirling flow in cyclone.

- Uncertainty in static pressure:

In the CFD simulations with FLUENT, no static pressure information is needed as input in the boundary condition for starting the calculations, as long as the flow field is not a supersonic flow. FLUENT assumes that the static pressure in the flow field follows from the pressure set up by the flow through the domain. However, in a flow with strong swirling motion, it is the high degree of coupling between the swirling motion and the pressure gradient that makes the CFD simulations so complex as shown in Eq. 5.12. The uncertainty in static pressure may be a reason for some of the unreasonable results from the current version of FLUENT.

- Uncertainty of the experimental data

Velocity bias is an error indigenous in the statistical analysis from the individual realizations of the LDA measurements. The probability of measuring a velocity larger than mean is greater than the probability of measuring a velocity slower than the mean. The reason for this is that at high velocities, more fluid and more seeding particles pass through the probe volume, per unit time, than at lower velocity. Thus the statistical mean velocity is expected to be biased towards the high velocity (McLaughlin & Tiederman, 1973). This bias is believed to be systematic (Edwards, 1987). Several bias corrections have been proposed and discussed. However, none is perfect. Edwards (1987) recommends a residence time weighting correction. Since in our measurement, there is no correction for mean velocity, and the gas flow is quite high. This kind of bias may exist.

- Uncertainty of the boundary conditions

At the top of the gas outlet tube, we impose a pressure boundary condition, i.e. the value of static pressure is used. All other flow quantities are extrapolated from the interior. This boundary condition can greatly attenuate the swirl in the cyclone. For this highly swirling flow, the outlet pressure boundary condition may contribute significantly to the improper prediction of numerical simulation.

5.6 Conclusion:

The FLUENT code employed in this investigation has been briefly discussed including the mathematical formulations, a brief discussion of the discretization, the algorithm, the turbulence models as well as the boundary conditions. The numerical CFD simulations for the flow field are presented here with emphasis on the qualitative description of flow characteristics. It can be concluded that the predicted flow patterns are qualitatively correct. The oscillation frequency predicted by the simulation is about half of the measured ones although the frequency still scales with the inlet velocities. The time averaged mean velocity agree well with the experiments. These CFD simulations have been shown to be effective in capturing the essential features of the flow field.

Table 5.1 Grid resolution, number of cells (since the grid the non-uniform along the diameter, the cells along the z axis is counted at the nearest cells to the wall in which most of the cells have been refined)

	Size (m)	Fine grid (number of cells)	Medium grid (number of cells)	Coarse grid (number of cells)
Gas outlet tube diameter	0.03805	17	13	12
Barrel diameter	0.0761	7	6	6
Gas outlet tube height	0.1912	36	36	18
Barrel height	0.2348	68	34	34

Cone height	0.375	30	30	15
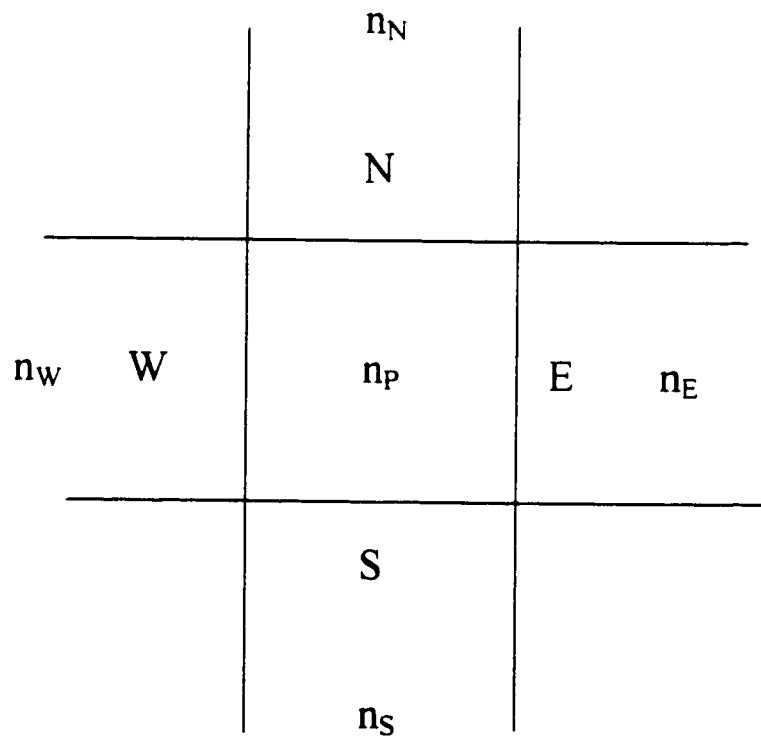
Figure 5.1: Schematic representation of a typical 2D-computational cell surrounding node n_P
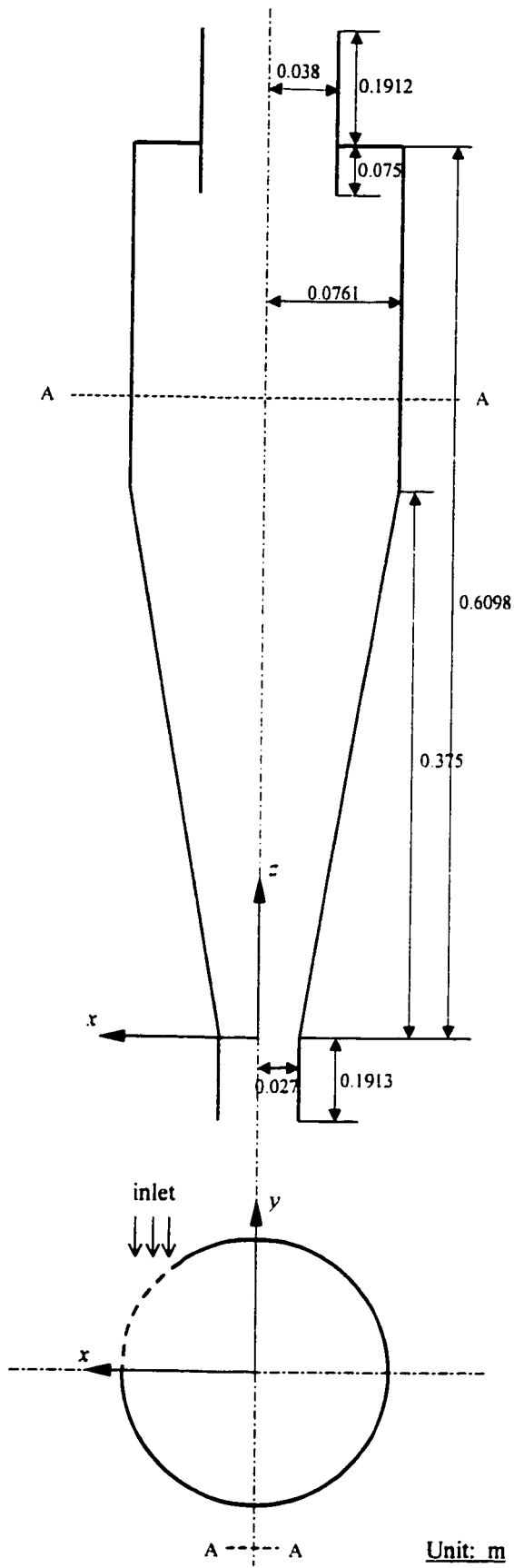
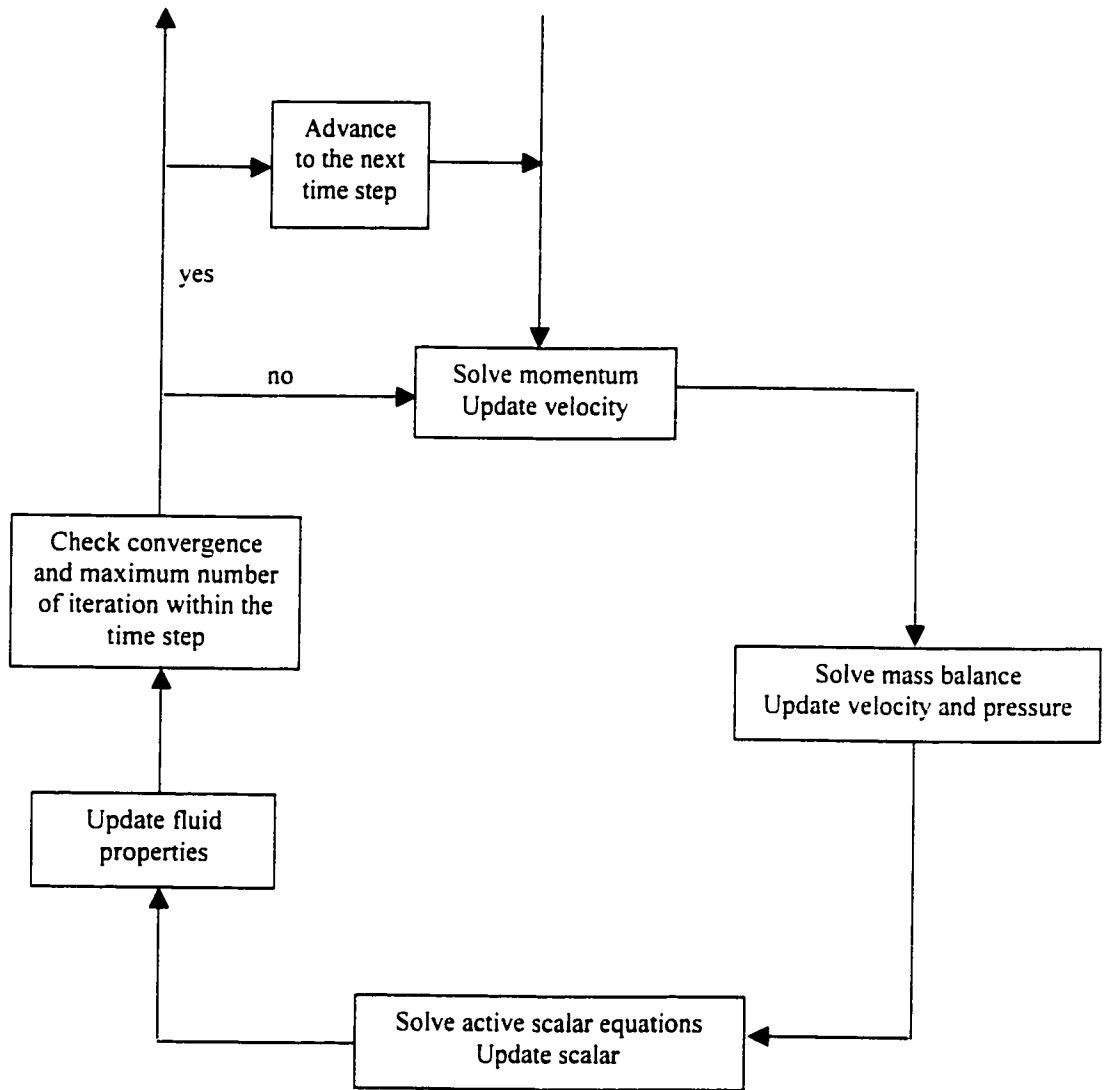Figure 5.2: Cyclone model in simulation

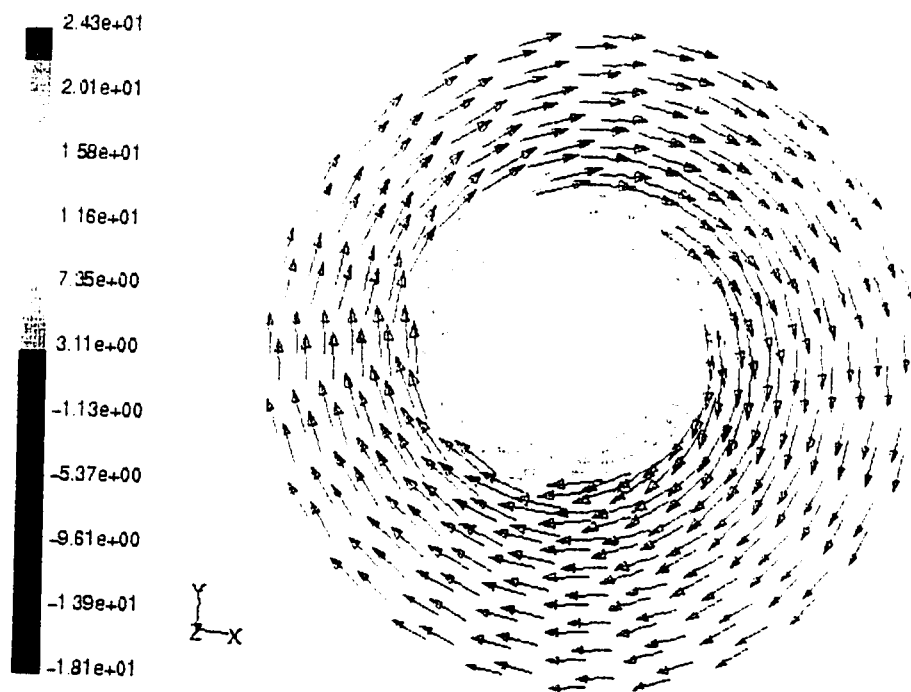Figure 5.3: Overview of the numerical solution process

Figure 5.4: Velocity vector in barrel at z=0.401m when V_{in}=26.667 m/s

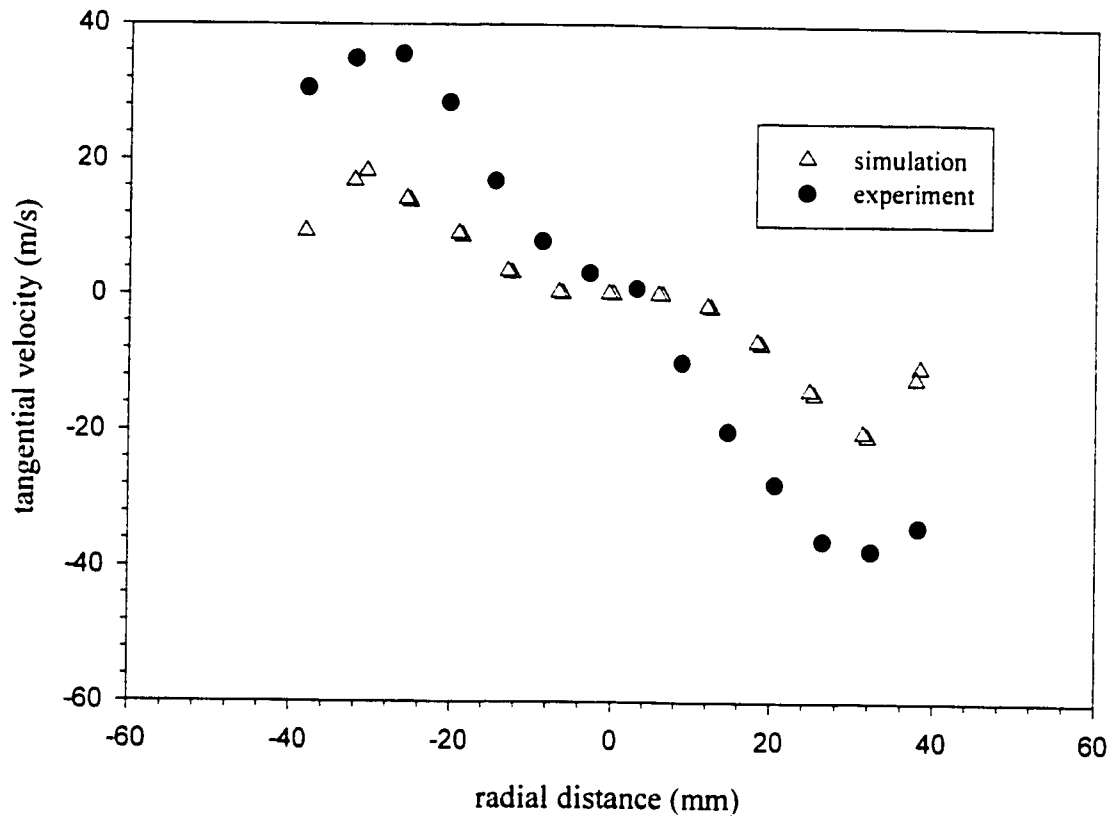Figure 5.5 Comparison of tangential velocity profile at the top of the cyclone outlet tube (with D$_{outlet}$/D$_{barrel}$ = 0.5)
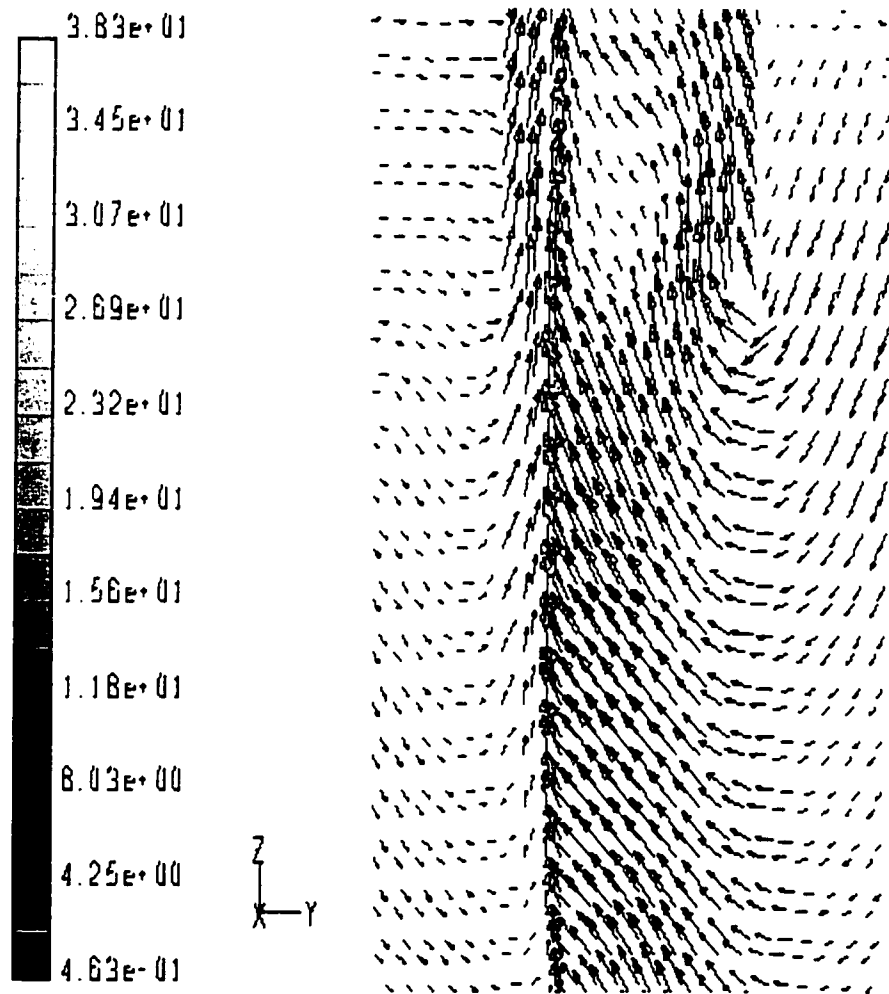
Figure 5.6: Velocity vector of axial and radial velocity
at x=0 cross section of z=0.35 to z=0.39
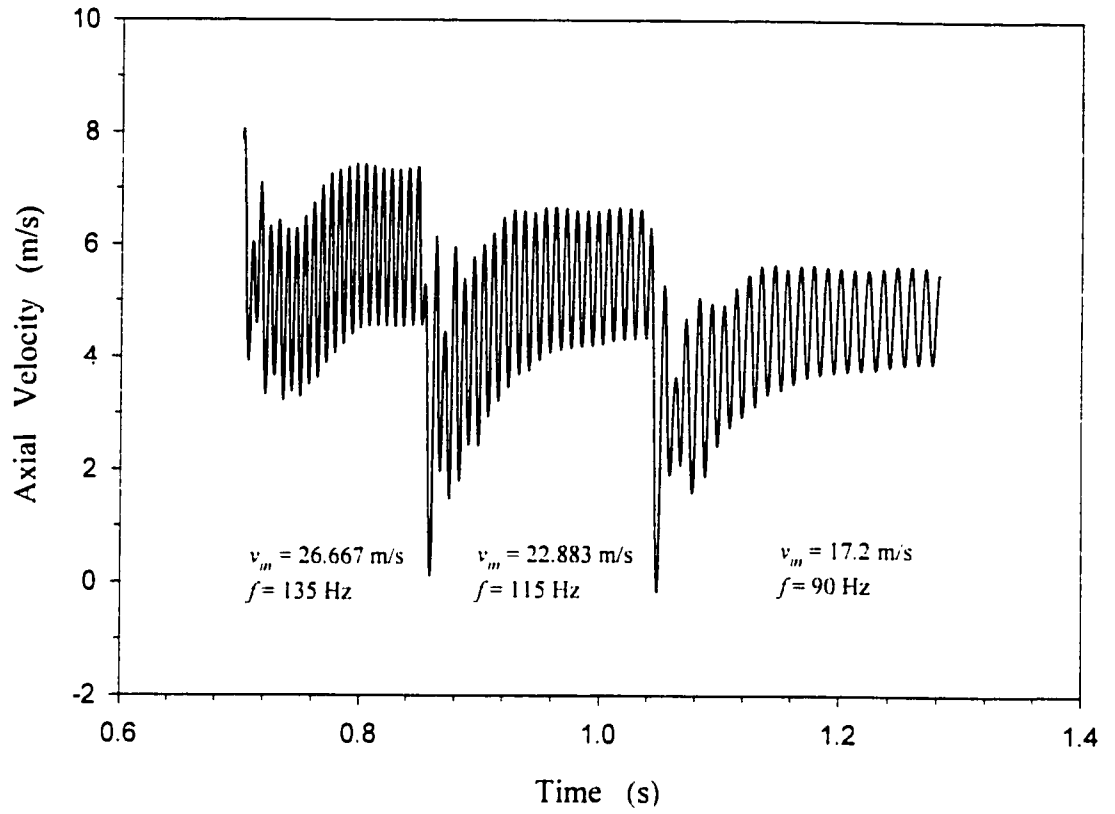
Figure 5.7: Oscillation predicted by simulation
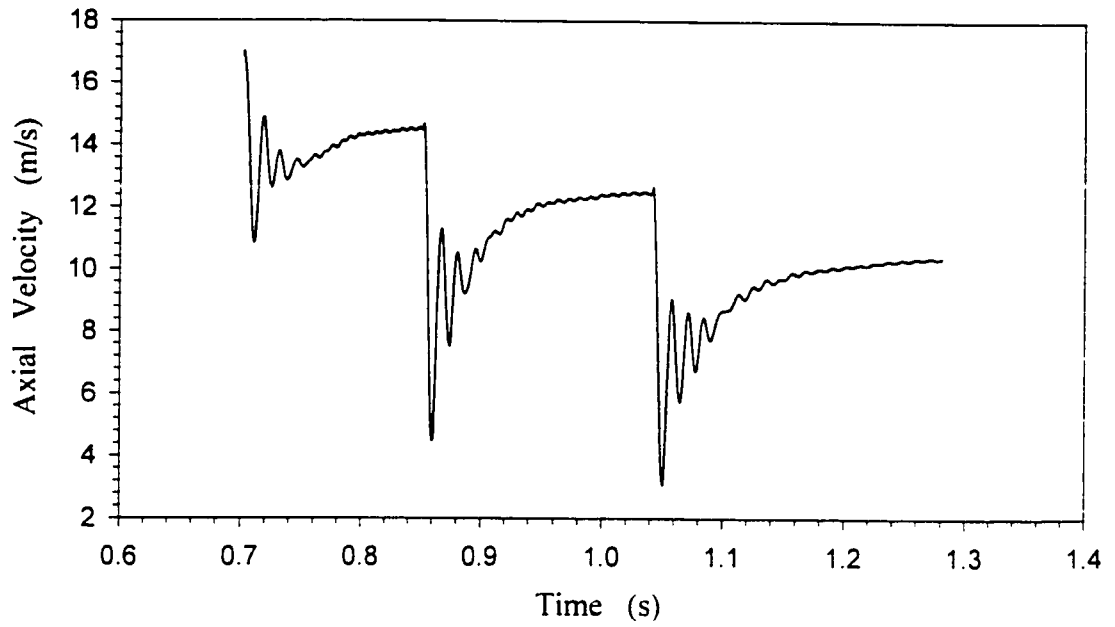at a point at z = 0.65 m and r = 5 mm

124
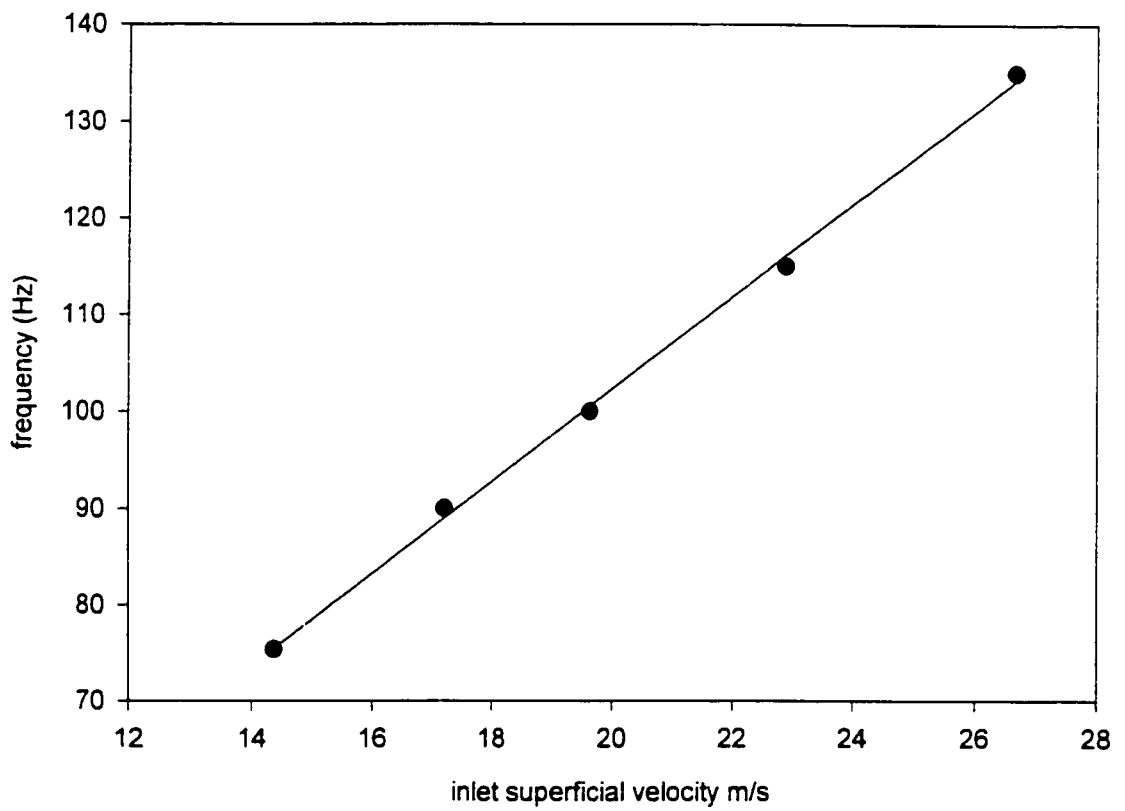
Figure 5.8. Frequency change with time in numerical simulation

Figure 5.9: Oscillation damping predicted by numerical simulation
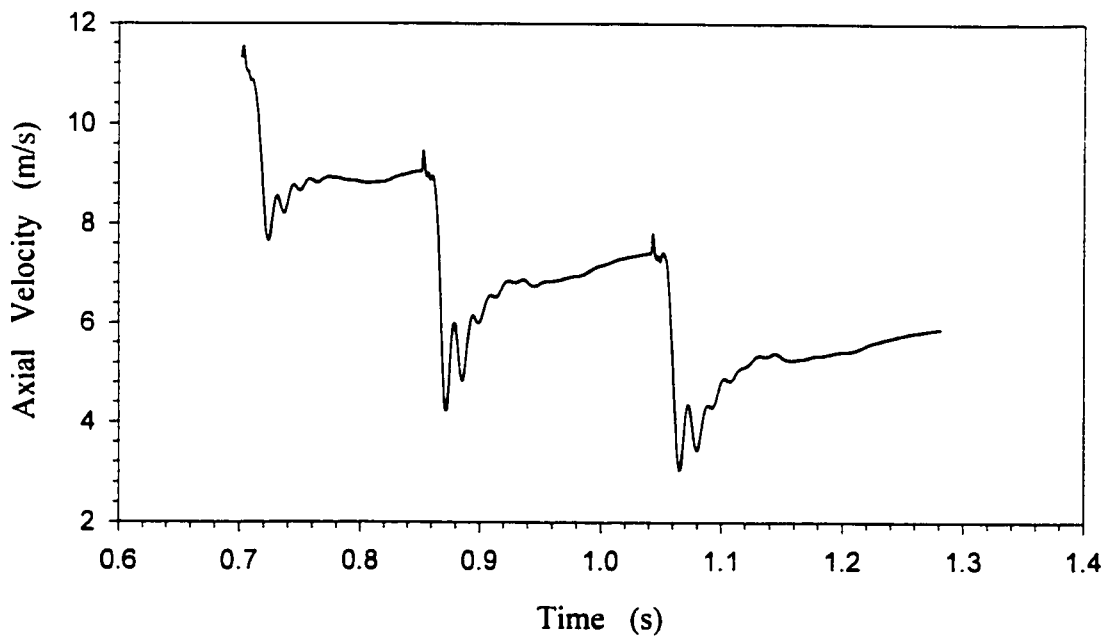in cyclone barrel at z = 0.5 m and r = 0 mm

Figure 5.10: Oscillation damping predicted by numerical simulation
in cyclone cone at z = 0.3 m and r = 5 mm

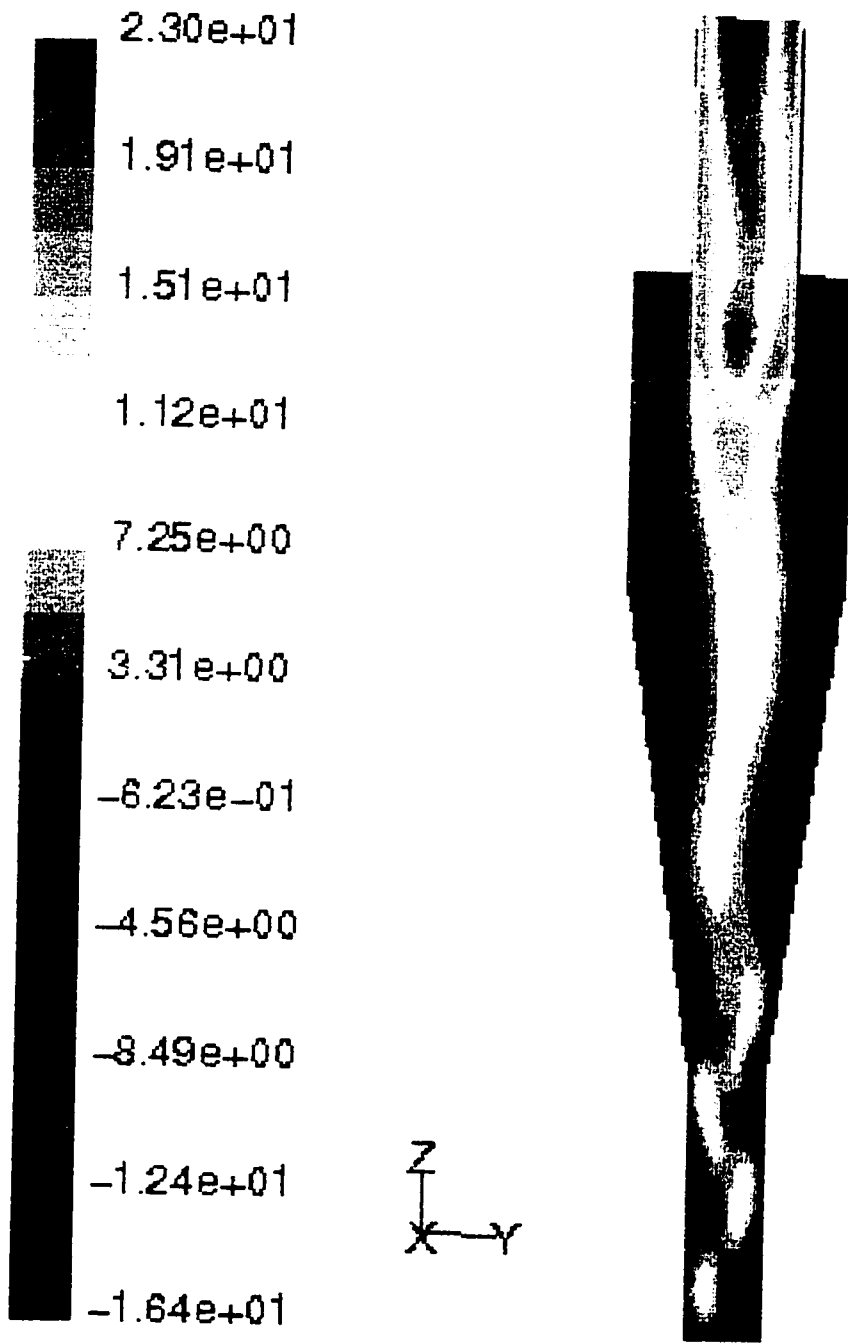|	
2.30e+01	
1.91e+01	
1.51e+01	
1.12e+01	
7.25e+00	
3.31e+00	
-6.23e-01	
-4.56e+00	
-8.49e+00	
-1.24e+01	
-1.64e+01	

Figure 5.11: Axial velocity contour on the xz plane.
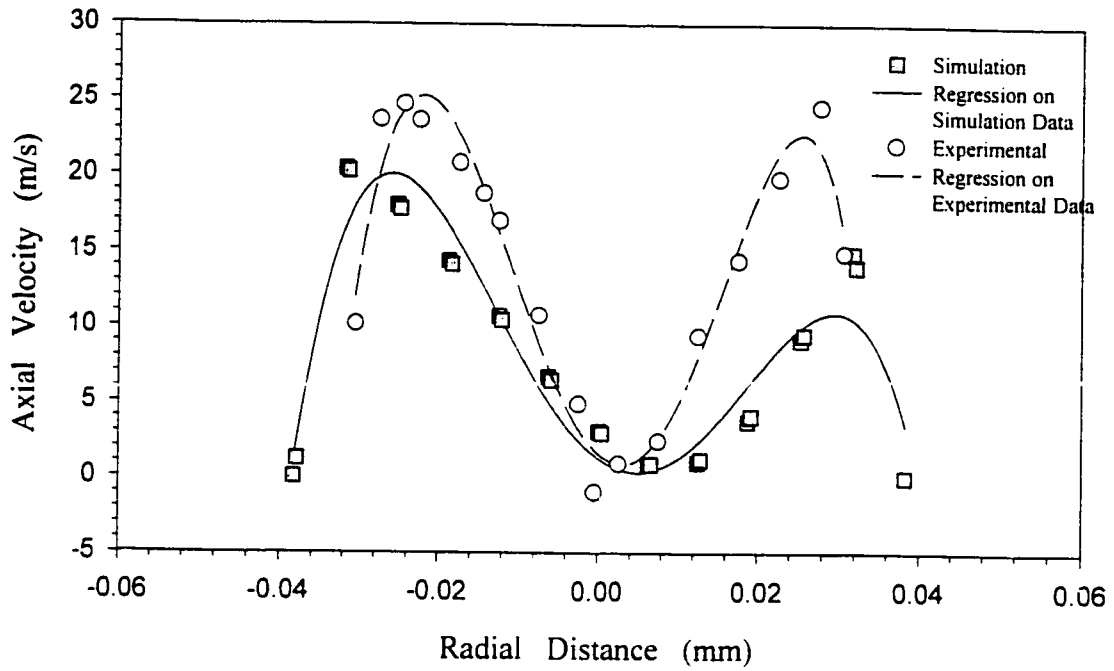
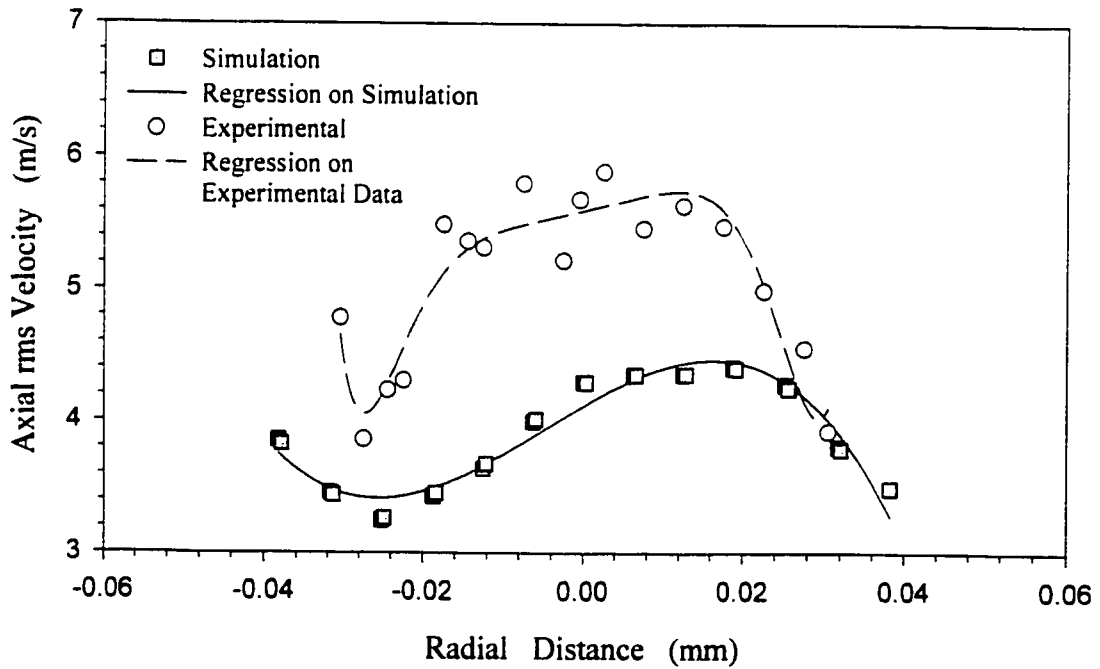Figure 5.12: Axial velocity profile 90 mm from the top of cyclone outlet tube (with $D_{outlet}/D_{barrel} = 0.50$)

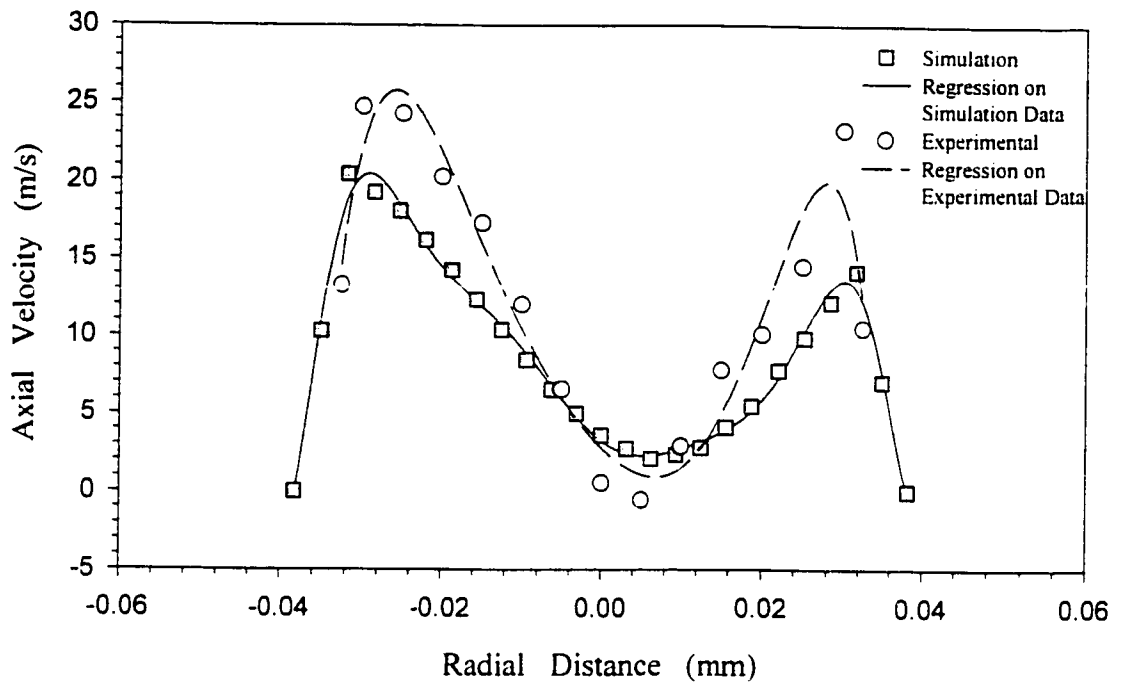Figure 5.13: Axial rms velocity profile 90 mm from the top of cyclone outlet tube (with $D_{outlet}/D_{barrel} = 0.50$)

Figure 5.14: Axial velocity profile in the gas outlet tube 135 mm from the top of the cyclone outlet tube (with $D_{outlet}/D_{barrel} = 0.50$)
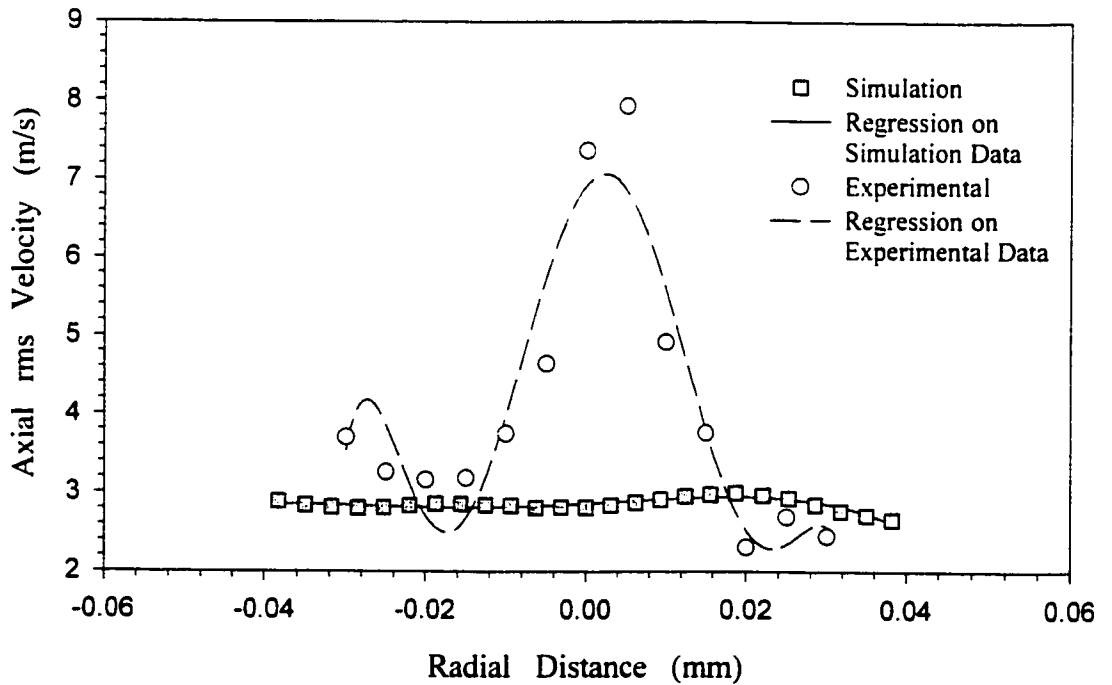

Figure 5.15: Axial rms velocity in the gas outlet tube 135 mm from the top of cyclone outlet tube (with $D_{outlet}/D_{barrel} = 0.50$)
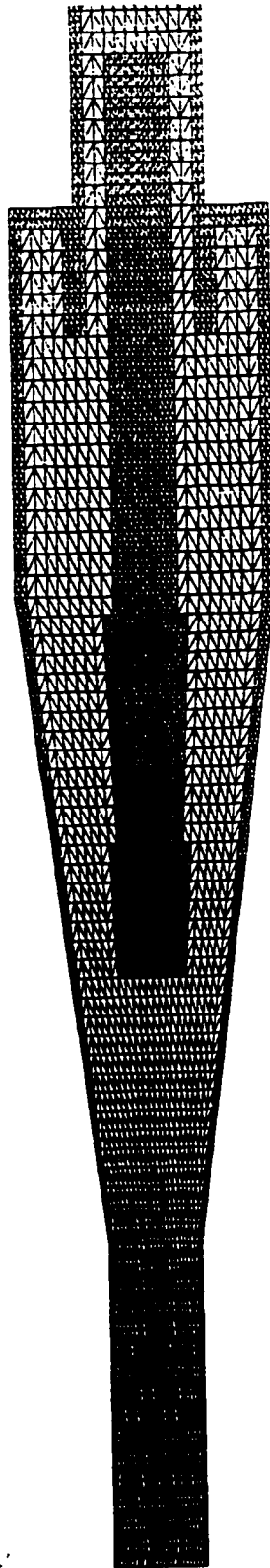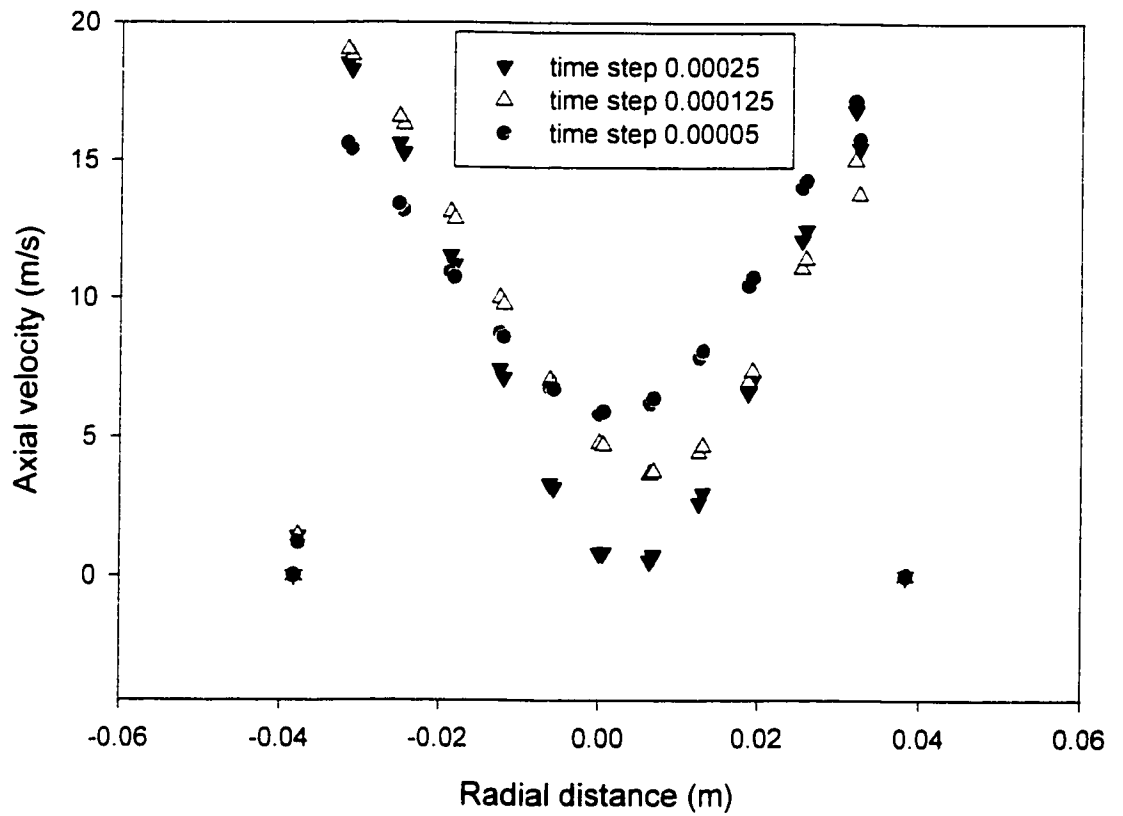
Figure. 5.16: Refined grid with unstructured mesh

Figure 5.17: Time step sensitivity of axial velocity
test at z=0.7m (in the gas outlet tube)

Reference

Brodkey, R. 1995, *Turbulence in Mixing Operations.* Academic Press, New York

Butts, R., 1996, *Single phase CFD simulation of a cyclone separator.* Internal report, Department of Chemical & Materials Engineering, University of Alberta

Edwards, R. & A. Dybbs, 1984, Refrective index matching for velocity measurements in complex geometries, TSI Quaterly **10** 3.

Freitas, C. 1995, *Perspective: Selected benchmarks from commercial CFD code,* ASME J. Fluid Eng., **117**, 208.

Launder, B. & Spalding, D. 1974, *The numerical computation of turbulent flows.* Comput. Methods Appl. Mech., **3**, 269.

McLaughlim, D. & W. Tiederman 1973, *Biasing correction for individual realizationof laser anemometry measurement in turbulent flows.* Physics of Fluids, **16**, 208

Patankar, S. & Spalding, D. 1980, *A calculation procedure for heat, mass and momentum transfer in three-dimensional parabolic flows,* Int. J. Heat and Mass. Transfer, **15**, 1787.

Ranada, V. & Joshi, J. 1989, *Flow generated by a pitched blade turbine-II: Mathematical model and comparison with experimental data,* Chem. Eng. Comm., **81**, 225.

Rodi, W. 1980, *Turbulence model and their application in hydraulics.* A state of the art review, International Association for Hydraulic Research, Delft, The Netherlands.

Tropea, C., M. Streglmeier, and W. Dursthoff 1989, *The application of LDA to the measurement of wave induced velocity fields.* in IAHR workshop on instrumentation for hydraulics laboratories, CCIW, 16 August, Burlington, Canada

Chapter 6: Conclusions

A scaled down Stairmand cyclone was built in the lab to investigate the back flow and the oscillation in the gas outlet tube, especially when changing gas outlet diameter and inlet velocity. Large amplitude, highly periodic, non-axisymmetric fluctuations were observed at the top of the gas outlet tube. Energy spectra constructed from instantaneous velocity components in these regions display strong peaks, establishing the organized and periodic nature of the flow. We may summarize our findings as follows:

- The oscillations and the back flow decay progressively down the gas outlet tube. At the top, periodic motions contribute significantly to the velocity fluctuations, while down the gas outlet tube, they are almost negligible.

- The frequency of the oscillations scaled with the inlet superficial velocity for all the three gas outlet tube diameter tested. Increase the gas outlet tube diameter will decrease the frequency, and vice versa.

- The non-dimensional frequency, i.e. the Strouhal number, was found to be a function of both the swirl number and Reynolds number. The constant ratio of Strouhal number to the swirl number at a given Reynolds number provides useful information to scale up geometry.

- Applying Navier-Stokes equation explained that the strong swirling motion is the cause of reverse flow and with a small diameter gas outlet tube can attenuate the distance back flow in the gas outlet tube.

- The numerical CFD simulation using FLUENT can predict flow pattern qualitatively correct and effective in capturing the essential features of the swirling flow based on our available experimental data. The frequency detected in simulation is about half of the experiments.

- The experiments do not allow conclusions to be drawn concerning the mechanism of the oscillation. We are unable to determine if the non-axisymmetric geometry is related to the oscillations and back flow.

133